Final Report:
Laser Assisted UAV

L.H.A. Goossens, R.G. van Holstein, F.T.H. Liu,
S. Matema, T. Negem, P.T. Peeters,
J.P. Reitsma, B.J.M.M. Slinger, S. Üzümcü

Tutor Dr. R.M. Groves
Coaches ir. M.F.M. Hoogreef
H. Udluft M.Sc.

January 28, 2013

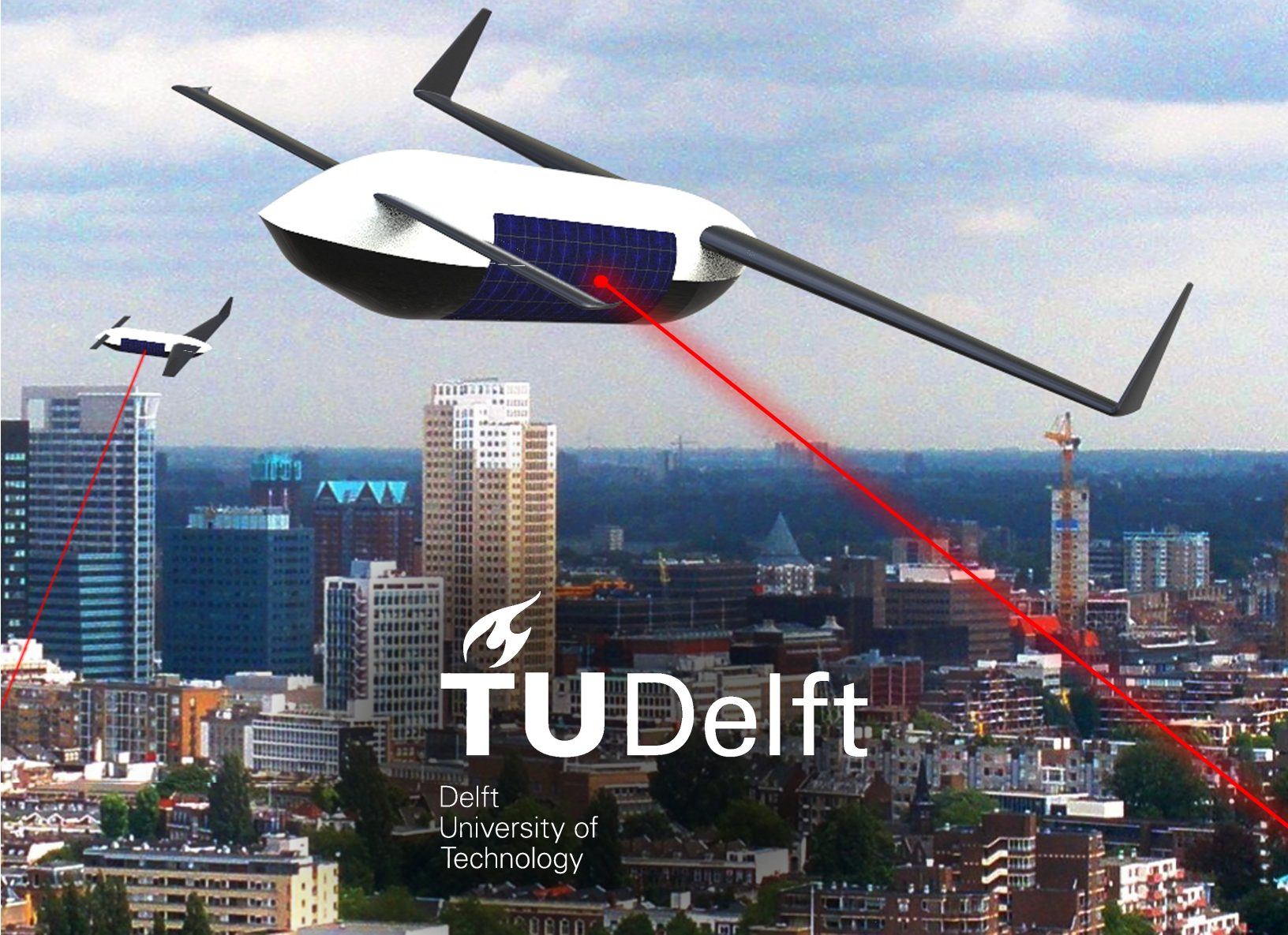

TU Delft
Delft
University of
Technology

Final Report

Group 2 - Laser Assisted UAV

L.H.A. Goossens	4047230
R.G. van Holstein	4012801
F.T.H. Liu	4015711
S. Matema	4048687
T. Negem	1551760
P.T. Peeters	4007956
J.P. Reitsma	4029496
B.J.M.M. Slinger	1507788
S. Üzümcü	4052315

Tutor	Dr. R.M. Groves
Coaches	ir. M.F.M. Hoogreef
	H. Udluft M.Sc.

January 28, 2013
Version 1.0

Update Records

Version	Date	Sections affected	Description of change
0.1 (Draft)	21-01-2013	all	New document
0.2	21-01-2012	1.3	content added
		2	spelling and grammar errors corrected
		5.2	units and equations fixed
		5.2	spelling and grammar errors corrected
0.3	22-01-2012	5.3	units fixed
		5.2	figure reference fixed
		5.3	fixed cross references
		6.2	section 'Interaction among Subsystems' added
		5	introduction added
		5.4	references and units fixed
		10	units fixed
		3	spelling and grammar corrected
		4	spelling and grammar corrected
		9	chapter 'Further Design Steps'
0.4	23-01-2012	-	list of symbols updated
		-	summary updated, spelling and grammar corrected
		2.2	requirements better defined, payload requirement added
		2.3	system overview more elaborated
		3	implemented changes with feedback from Roger
		4.6	implemented changes with feedback from Roger
		5.1	spelling and grammar corrected, references fixed
		5.3	implemented changes with feedback from Roger
		5.4	implemented changes with feedback from Roger
		5.5	spelling and grammar corrected

Version	Date	Sections affected	Description of change
0.5	25-01-2012	all	page margin reduced
		-	list of abbreviations put in alphabetical order
		Summary	rewritten
		3.1	subsection Verification and Validation added
		4	section 'Verification and Validation' added
		4	all sections about structures: feedback implemented
		4.6	feedback implemented to 'Electrical System'
		5.3.2 - 5.3.4	feedback implemented
		5.4.2	table 5.11 adapted
		10	rewritten
1.0 (Final)	28-01-2012	-	bibliography fixed
		-	fixed missing cross references
		Summary	rewritten
		all	feedback implemented
		4	introduction rewritten
		4.1.1 - 4.1.2	rewritten
		4.1.3 - 4.1.4	feedback implemented
		4.1.6	feedback implemented
		4.2.1	feedback implemented
		4.3.1	rewritten
		4.3.2	new section
		4.3.3	new section
		4.3.4	feedback implemented
		4.3.5	feedback implemented
		4.4	feedback implemented
		4.5	new section
		6.3	new section
		10	rewritten

PREFACE

This report concerns the detailed design of the laser assisted UAV, developed during the AE3200 Design Synthesis Exercise, BSc Aerospace Engineering at Delft University of Technology. The chapters of this report outline the operations, in-depth methods and results of the laser powered UAV design. The entire project team would like to express their profound gratitude to the tutor Dr. R.M. Groves and the coaches ir. M.F.M. Hoogreef and H. Udluft M.Sc. for their positive criticism, priceless information, support and guidance during the design process. We would also like to thank ir. H.C.M. Veerman for providing us with valuable information and an extensive UAV database. Finally, we also feel thankful for the help of S. Hulsman B.Sc. in selecting the propeller and electric motor combination.

Contents

List of Tables

List of Figures

List of Symbols

A	Area	m^2
AR	Aspect ratio	[-]
AR_{eff}	Effective aspect ratio	[-]
C_d	Aerofoil drag coefficient	[-]
C_{d_0}	Aerofoil zero lift drag coefficient	[-]
C_D	Drag coefficient	[-]
C_{D_0}	Zero lift drag coefficient	[-]
C_{h_α}	Hinge moment derivative w.r.t. angle of attack	rad^{-1}
C_{h_δ}	Hinge moment derivative w.r.t. deflection	rad^{-1}
C_l	Aerofoil lift coefficient	[-]
$C_{l_{des}}$	Aerofoil design lift coefficient	[-]
$C_{l_{max}}$	Aerofoil maximum lift coefficient	[-]
C_L	Wing lift coefficient	[-]
$C_{L_{des}}$	Wing design lift coefficient	[-]
$C_{L_{max}}$	Wing maximum lift coefficient	[-]
C_{L_α}	Wing lift gradient	rad^{-1}
C_{m_0}	Zero lift moment coefficient	[-]
CR	Cantilever ratio	[-]
G	Climb gradient	[-]
H	Hinge moment	Nm
I	Current	A
I_{xx}	Second moment of area about the x axis	m^4
I_{yy}	Second moment of area about the y axis	m^4
I_{xy}	Product moment of area	m^4
$I_{detector}$	Radiance incident on sensor	$W \cdot m^{-2}$
I_{bird}	Radiance incident emitted by bird	$W \cdot m^{-2}$
L	Length	m
L/D	Aircraft aerodynamic efficiency	[-]
M	Mach number	[-]
M_x	Moment about the x axis	Nm
M_y	Moment about the y axis	Nm
MPE	Maximum permissible exposure	$W \cdot m^{-2}$
$NETD$	Noise equivalent minimum temperature difference	mK
P	Power	W
P_{cruise}	Cruise power	W
P_{max}	Maximum power required	W
P_{loss}	Power loss	W
P_{loss}/P_0	Factor of atmospheric losses at clear conditions	[-]
P_{grid}	Power required from the grid	W
$P_{out,max}$	Maximum output power	W
$P_{max,ground}$	Maximum reflected laser power	$W \cdot m^{-2}$

$\dot{Q}_{conv}$	Heat transfer by convection	W
$\dot{Q}_{rad}$	Heat transfer by radiation	W
$\dot{Q}_{tot}$	Total heat transfer	W
R	Reflectivity for unpolarised light	[-]
R_{copper}	Resistance of copper	Ω·m
Re	Reynolds number	[-]
S	Wing reference area	m^2
S_c	Canard reference area	m^2
S_c/S	Canard area ratio	[-]
S_v	Vertical stabiliser reference area	m^2
S_x	Shear force in x direction	N
S_y	Shear force in y direction	N
T	Thrust	N
$\mathcal{T}$	Torque	Nm
T_{bird}	Temperature of a bird	K
T_s	PV cell panel temperature	K
T_f	Outside temperature	K
V	Velocity	$m{\cdot}s^{-1}$
V_a	Design manoeuvring speed	$m{\cdot}s^{-1}$
V_c	Cruise speed	$m{\cdot}s^{-1}$
V_d	Dive speed	$m{\cdot}s^{-1}$
V_s	Stall speed	$m{\cdot}s^{-1}$
$\bar{V}_v$	Vertical tail volume coefficient	[-]
V_y	Climb speed	$m{\cdot}s^{-1}$
$\breve{V}$	Visibility trough the air	km
W	Aircraft weight	N
a	Acceleration	$m{\cdot}s^{-2}$
b	Span	m
$\bar{c}$	Mean aerodynamic chord length	m
c_r	Root chord length	m
c_t	Tip chord length	m
c_p	Specific heat	$J{\cdot}kg^{-1}{\cdot}K^{-1}$
e	Oswald efficiency factor	[-]
e_{beam}	Vertical beam error	m
g	Standard gravity	$m{\cdot}s^{-2}$

h	Cruise altitude	m
l_c	Horizontal tail length	m
l_f	Fuselage length	m
l_v	Vertical tail length	m
m	Mass	kg
n	Load factor	[-]
n_1	Refraction index of air	[-]
n_2	Refraction index of glass	[-]
q	Size distribution of the scattering particles	[-]
q_b	Shear flow in the skin, open section	$\mathrm{N{\cdot}m^{-1}}$
q_s	Shear flow in the skin, closed section	$\mathrm{N{\cdot}m^{-1}}$
$q_{s,0}$	Resulting shear flow when closing section	$\mathrm{N{\cdot}m^{-1}}$
q_T	Shear flow due to torque	$\mathrm{N{\cdot}m^{-1}}$
r	Distance	m
r_f	Fuselage radius	m
r_{climb}	Horizontal distance covered at maximum climb gradient	m
r_{UAV}	Distance between laser base station and UAV	km
t	Thickness	m
$(t/c)_{max}$	Maximum thickness ratio	[-]
t_r	Maximum root chord thickness	m
α	Angle of attack	$^\circ$
α_L	Horizontal laser angle	$^\circ$
β_L	Vertical laser angle	$^\circ$
δ	Control surface deflection angle	$^\circ$
θ	Flight path angle	$^\circ$
θ_t	Angle of refraction	$^\circ$
θ_i	Angle of incidence	$^\circ$
θ_t	Angle of refraction	$^\circ$
Λ_{LE}	Sweep angle w.r.t. leading edge	$^\circ$
λ	Wavelength	m
μ	Bank angle	$^\circ$
μ_{air}	Dynamic viscosity of air	$\mathrm{kg{\cdot}m^{-1}{\cdot}s^{-1}}$
ρ	Density	$\mathrm{kg{\cdot}m^{-3}}$
σ	Attenuation value	$\mathrm{km^{-1}}$
σ_z	Normal stress due to bending	Pa
τ	Transmittance	[-]
ϕ	Azimuth angle	$^\circ$
ϕ_c	Cable angle	$^\circ$

List of Abbreviations

BER	Bit Error Rate
BMS	Battery Management System
BW	Bandwidth
DC	Direct Current
DOD	Depth of Discharge
EIRP	Effective Isotropic Radiated Power
EOL	End of Life
FSK	Frequency Shift Keying
FSLP	Free Space Loss
FPS	Frames per Second
GaAs	Gallium Arsenide
GPS	Global Positioning System
MMW	Millimetre Wave
MPE	Maximum Permissible Exposure
MPPT	Maximum Point Power Tracking
NACA	National Advisory Committee for Aeronautics
NASA	National Aeronautics and Space Administration
NETD	Noise Equivalent Temperature Difference
NF	Noise Figure
PI	Proportional-integral
PID	Proportional-integral-derivative
PMD	Power Management and Distribution
PNAS	Proceedings of the National Academy of Sciences
PP	Polypropylene
PPU	Power Processing Unit
PSK	Phase Shifting Key
PV	Photovoltaic
QPSK	Quadrature Phase Shift Keying
RAMS	Reliability, Availability, Maintainability and Safety
RF	Radio Frequency
SNR	Signal to Noise Ratio
UAV	Unmanned Aerial Vehicle
USA	United States of America

SUMMARY

This report presents a new way of powering aircraft by the use of laser power. Nowadays, the endurance of aircraft is heavily limited by fuel capacity. Solar power provides an alternative, but requires a large area of solar cells and cannot fly at night without batteries. To extend the endurance of aircraft, laser power beaming is introduced. With laser power beaming, an aircraft no longer requires fuel and can fly continuously during day and night.

A design is presented in which two laser powered unmanned aerial vehicles (UAVs) observe the motorway network of The Hague. These UAVs are capable of carrying a 10 kg payload while flying at a velocity of 100 km h^{-1}. An area of 10 x 10 km is covered by four laser base stations. From these laser base stations, power is transferred using Gallium Arsenide (GaAs) diode lasers and received by GaAs PV (photovoltaic) cells on the aircraft. The PV cells operate at an efficiency of 56%. The wavelength of the lasers is 830 nm, which is invisible to the human eye. The use of lasers invokes certain safety issues. High power lasers have the ability to blind people and animals. Therefore it is important that the laser beam shall only hit the PV cells. The position of the laser beam on the PV cells is measured and communicated to the laser controller, thereby establishing accurate aiming. Laser power is only transmitted when the laser is detected by the PV cells. Part of the laser beam is reflected by the PV cells. Even the reflected beam has devastating power. By applying curvature to the PV cells, the reflected beam is diffused and the intensity on the ground is reduced to a safe level. Obstacles that might fly through the laser beam are detected by a radar system and thermal cameras. When this occurs, the laser is switched off immediately.

The UAVs have a small Lithium-Ion battery allowing for 30 minutes of flight. They supply power when laser power beaming is not possible, but they have to be replaced every five months. Continuous communication with the aircraft is required, mainly for the laser aiming and flight control. Furthermore data must be transmitted to the customers. This is established with 2 $Mb{\cdot}s^{-1}$ radio communication system.

For the UAVs a canard configuration is chosen, which allows placement of the PV cells between the wing and the canard. This configuration is also beneficial because of the lower induced drag compared to a conventional configuration. The structure is made from composites and bio-composites. These are lightweight and strong enough to handle extreme loads. Mainly because of the bio-composites, the recyclability of the UAV is around 75%. Propulsion is provided by an electric motor with a push-propeller, preventing interference with the cameras in the nose. These cameras are used for obstacle detection and avoidance. Instead of using a landing gear, the aircraft will be caught from the sky with a net and a winch is used to redeploy the UAV. The system with four laser base stations, three UAVs, two landing sites and one ground control station has an initial cost of approximately 3.7 million EUR and a yearly operational cost of 178.000 EUR.

It is recommended to perform experimental tests to prove the safety of the laser. This can be done by measuring the reflected laser light and aiming accuracy. The UAV can be further optimised for weight, structural strength and aerodynamic performance by doing wind tunnel tests and load tests. Lithium-Sulphur batteries are recommended, when the technology is matured, as they have a higher power density.

CHAPTER 1

INTRODUCTION

1.1 Background Information

There are many options for large area observations. Trough observations from the sky, a large area can be covered at once. This is often done by using helicopters, aeroplanes and unmanned aerial vehicles (UAVs). These kind of aerial vehicles also provide great flexibility. They can fly to a certain spot to get a better view of the situation. However, helicopters and aeroplanes have the disadvantage of being big and expensive when in operation. Because they are controlled by pilots and have a limited amount of fuel, they cannot stay up in the air for a very long time, as they have to land to refuel.

In order to stay in the air for days, months, or even years, an external power source will have to be used. It has already been proven by the Helios plane [2] that it is possible to fly using just solar energy. However, the amount of power that can be extracted from solar energy is limited by the area of the solar cells. Another external power source is wireless power. This sounds very futuristic, but the technology of beaming energy using lasers has already been proven by NASA in 2003 [3]. The company LaserMotive [4] has also designed a system which can beam 2000 W of laser energy to a UAV, but this is still in the experimental phase.

The great advantage of laser assisted UAVs is that they can stay in the air for a very long time, because they do not have to refuel. Also the weight is lower, because no fuel is carried on board. This results in a lower power requirement. Since no fuel is burned by the aircraft, it will also fly with zero emissions. This is a big advantage in the current political climate, especially when urban areas are considered.

The technology of laser power beaming is still in an early stage. Lasers are potentially very dangerous to the environment and all living creatures. Even orbiting satellites can be damaged with a laser. For larger aerial vehicles, a lot of laser power would be required, increasing the risk even further. Even the reflections of the laser can be harmful. It is clear that safety forms a big constraint on the design of such a system.

Next to that, it is also very important to keep the laser aimed at the aircraft. With a small target at a large distance, the angular margins are very small. A sophisticated control mechanism is required to aim the laser with enough precision and accuracy. Missing the UAV means that no power is being transferred to the UAV. The laser beam will propagate further and might be harmful to aeroplanes or satellites.

If such a laser assisted UAV would be equipped with a camera or other measurement equipment, it could be used for continuous aerial observations for many sorts of applications. For border patrol, continuously flying UAVs can monitor the area for illegal immigrants. In urban areas, the traffic situation can be monitored or it can help the police while chasing suspects. Forest fires can be detected early on. The military can use it for reconnaissance. These are all possible applications for the laser assisted UAV.

1.2 Goal

This report presents a design for a system of laser assisted UAVs. The required design steps required for the system to be operational are presented. This report focuses on the use of laser assisted UAVs to monitor traffic in the motorway network of The Hague. In order to support monitoring capabilities, a payload of at least 10 kg is required.

For the project, the following mission need statement is defined: "Perform continuous unmanned flight with two aircraft powered by lasers which extract power from the electric grid. The aircraft will have an operational life of five years and fly at least at a distance of 1 km from the laser base stations while monitoring an urban area of 10 x 10 km carrying at least 10 kg payload each."

The conceptual design steps were taken in the early stage of the project [5]. The previously selected technologies are analysed in detail, taking the interaction between the different subsystems into account, which results in an integrated final design.

1.3 Report structure

Chapter 2 will describe the mission objectives, top level requirements and eventually show the system overview. Chapter 3 will explain the power transfer procedure. The tracking and aiming procedure and characteristics of the PV cells will be elaborated. Chapter 4 explains the design procedure of the aircraft and its subsystems, chapter 5 explains how the aircraft is controlled and operated and chapter 6 gives an overview and the interactions between the different subsystems. Chapter 7 gives an overview of the sustainability procedure of the whole system and the sustainability of the different subsystems are analysed. Chapter 8 gives an overview of the costs of the system and chapter 9 describes the steps that needs to be taken till the system becomes operational. Finally chapter 10 gives gives the conclusion of the overall project and recommendations that are obtained during the design steps.

CHAPTER 2

MISSION AND SYSTEM OVERVIEW

This chapter describes the mission of the laser assisted UAV. In order to fulfil its mission objectives, the system must satisfy a set of requirements. Therefore the system must be designed in such a way that the requirements are met. Section 2.1 describes the mission objective of this concept and section 2.2 lists the top level requirements of the concept and shows whether those requirements are met. In case a requirement is not met, an explanation is given and an alternative is presented. Finally section 2.3 explains what systems are required in order to fulfil the mission objectives.

2.1 Objectives

The objective of this project is to design a UAV that can fly continuously while monitoring the motorways in The Hague while being powered by optical power beaming with lasers. The aircraft shall have a cruise velocity of 100 $km \cdot h^{-1}$, cruise at an altitude of 230 m and be able to carry a payload of at least 10 kg. The altitude is determined such that the aircraft flies higher than the tallest building in the Hague while stay below the cruise altitude of other aircraft.

The whole system shall consist of two UAVs in the network flying the same flight path while monitoring the priority areas consisting of the A4, A12, A13 and N44 motorways with an interval of at most 15 minutes. An area of 10 by 10 km shall be monitored.

The aircraft operate in a scanning mode and an emergency mode. In case of an emergency one of the aircraft shall leave its flightpath and loiter above the emergency area.

2.2 Requirements

In the early stage of the project a list of requirements was set up [5]. In this section the top level requirements are shown. The top level requirements are summarised in table 2.1 while a full list of the requirements are shown in a compliance matrix, which can be found in appendix A. The requirement code AG, AC, LG, LA OG and OM are the general aircraft requirements, aircraft control requirements, general laser requirements, laser aiming requirements, OG general operational requirements and maintenance requirements respectively. During the design process it will become clear whether the requirements are fulfilled and in case if a requirement is not fulfilled, a solution shall be implemented to ensure that the design can perform its mission.

2.3 System Overview

From the mission overview and the top level requirements it can be concluded that the concept needs a laser base station to provide power to the aircraft, two aircraft for monitoring purpose and a control system to control the aircraft. The laser base station must be able to track the aircraft accurately enough to aim its laser on the PV cells and the laser beam must be powerful enough to provide the required power to the aircraft and its subsystems in order to fulfil its mission. However, it is also important that the laser beam shall not be a threat to the environment.

The aircraft shall be able to monitor the priority area at the required cruise velocity. The aircraft shall also have enough space to store its subsystems which are required to perform its mission.

Finally a crew is needed to operate and maintain the aircraft. The aircraft needs to be launched during its first use and recovered once in four weeks for maintenance purpose. In normal operational use the aircraft needs to receive its preprogrammed flight path which is send by the operator to the UAV and the UAV shall follow its waypoints during the mission. When an emergency occurs, one of the aircraft shall receive a new command so that it leaves its flightpath and loiters above the emergency area. The aircraft thus needs to communicate with the ground station in order to receive its commands. The aircraft shall follow its flightpath and autonomously and in order to make this possible, an autopilot system is required to process the data of the flightpath and the commands sent by the operators.

Table 2.1: The top level requirements of the laser assisted UAV concept.

Code	Requirement	Determined by?
AG. 2	The aerial vehicle shall be unmanned.	The project guide.
AG. 4	The aircraft shall be able to carry a payload of at least 10 kg.	The project guide.
AG. 5	The aircraft shall be able to monitor continuously.	The project guide.
AG. 6	The aircraft shall be powered by optical power beaming with lasers.	The project guide.
AG. 7	The aircraft shall have an operational life of 5 years.	The project guide
AG. 8	The aircraft shall have cruise velocity of 100 km h^{-1}.	The project guide.
AC. 1	The control system shall use flight path commands to control the aircraft.	The project group.
AC. 2	The control shall autonomously evade obstacles detected by the obstacle detection system.	The project group.
LG. 2	The laser base stations shall cover an area of 10 by 10 km.	The project guide.
LG. 3	The laser base station shall continuously provide power to the aircraft.	The project group.
LG. 5	The laser range from the laser base stations to the aircraft shall be at most 4 km.	The project group.
LA. 5	The laser shall at all time be aimed at the photovoltaic cell area on the aircraft when it is active.	The project group.
OG. 1	Two aircraft shall operate simultaneously in the same network.	The project guide.
OM. 1	The aircraft in the network shall monitor an area of 10 by 10 km around the motorway network of the Hague.	The project guide.
OM. 2	The aircraft in the network shall operate in scanning mode and emergency mode.	The project group.
OM. 3	In scanning mode, the aircraft in the network shall fly the same flight path, while monitoring the priority area consisting of the A4, A12, A13 and N44 motorways with an interval of at most 15 minutes.	The project group.
OM. 4	In emergency mode, one of the aircraft in the network shall leave its flight path and fly to and loiter above the emergency target area.	The project group.

2.3.1 Summary of the Systems

From the mission overview it can be concluded that in order to have this concept operational, there must be several laser base stations, two UAVs, a launch and recovery system for the UAV and a control and operation station. In the early stage of the design phase, different technologies were analysed and decisions were made what technologies will be used to perform certain tasks. Eventually a concept of the aircraft and network are chosen. The decisions made for the systems are explained below.

Laser base station

The laser base station shall house the laser used to transfer power to the UAV. To ensure that the laser beam always hits the PV cells, the tracking and aiming system shall require pinpoint accuracy. Furthermore the laser base station must have the right communication systems to communicate with the aircraft and the ground station. Four base stations and six lasers shall be available in the network and laser tracking shall be used to determine the position of the PV cells

Aircraft

The aircraft shall have a canard configuration. The fuselage of the aircraft shall provide storage for the subsystems and payload and the PV cells shall be located on the fuselage itself. A push propeller will be used to provide thrust driven by an electric motor and finally batteries shall be used to provide power to the subsystems when power beaming is not available.

Control and Operation

The aircraft is controlled by deflecting its control surfaces which are driven by servo actuators. As for flight control, it was decided that the aircraft shall follow a preprogrammed flightpath and thus an autopilot shall be installed. For obstacle detection the aircraft shall have a conventional and an infrared camera and communication is established using radio frequencies. Finally it was decided that the aircraft shall be launched using a winch and recovered using a net.

2.3.2 Network Simulation

In order to visualise the operations of the two aircraft in the network of laser base stations (LBS), a simulation is performed. From this simulation, the time without laser power, various angles and the distance between the UAVs and laser base stations are calculated. The results are used for the design and sizing of the laser aiming system, energy collection system and electric system. A snapshot of this network simulation is shown in figure 2.1.

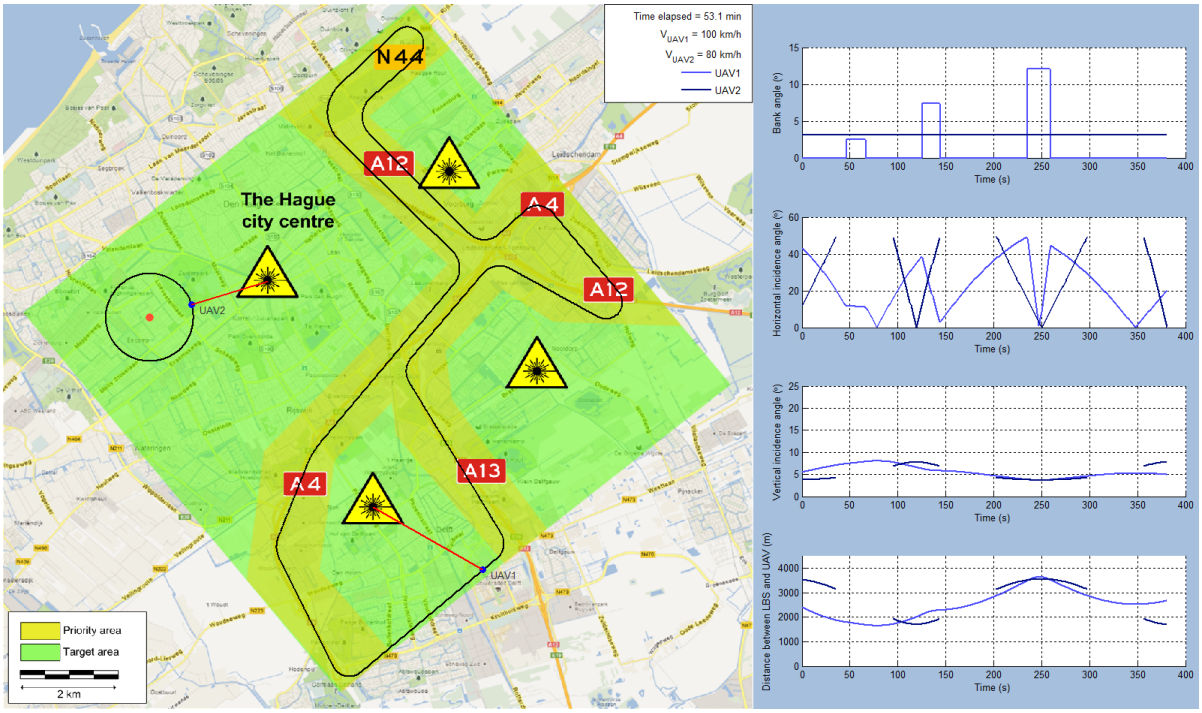

Figure 2.1: Snapshot of the network simulation showing UAV1 flying in scanning mode and UAV2 loitering in emergency mode.

Description of the simulation

The simulation starts with the two UAVs flying a preprogrammed flight path over the motorway network of the Hague during scanning mode. With a cruise speed of 100 km/h and a round time of approximately 25 minutes, they monitor this priority area (indicated yellow in figure 2.1) with an interval of 12.5 minutes. The aircraft are almost continuously powered by the laser base stations. As the UAVs come close to another laser base station, that base station takes over the power transfer. This allocation of the laser base stations to power the aircraft is preprogrammed.

At some point in the simulation, an emergency situation arises. The flight path of one of the aircraft is reprogrammed by the ground crew, after which the aircraft cruises to the emergency area. During this emergency mode, the aircraft slows down and loiters above the area. A nearby laser base station provides power to the aircraft. After a while, the emergency situation is resolved and the UAV is ordered

back into scanning mode. The aircraft accelerates to cruise speed and enters the priority area such that the monitoring interval of the two UAVs is 12.5 minutes again.

During the simulation, the bank angle of the aircraft, the incidence angle of the laser beam in the horizontal plane θ, the incidence angle of the laser beam in the vertical direction φ and the distance between the UAV and laser base station d are displayed in real time. The definition of the last three variables is shown in figure 2.2. The horizontal and vertical incidence angles are defined to be zero when the laser light strikes the photovoltaic cells (which are positioned at the sides of the fuselage) perpendicularly.

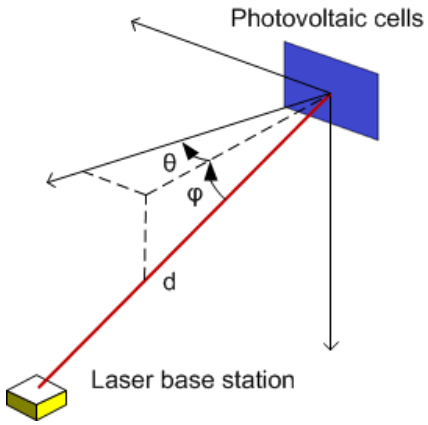

Figure 2.2: Definition of the incidence angle of the laser beam in the horizontal plane θ, the incidence angle of the laser beam in the vertical direction φ and the distance between the UAV and laser base station d.

Analysis of the simulation

The four aforementioned variables are plotted in figure 2.2 for one complete circuit of one UAV in scanning mode. The bank angle shown in figure 2.2(a) is calculated based on the velocity of the aircraft and the turn radius. In reality the aircraft does not abruptly go from straight flight into banked flight. However, a very accurate representation of the behaviour of the aircraft in banked flight is not available yet nor required for this conceptual analysis. The flight path is constructed such that this bank angle is limited to less than 15 °. This way the photovoltaic cells do not need to cover the complete circumference of the fuselage. Hence, by limiting the bank angle, the mass and cost of the photovoltaic cells are limited as well.

As can be seen in figure 2.2(b), the horizontal incidence angle changes rapidly over time. This angle decreases when the UAV approaches the point in its flightpath were it flies in a direction perpendicular to the laser beam, where the horizontal incidence angle reaches the minimum of 0 °. As the aircraft flies away from this point, the horizontal incidence angle increases again.

When the aircraft performs a turn towards the laser base station, the horizontal incidence angle drops rapidly. This behaviour can be observed for the first two turns in the graphs of figure 2.2. On the other hand, the third turn is away from the laser base station, so that the horizontal incidence angle increases rapidly. The fourth turn shows that at times the incidence angle of the laser beam on the photovoltaic cells becomes too large. The laser is shut down at these angles, because most of the laser light is reflected. Not only does the power output drop drastically in this situation, the reflected light can also be harmful to inhabitants of the area. For more information about reflection of laser light on the photovoltaic cells, see section 3.3.

The interruption of power transfer is visible on figures 2.2(b), 2.2(c) and 2.2(d) by the discontinuity of the graphs. By summing up the time the power transfer is interrupted, the time without laser power for one complete circuit in scanning mode is determined to be 2 minutes and 43 seconds or approximately

10 % of the time. In emergency mode, the interruptions of power transfer are more severe. When the aircraft loiters above the emergency area it is flying in circles. It receives laser power for approximately 60 % of the time only, because the horizontal incidence angle of the laser beam often gets too large. This aspect of the emergency mode limits the maximum loiter time. However, the time the aircraft receives laser power in emergency mode can be increased by flying a rectangular or elliptical flight path, so that the horizontal incidence angle is low most of the time. The time without laser power is used for the sizing of the batteries in section 4.7.

Figure 2.2(c) shows that the distance between the laser base stations and the aircraft is most of the time between 1.5 and 4.0 km. The distance is seen to increase or decrease depending on whether the aircraft approaches or flies away from the laser base station. The distance data is also used in the design of the laser aiming system and the energy collection system described in section 3.3.

The vertical incidence angle displayed in figure 2.2(d) shows a more steady behaviour than the horizontal incidence angle. This is because of the generally large distances between the aircraft and the laser base stations and the low altitude of 230 m the aircraft is flying at. Only when the aircraft comes close to the laser base station, the vertical incidence angle increases to a value of 20 °. The data is used to design the laser aiming system in section 3.1.

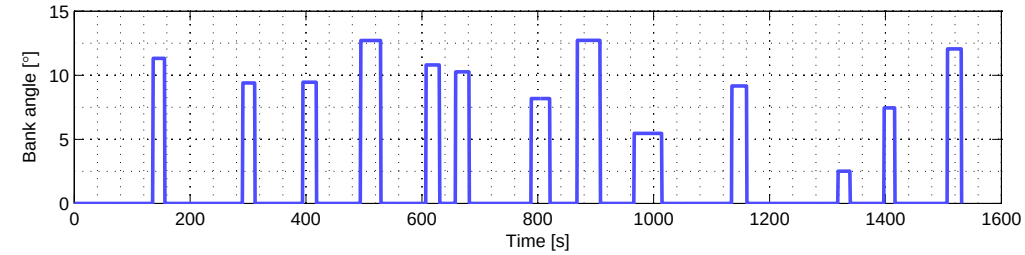

(a)

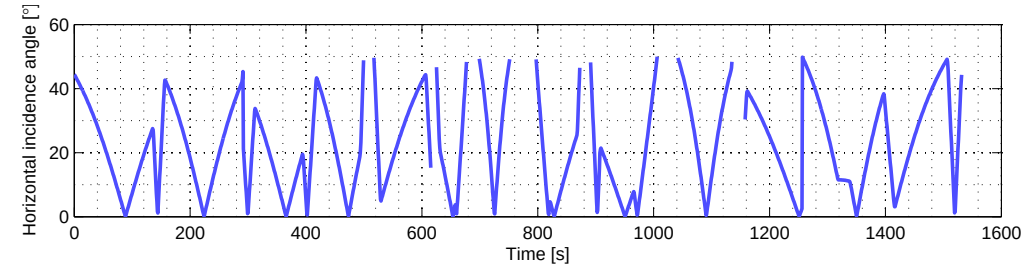

(b)

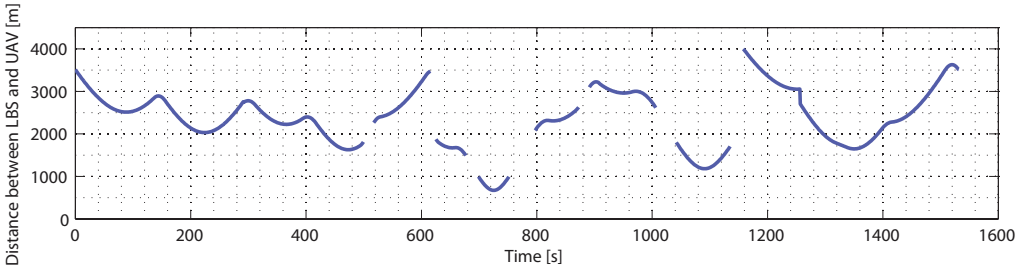

(c)

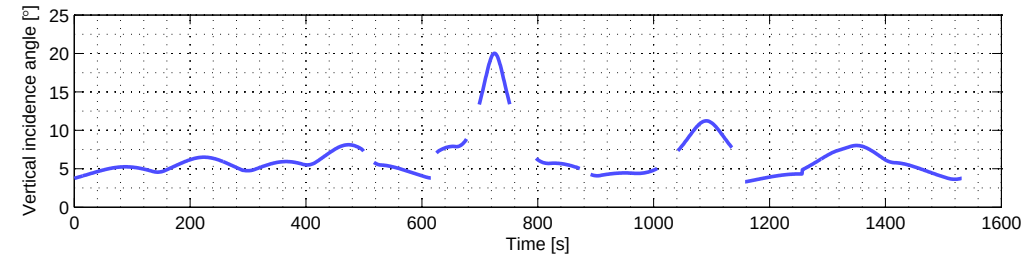

(d)

Figure 2.2: Calculated angles and distances for one UAV flying one complete circuit in scanning mode.

CHAPTER 3

LASER BEAMING

In order to propel or communicate with the UAV, power has to be transfered from the ground to the aeroplane. Before power can actually be transmitted, the exact location and attitude of the UAV has to be known. This is analysed in the first section. Then the power transfer is considered. How the PV cells on the plane receive the laser power and convert a part of it to electric energy concludes this chapter.

3.1 Tracking and Aiming

When the UAV is flying, it has to be tracked by the laser to obtain power. The problems are defined in section 3.1.1. Section 3.1.2 describes the proposed solution to the problem. The idea behind the control system is explained in section 3.1.3. In order to make sure the system works, the components are modelled in section 3.1.4 and 3.1.5. The verification and validation of the results is discussed in section 3.1.6.

3.1.1 Problem Definition

When the UAV is flying, it has to be tracked by the laser to obtain power. This has to be done very accurately. The allowable margin is in the order of a few centimetres in all directions. Every extra centimetre increases the size of the PV cells, which determine the size of the fuselage. This should be kept small to minimise drag. The beam diameter of 20 cm is selected in section 3.3 for safety reasons.

Depending on the position of the UAV, this results in a margin requirement for the angles of the laser. The two extreme cases are studied here. The angles of the laser are shown in figure 3.1(a). The horizontal angle is defined as α_L and β_L is the vertical angle.

At the largest distance from the laser base station (approximately 4 km), the required accuracy is the highest and the required angular velocity is the lowest. 10 cm over a distance of 4 km corresponds to an angular resolution of 25 µrad.

When the UAV passes the laser base station close by (at approximately 200 m ground distance), the required accuracy is the lowest, but the required angular velocity is the highest. At an altitude of 230 m and with a velocity of 100 km/h, the required horizontal angular velocity of α_L is 0.14 rad·s^{-1} or 8°·s^{-1} and the maximum vertical angular velocity of β_L is 0.035 rad·s^{-1}. Figure 3.1(b) shows the required angles of the laser to track the UAV in this situation.

If the system is able to stay within the margins for these two situations, it will also be within the margins for all the other situations.

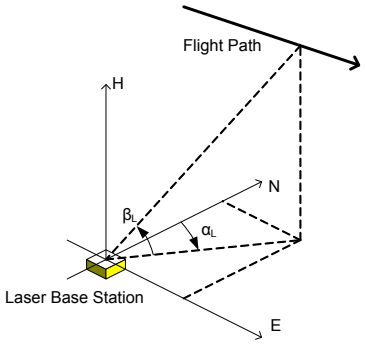

(a) Laser Base Station angle definitions.

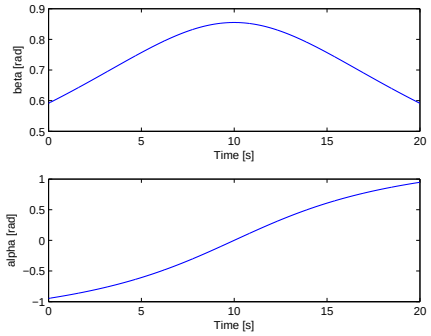

(b) Flight Path angles.

Figure 3.1: Angles from Laser Base Station to the UAV.

3.1.2 System Configuration

The laser aiming system consists of a rotary stage (figure 3.2(a)) for the horizontal angle and a galvanometer (figure 3.2(b)) for the vertical angle. The galvanometer is mounted on top of the rotary stage, such that the mirror is positioned above the hole in the centre. The rotary stage can rotate 360°. The galvanometer provides a range of 40°. The beam diameter and divergence is controlled by two lenses at variable distance.

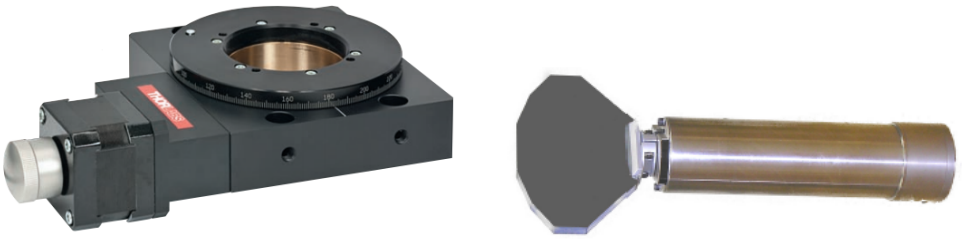

(a) Rotary Stage by Thorlabs.com (b) Galvanometer by Cambridge Technology

Figure 3.2: Optical systems to control the laser beam.

Galvanometer

Galvanometers are very fast and accurate electro-mechanical devices to control a rotation angle. When a mirror is mounted onto it, the laser beam can be deflected accurately in a given direction. Galvanometers are already being used in many laser applications.

Accuracy of galvanometers is given in terms of short-term repeatability. This is the range of error that occurs when the galvanometers is repetitively commanded to the same position. Closed loop galvanometers use an internal optical position detector to provide this repeatability.

When comparing different galvanometers from different manufacturers, the 8360K Galvanometer [6] by Cambridge Technology provides a low repeatability error of 8 µrad and can be used for beam apertures up to 100 mm. Since an error range of 8 µrad can be detected, the position can be controlled with a resolution of 8 µrad. The angular velocity easily satisfies the requirement because the galvanometer can reach any position within a split second. This assumption is validated by the model in section 3.1.4.

Rotary Stage

The rotary stage allows the laser to focus in all possible horizontal angles. There are many manufacturers of such rotary stages. The NR360S [7] from Thorlabs is selected because it is very well documented and it satisfies the requirements. The resolution is less than one arc second or 4.8 µrad and the maximum speed is $20°{\cdot}s^{-1}$. However, the accuracy is only 5 arc minutes or 1.5 µrad, while 25 µrad is required. In order to take maximum advantage of the resolution, an advanced control system is required.

The rotary stage can also be used for the communication system in order to reduce antenna pointing losses. Cameras used for obstacle detection can also be placed on top of it, in order to assure a clear line of sight when firing the laser.

3.1.3 Controller Philosophy

It is of great importance that the target is tracked before the laser power is transferred. This can be done by gathering positioning information from the UAV with just centimetres accuracy. However, this requires an expensive positioning system and the system then has to be calibrated with great precision. Even then, it might be subject to other errors.

A better and more reliable method would be to use the actual laser position as feedback for the controller. By taking measurements on the PV cell, the laser position can be determined. The laser

position is communicated immediately to the laser controller on the ground where it is used as input. This way, a closed loop system is constructed.

The position data does not have to be very accurate to do this. Therefore, simple GPS position measurements can be used.

PV cell measurements

The laser beam intensity can be approximated by a Gaussian distribution [8]. The PV cell exists of small sections of which the dimensions are approximately 5 x 5 cm. For each of these sections, the received power can be measured. The placement of the PV cells is shown in figure 3.3. The received power on the PV cell is plotted in figure 3.4 where a beam diameter of 20 cm is used. From this figure, it is clear that the actual beam position can easily be determined by finding the cell with the maximum power. The accuracy can be improved by using curve fitting techniques, since the beam properties are known. However, this would require more computational power on board, or a higher data rate if the computation is done on the ground.

With a PV cell size of 1 m length, 0.6 m height and sections of 5 x 5 cm each, there are 240 sections. The number of the section that receives most laser power is communicated to the laser base station. This can be described with 8 bits. If the position is communicated 1000 times per second, the required data rate is 8 kbits$\cdot$s^{-1}.

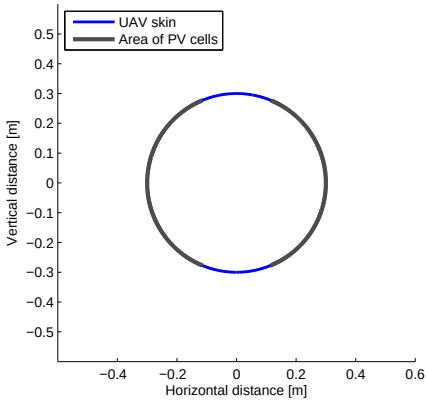

Figure 3.3: Placement of the PV cells.

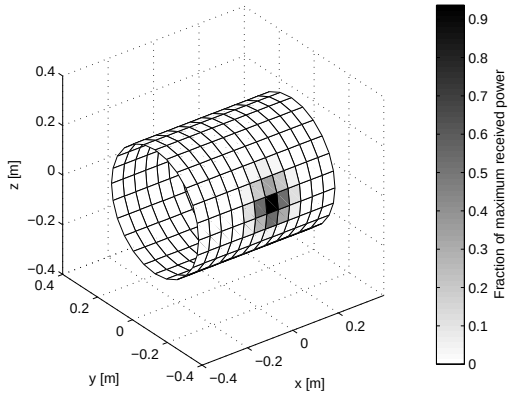

Figure 3.4: Received power by the PV cell.

Initial tracking

The first step of tracking is determining a rough estimate of the position of the aircraft. An on board GPS receiver supplies the position information to the laser base station. This is accurate up to a 5 metres [9]. Then, the laser starts scanning around that position with low power. When the laser beam is detected by the PV cell, this information is sent to the laser base station. Only when the laser beam stays continuously within the margins, the beam intensity is set for power transfer.

3.1.4 Galvanometer

For the vertical angle, the Cambridge Technology 8360K galvanometer [6] is used. The parameters of this model already show sufficient behaviour. In order to assure functioning in the system, the situation is modelled in Simulink.

Model

The parameters of the galvanometer are well documented and can be used for constructing a model. For the galvanometer itself, the model described by Michael Widlok in his PhD Thesis [10] is used. This model is used because it was extensively researched, verified and validated. Table 3.1 shows the values that are used in the model.

Table 3.1: Galvanometer 8360K parameters

Parameter	**Value**	**Unit**
Coil Inductance	0.61	Ω
Coil Resistance	541	mH
Torque constant	86	$\mathrm{mN{\cdot}m{\cdot}rad^{-1}}$
Rotor inertia	4.75	$\mu\mathrm{kg{\cdot}m^2}$
Rotor dynamic friction	4	$\mu\mathrm{N{\cdot}m{\cdot}s{\cdot}rad^{-1}}$
Torsion bar constant	17.9	$\mathrm{N{\cdot}m{\cdot}rad^{-1}}$
Back EMF voltage	85.9	$\mathrm{mV{\cdot}s{\cdot}rad^{-1}}$

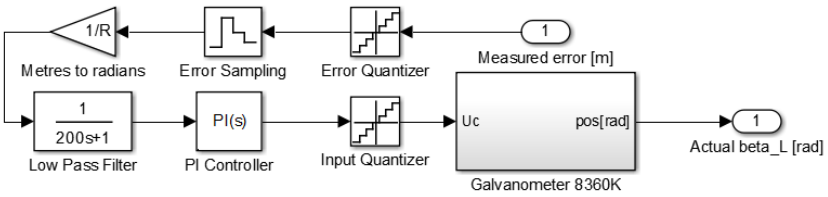

Figure 3.5: Galvanometer control model.

Figure 3.5 shows how the galvanometer is controlled. The measured error on the PV cell forms the input of the system. The sections of PV cell form a resolution of 5 centimetres. This is simulated by quantizing the error to an interval of 5 cm.

Then, the data is sent to the laser base station with radio signals. The communications are described in detail in section 5.3 Therefore the data has to be converted to a digital signal which is simulated with a data sampler block. A sampling time of 1 ms is used in order to provide a fast feedback response. Using a slower sampling time results in lower accuracy.

The distance is measured with the GPS signal. The deviation on the PV cell is then divided by the distance to convert it to an angular deviation. Even if the GPS measurement is off by a five metres, the error on the angular deviation remains small. On the ground, the received error signal is filtered by a low pass filter. This filters the high frequencies caused by quantization and data sampling.

This filtered error is fed into the proportional-integral (PI) controller which generates the input for the galvanometer. In order to simulate a resolution of 8 µrad, this signal is quantized to this interval.

Controller

Proportional-integral-derivative (PID) controllers are the most commonly used feedback controllers and can be tuned for optimal performance. Derivative control is often applied to increase performance in the transient response. This is not required because the galvanometer itself already has an excellent response time. Therefore a PI controller is used here.

Figure 3.6 show the step response of the galvanometer. This response is already very fast, with a reaction time of less than 0.02 s. The overshoot is less than 5%. By tuning the PI controller the result from figure 3.7 is obtained. Figure 3.13 shows the deviation in centimetres. From this figure, it can be concluded that it is possible to aim the laser within a vertical range of twelve centimetres.

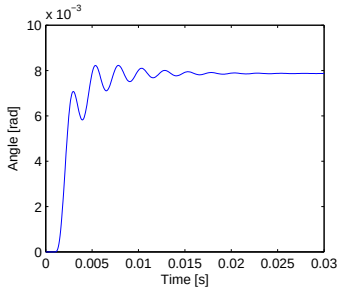

Figure 3.6: Galvanometer small angle step response.

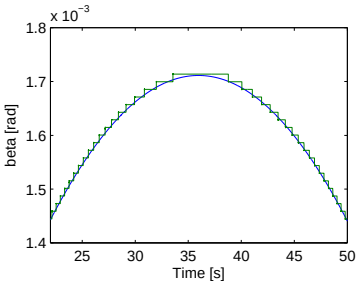

Figure 3.7: Galvanometer path tracking.

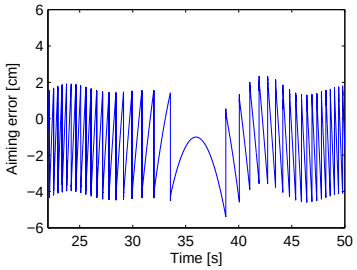

Figure 3.8: Galvanometer aiming error.

3.1.5 Rotary stage

The rotary stage from Thorlabs.com is driven by a stepper motor. A full rotation of the stage requires 66 full rotations from the stepper motor. The hybrid stepper motor used in the stage has 50 individual magnetic teeth, allowing a step size of 1.8°. By applying a current to both phases simultaneously, micro steps can be created [11]. When the BSC101 stepper motor controller is used, the stepper motor provides 25,600 micro steps per revolution. Each micro step then results in a rotation of 0.0141° of the motor and a rotation of $(0.213{\cdot}10^{-3})°$ of the stage.

Model

For the simulation, the stepper motor [12] from the Simulink library was used. Table 3.2 shows the parameters used. The driver used in the example can only perform full steps. In order to simulate the BSC101 stepper motor controller, a new driver (figure 3.9) is created such that it performs 128 micro steps for every full step. This is achieved by using sine and cosine functions for the current, instead of block signals. The new driver also has rotation speed control. This is done by making the micro step rate proportional to the required angular velocity.

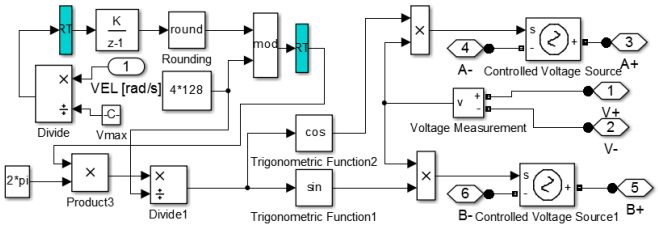

Figure 3.9: Stepper motor driver with micro steps and velocity control.

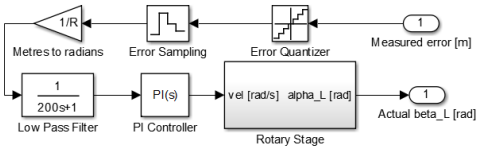

Figure 3.10: Rotary stage control model.

Table 3.2: Stepper motor parameters

Parameter	**Value**	**Unit**
Winding Inductance	6	mH
Winding resistance	4.6	Ω
Step angle	1.8	deg
Maximum Flux Linkage	0.1528	V·s
Maximum Detent Torque	$17{\cdot}10^{-3}$	N·m
Total inertia	$6.8{\cdot}10^{-4}$	$kg{\cdot}m^2$

The control method of the rotary stage (figure 3.10) differs slightly from that of the galvanometer. The rotary stage has a speed control instead of position control. There is no input quantization after the PI controller, because the resolution is already simulated by the micro steps inside the stepper motor driver.

Controller

Figure 3.11 shows the response of the stepper motor with and without micro stepping. Without steps, the response is fast but unsteady. Micro stepping slightly slows the response time but shows better stability.

Just like for the galvanometer, a PI controller is used. After tuning the parameters of the PI controller, the range around the target spot is eight centimetres.

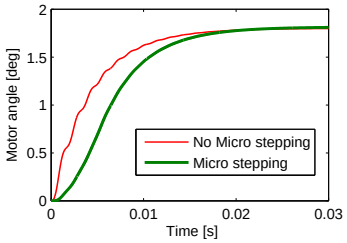

Figure 3.11: Stepper motor single step response.

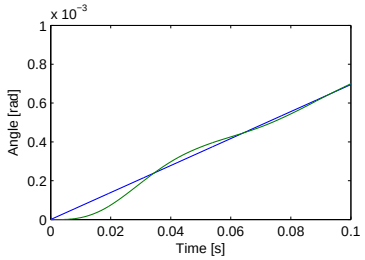

Figure 3.12: Rotary stage path tracking.

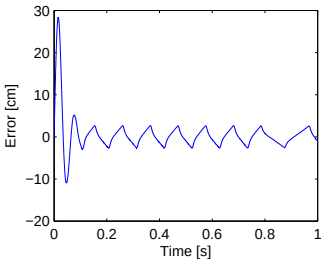

Figure 3.13: Rotary stage aiming error.

3.1.6 Verification and Validation

The models show that it is possible to aim the laser accurately over a distance of 4000 metres. A vertical range of around 6 cm is seen for the galvanometer, which corresponds to 15 µrad. This is slightly higher than the error range of 8 µrad.

The model of the rotary stage also shows an error range of around 6 cm or 15 µrad. This is significantly higher than the size of a micro step which is $(0.213{\cdot}10^{-3})^\circ$ or 4 µrad.

These errors were to be expected because errors are introduced by PV cell measurements and sampling. However, it should be taken into account that in the real world, there will always be disturbances in the system. These disturbances are considered as the known unknowns and can only be obtained by doing measurements. This could be done by measuring angular deviations of the systems with the same level of accuracy while aiming at a fixed spot.

3.1.7 Conclusions and Recommendations

From the model, it is concluded that the vertical and horizontal range both 6 cm. Together with the beam diameter, this sets the requirement for the PV cell area. However, before building the entire system, it is recommended to validate the model with testing.

At this point, the controller gets only feedback on the angles. If it turns out that a higher accuracy is required, this could be gained by implementing a feed from the angular velocity. This is not directly measurable on the PV cells. The required angular velocity can be predicted by position and velocity data from the UAV, by dividing the velocity vector by the distance. An error in the distance therefore has only a small effect on the result. The velocity measurement should be accurate. GPS position data is expected to satisfy these requirements, but this was not proven yet.

3.2 Analysis of Power Transfer

Now that the position of the UAV is known, a power transfer system has to be designed. This system will consists of an array of lasers and PV cells mounted on the fuselage of the UAV. This section covers the power transfer from the electric grid up to the PV cells. From the electric system a power requirement is given of $P_{req} = 2.2 \cdot 10^3$ W. In order to provide this amount of power, a laser is selected and laser efficiency is analysed. To conclude this section atmospheric and cable losses are considered.

3.2.1 Selection of Power Transfer Laser

The selected laser is a diode laser with a wavelength $\lambda = 830$ nm and a maximum output $P_{out,max} = 4500$ W from the company Coherent [13]. Diode lasers can be stacked into arrays boosting their output power and reliability while emitting outside the visible spectrum, thus they do not provide distraction near motorways. The diodes use Gallium Arsenide (GaAs) to provide the required stimulated emission of photons. The advantage of diode lasers is that units can be stacked into arrays, increasing the scalability of the laser. The selected laser uses 45 bars with an output of 100 W each. A disadvantage of using diode lasers is the required active cooling system, increasing the complexity and the energy required. This is the reason that the efficiency of lasers is often described as wall plug efficiency, this efficiency accounts for the laser efficiency including cooling of the array. Other requirements for use of the cooling system are using deionised water, limited conductivity and a neutral pH of the cooling water.

The camera for obstacle detection camera operates between 9.0 μm and 14 μm. Therefore the laser will not interact with infrared cameras and normal, visible-spectrum, cameras. Moreover, the tracking and aiming system will avoid pointing at the cameras at all times and the cameras are placed on the nose of the UAV, as far from the PV cells as possible.

3.2.2 Losses due to Laser Power Beaming

Besides the losses in the laser due to heat production, two other factors contribute to power loss in laser power beaming. First cable losses are analysed. The other loss is the loss of laser power in the atmosphere due to Rayleigh scattering for air, Mie scattering for water vapor and absorption of the medium.

Cable Losses

The connection from the electric grid will be three-phase electric power. The higher voltage of $V = 400$ V decreases the required electric current I and therefore decreases the energy losses given by equation 3.1, in which R is the resistance in Ω·m. For a copper wire of 25 m with conductivity of $R_{copper} = 1.68{\cdot}10^{-8}$ Ω·m [14] the losses will be 0.16%.

$$P_{loss} = I^2 R_{copper} \tag{3.1}$$

Atmospheric Losses due to Laser Power Beaming for Clear Weather Conditions

When light travels through a medium, photons collide with particles of this medium, causing absorption and scattering. Both effects contribute to atmospheric losses, because the emitted light is not able to reach the target. For light transfer through air, Rayleigh scattering applies because the relatively small particles in the air are redirected. The combination of these effects has been investigated by Tomasi and resulted in a coefficient of transmittance $\tau_{\lambda=830nm} = 0.94$ km^{-1} for $\lambda = 830$ nm [15]. The atmospheric loss will be highest when the distance between the laser base station and UAV is maximal. The maximum distance between the UAV and the laser will be $r_{UAV} = 4.0 \cdot 10^3$ m. The maximum atmospheric losses are calculated as 21.9% and can be seen from equation 3.2.

$$\frac{P_{loss}}{P_0} = 1 - \frac{P}{P_0} = 1 - (\tau_{\lambda=830nm})^{4.0} = 1 - 0.94^{4.0} = 0.219 \tag{3.2}$$

Laser Power Beaming Losses in Bad Weather Conditions

When bad weather conditions, such as rain, snow or fog are present the laser power can not be transferred as efficiently as in clear weather conditions. The loss of efficiency is caused by the increase of water in the air, which absorbs and scatters more laser power than normal. To make sure enough laser power can reach the aircraft, an estimation of the transmittance τ is made for different visibilities $\breve{V}$. The transmittance in these conditions for near infrared wavelengths has been investigated by Isaac I. Kim et al. with as result an experimental relation, given by equation 3.3 [16].

$$\begin{aligned} \sigma &= \frac{3.91}{\breve{V}} \left(\frac{\lambda}{550} \right)^{-q} \\ \tau(r_{UAV}) &= \frac{P(r_{UAV})}{P(0)} = e^{-\sigma \cdot r_{UAV}} \end{aligned} \tag{3.3}$$

Where:

σ	Attenuation value		km^{-1}
$\breve{V}$	Visibility through the air		km
λ	Wavelength of emitted laser light	830	nm
q	Size distribution of the scattering particles		
	– For high visibility ($\breve{V} > 50$ km)	1.6	[-]
	– For average visibility (1 km $< \breve{V} <$ 50 km)	1.3	[-]
	– For haze visibility (1 km $< \breve{V} <$ 6 km)	$0.16\breve{V} + 0.34$	[-]
	– For mist visibility (0.5 km $< \breve{V} <$ 1 km)	$\breve{V} - 0.5$	[-]
	– For fog visibility ($\breve{V} <$ 0.5 km)	0	[-]
r_{UAV}	Distance between laser base station and UAV		km
$\tau(r_{UAV})$	Transmittance of air in different weather conditions		[-]

The results for different weather conditions are made and presented in figure 3.14(a) and figure 3.14(b). As can be seen from the figure, the distance between the UAV and the laser base station is critical for a good transmission of power trough the air. For clear conditions the ratio of transmission over 50 km is 0.8 as predicted in the previous section. More important is the dramatic loss in the range of low visibilities, because laser power beaming over long distances is then too inefficient. To cope with the problem of dense fog, three cases are identified and presented in table 3.3.

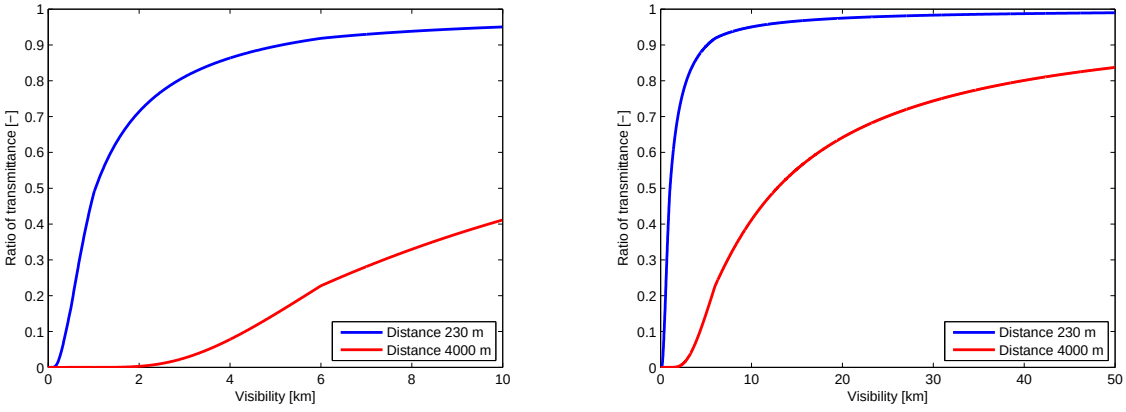

(a) Transmittance through air for 0 km $< \breve{V} <$ 10 km.

(b) Transmittance through air for 0 km $< \breve{V} <$ 50 km.

Figure 3.14: Overview of transmission through air for wavelength $\lambda = 830$ nm. The two different rangens are plotted for the sake of readability in the lower visibility part.

Table 3.3: Different cases of flight for the visibility through the air due to water vapor.

Case	Visibility	Mode of the UAV
1	$\breve{V} > 15$ km	Normal operation of the UAV with normal flight path. Lower transmittance is compensated by batteries and by beaming more power.
2	1.5 km $< \breve{V} < 15$ km	Fly to nearest laser base station and circle around it to collect enough power required to stay in flight. When visibility rises to 15 km resume normal flight path.
3	1.5 km $> \breve{V}$	Not enough power can be transferred to the UAV, thus a landing procedure is started. Fly the UAV to the nearest landing site and land to ensure safety.

3.3 Characteristics of the PV Cells

The second main part of the system is the array of PV cells. The cells provide direct current to the electric system. First the selection of the PV cells is done, then the safety is assessed. Due to the fact that a part of the laser power is converted to heat, a cooling method is analysed.

3.3.1 Selection of Photo Voltaic Cells

With high efficiency GaAs cells, optimised for laser wavelengths between 820 and 850 nm, efficiencies of 56% are demonstrated [17]. Besides providing power to the UAV in an efficient way, the high power input to power output ratio has the advantage of generating less heat, thus decreasing the mass of the insulation and preventing the use of an extra cooling system. GaAs cells have a maximum operating temperature of 400 °C [18], thus this temperature may not be exceeded otherwise permanent damage will be inflicted on the cells.

3.3.2 Analysis of Safety for Laser Power Beaming

Reflection of the PV cells is considered due to safety concerns. The maximum permissible exposure (MPE) for long periods of time ($> 30 \cdot 10^4$ s) is $MPE_{\lambda=830nm} = 6.1\ \mathrm{W} \cdot \mathrm{m}^{-2}$, thus the reflection coming from the UAV has to be lower, otherwise the system is not considered safe. With Snell's law from equation 3.4 and the Fresnel equation from equation 3.5 the reflection index R is calculated and presented in figures 3.15(a) and 3.15(b).

$$\frac{\sin\theta_i}{\sin\theta_t} = \frac{n_2}{n_1} \Leftrightarrow \theta_t = \arcsin\left(\frac{n_1 \sin\theta_i}{n_2}\right) \tag{3.4}$$

$$R = \frac{1}{2}\left(\left|\frac{\mathrm{n}_1\cos\theta_i - n_2\cos\theta_t}{n_1\cos\theta_i + n_2\cos\theta_t}\right|^2 + \left|\frac{n_1\cos\theta_t - n_2\cos\theta_i}{n_1\cos\theta_t + n_2\cos\theta_i}\right|^2\right) \tag{3.5}$$

Where:

θ_i	Angle of incidence		rad
θ_t	Angle of refraction		rad
n_1	Refractive index for air	1.000293	[-]
n_2	Refractive index cover plate of the PV cells	1.51	[-]
R	Reflection index for unpolarised light		[-]

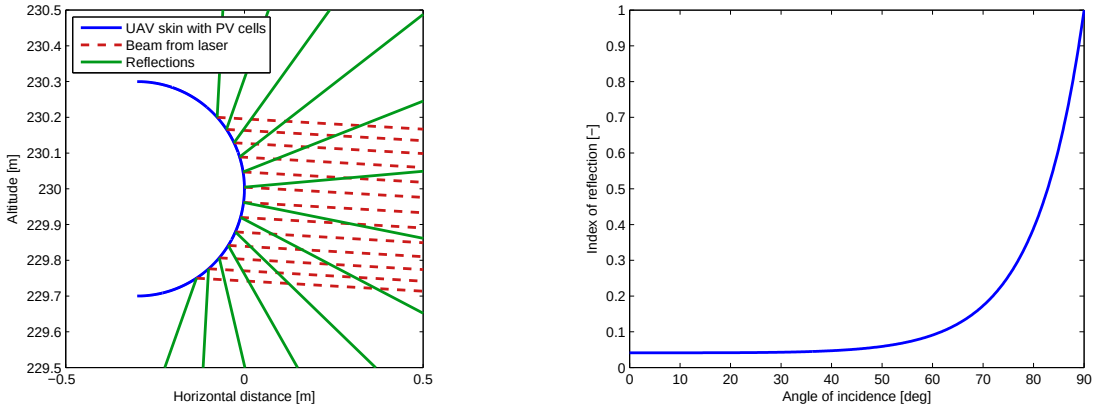

(a) Reflection on the fuselage.

(b) Index of reflection for $0° \leq \theta_i \leq 90°$.

Figure 3.15: Overview of the reflection on the UAV.

Now the reflection and power on the PV cells is known, the reflected laser power at ground level can be calculated. By dividing the reflected laser power with the ground area and taking earlier defined atmospheric losses into account the laser power at ground level is obtained. For different situations the results are summarised in table 3.4.

Table 3.4: Results from the calculations for cases with different distances, bank angles and beam errors.

r_{UAV} [m]	μ [°]	e_{beam} [m]	P_{grid} [W]	P_{loss}/P_0 [-]	$T_{PV\ cells}$ [°C]	$P_{max,\ ground}$ [W · m^{-2}]
500	0	0.00	$8.77 \cdot 10^3$	0.030	162	0.233
500	0	0.10	$8.76 \cdot 10^3$	0.030	162	0.375
500	15	0.00	$8.75 \cdot 10^3$	0.030	162	0.602
500	15	0.10	$8.83 \cdot 10^3$	0.030	162	1.01
4000	0	0.00	$10.8 \cdot 10^3$	0.219	162	0.341
4000	0	0.10	$10.9 \cdot 10^3$	0.219	161	0.582
4000	15	0.00	$10.9 \cdot 10^3$	0.219	162	0.138
4000	15	0.10	$12.1 \cdot 10^3$	0.219	158	0.284

Where:

r_{UAV}	Distance between laser base station and UAV	m^2
μ	Bank angle of UAV	°
e_{beam}	Vertical beam error in meters	m
P_{grid}	Power required from electric grid	W
P_{loss}/P_0	Factor of atmospheric losses at clear conditions	[-]
$T_{PV\ cells}$	Temperature of PV cells	°C
$P_{max,\ ground}$	Maximum reflected laser power per unit area	W · m^{-2}

3.3.3 Cooling Methods and Insulation of the PV cells

From the efficiency of the GaAs PV cells of 56% and 4% minimum reflectivity follows that a maximum of 40% of the laser power is converted to heat. The PV array will lose this heat to the moving air and by radiation defined in the Stefan-Boltzmann law as can be seen from equations 3.6 [19] and 3.7 respectively. The total heat loss is obtained by adding these equations as can be seen in equation 3.8.

$$\dot{Q}_{conv} = 0.332\frac{A}{L}\sqrt{\frac{\rho V L}{\mu}}\sqrt[3]{\frac{c_p \mu}{k}}(T_s - T_f) \tag{3.6}$$

$$\dot{Q}_{rad} = \sigma \epsilon A(T_s^4 - T_f^4) \tag{3.7}$$

$$\dot{Q}_{total} = \dot{Q}_{conv} + \dot{Q}_{rad} \tag{3.8}$$

Where:

A	Area of one PV array		m^2
L	Length of the PV array in direction of flight		m
ρ	density of air, ISA (230m)	1.198	$\mathrm{kg \cdot m^{-3}}$
V	Velocity of the UAV	27.78	$\mathrm{m \cdot s^{-1}}$
μ	Dynamic viscosity of air, ISA (230m)	$1.804 \cdot 10^{-5}$	$\mathrm{kg \cdot m^{-1} \cdot s^{-1}}$
c_p	Specific heat of air	$1.005 \cdot 10^{3}$	$\mathrm{J \cdot kg^{-1} \cdot K^{-1}}$
σ	Stefan-Boltzmann constant	$5.670373 \cdot 10^{-8}$	$\mathrm{W \cdot m^{-2} \cdot K^{-4}}$
ϵ	Emissivity of PV array [20]	0.85	[-]
T_f	Outside temperature, ISA (230m)	286.65	K
T_s	Temperature of the panel		K
$\dot{Q}_{conv}$	Heat transfer by convection		W
$\dot{Q}_{rad}$	Heat transfer by radiation		W
$\dot{Q}_{tot}$	Total heat transfer		W

By filling in the equations and iterating, the panel temperature T_s is obtained. Fortunately the panel temperature is lower then the maximum operating temperature, making the use of an additional cooling system superfluous. The material used in the fuselage is a composite which can have a maximum temperature of 156 °C [21]. Therefore insulation has to be applied when the temperature of the PV cells reaches this temperature. Insulation in the form of glass wool has been selected, because it has a low thermal conductivity of $k_{wool} = 0.04\ \mathrm{W \cdot m^{-1} \cdot K^{-1}}$ [22] and a low density of $\rho_{wool} = 50\ \mathrm{kg \cdot m^{-3}}$. For small temperature differences equation 3.9 applies in which d is the thickness of the insulation.

$$\dot{Q} = kA\frac{\Delta T}{d} \tag{3.9}$$

For a panel temperature of 160 °C a 0.2 mm insulation layer is needed, making the total thickness of the PV cells 1.4 mm with an insulation mass of 0.011 kg.

3.4 Conclusion

The total mass of the system on the UAV, consisting of the PV array, with a mass per unit area of $MPA = 0.89\mathrm{kg \cdot m^{-2}}$ [23], and the insulation is 1.06 kg. The area of the cells on the fuselage is given by the accuracy of the laser aiming system and the structural and aerodynamic limitations. The laser aiming system needs at maximum 0.36 m in height of the UAV and the length of 1 m on the fuselage. Including a safety factor and considering the banking angle the PV cells on both sides will be 1.18 m^2 and will be powered by a 4.5 kW laser which needs 9.1 kW from the grid. The cost of the laser and PV cells are over EUR 300,000 [24] and over EUR 15,000 [25] respectively. The power required from the grid for the laser per year is around 75,000 kWh with an operational cost of around EUR 6,000, calculated with a fee of 0.08 $\mathrm{EUR \cdot kWh^{-1}}$ [26].

CHAPTER 4

AIRCRAFT DESIGN

Aircraft design is a complex and iterative process. Small changes can have a big impact on the design. In the early stage of the project, a fixed wing canard aircraft was chosen to be the aircraft that would operate in the network and would fulfil the mission.

The concept generation, selection procedure and trade off process is described in the Mid term report [5]. The canard configuration was chosen from three other concepts. The other concepts were a blimp, a blended wing body and Prandtl plane. The criteria on which the decision was based are the power required, safety, complexity and handling. The major reasons for choosing a canard configuration are briefly summarised below.

The first reason is that a well designed canard configuration has a lower induced drag with respect to conventional configurations. This is mainly caused by the fact that a canard generates positive lift to provide stability instead of generating negative lift, which is the case for conventional tail configurations. The wing of conventional configurations must generate more lift to compensate for this negative lift component. This results in more induced drag, because more lift results in more drag. The canard does not have to compensate for this negative lift component and therefore the wing needs to generate less lift, meaning less induced drag. This is an important design parameter because a lower drag will result into less power required, which means that the motor can be smaller. Next to that, smaller batteries and a less powerful laser is required.

The most important and most influencing part of the design is the integration of the energy collection system. The laser beaming technology is discussed in chapter 3. To recap, the energy from the laser will be converted by photovoltaic cells into electricity. As described in chapter 3, the PV cells need to be curved to avoid laser hazards. Furthermore they require a large area. The PV cells could either be mounted underneath the aircraft or integrated into the fuselage. Integrating the PV cells into the fuselage is advantageous because less parasite drag is generated and a large curved area can be achieved. For a canard configuration, the available area for the PV cells on the fuselage is generally larger than that of conventional configurations. This is because the wing and canard are positioned at the far ends of the fuselage which results in ample space for the PV cells to be positioned in the middle of the fuselage. By positioning the wing and canard high on the fuselage, the line of sight of the laser beam with the PV cells is assured in turning flight with a small bank angle.

A combination of an electric motor and propeller was chosen to generate thrust for the aircraft. The propeller is placed at the back of the fuselage. This is chosen because it eliminates the interference with the payload cameras in the front and a clear line of sight with the ground can be guaranteed concerning the aircraft itself. Another reason for choosing a push propeller is to shift the centre of gravity further to the back. This is advantageous for the canard size, which will be discussed in section 4.3.

The final result of the conceptual design is presented in figure 4.1.

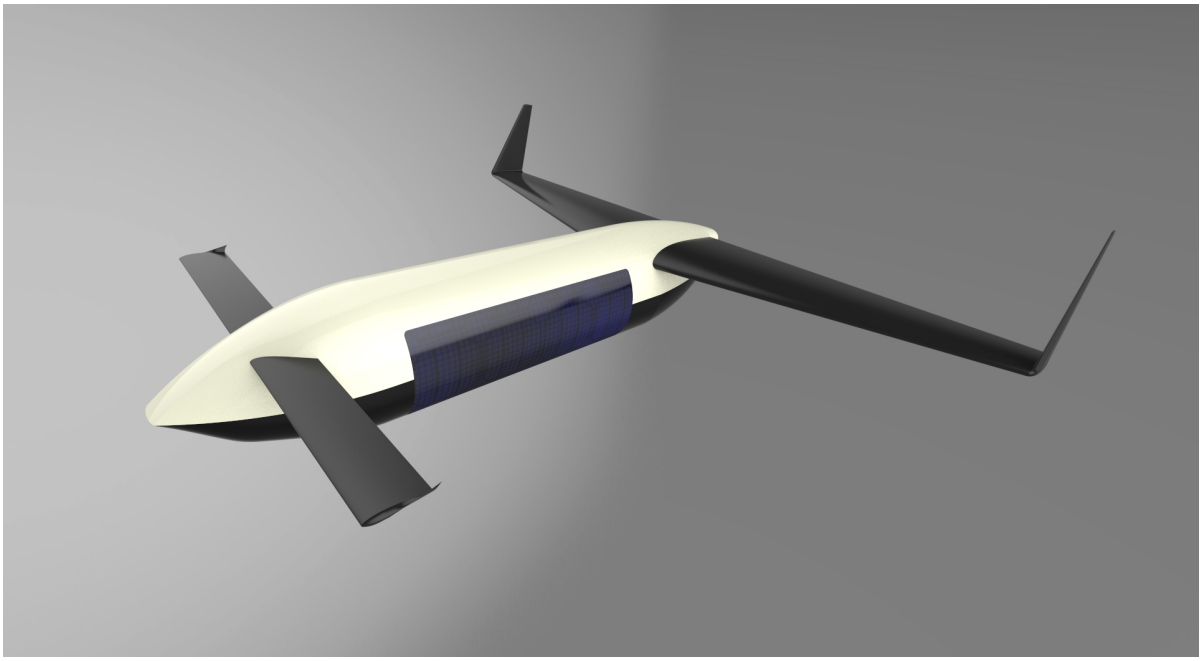

Figure 4.1: The final result of the conceptional design is a high wing canard configuration with push propeller and fuselage integrated photovoltaic cells. Note that the shape of the fuselage nose as well as the canard wing tips are artist impressions of a possible detailed design. These features are not designed at this conceptual design stage.

It was mentioned before that the design process is an iterative process. The design process of the aircraft start with the aerodynamic design of the wing, fuselage, canard and vertical stabilisers. The result from this are the dimensions of each component. With these dimensions the structure can be designed, which will lead to a better estimation for the weight of each component. Another result from the aerodynamic design is the power required. With this specification, the propulsion system is designed after which the electric system will be designed. The weights of the systems are updated during every iteration. The outcome of the design depends on the estimated values which are used for the first iteration. These values are estimated in the early stage of the project. In appendix C the final design is summarised.

Because the aerodynamic design is a complex and iterative process, the design process is elaborated on with a flow diagram that is displayed in figure 4.2. First the preliminary sizing will be performed in section 4.1.1. This correspond with the first step in figure 4.2. After this, the wing will be designed from aerodynamic and structural prospective in section 4.1. After this the fuselage is sized in section 4.2. This is followed by the canard design in section 4.3. Subsequently the design of the vertical stabilisers is discussed in 4.4. To conclude the aerodynamic design, the lift and drag predictions are presented in section 4.5. This section is then followed by the design of the propulsion system in section 4.6 and the electric system in section 4.7.

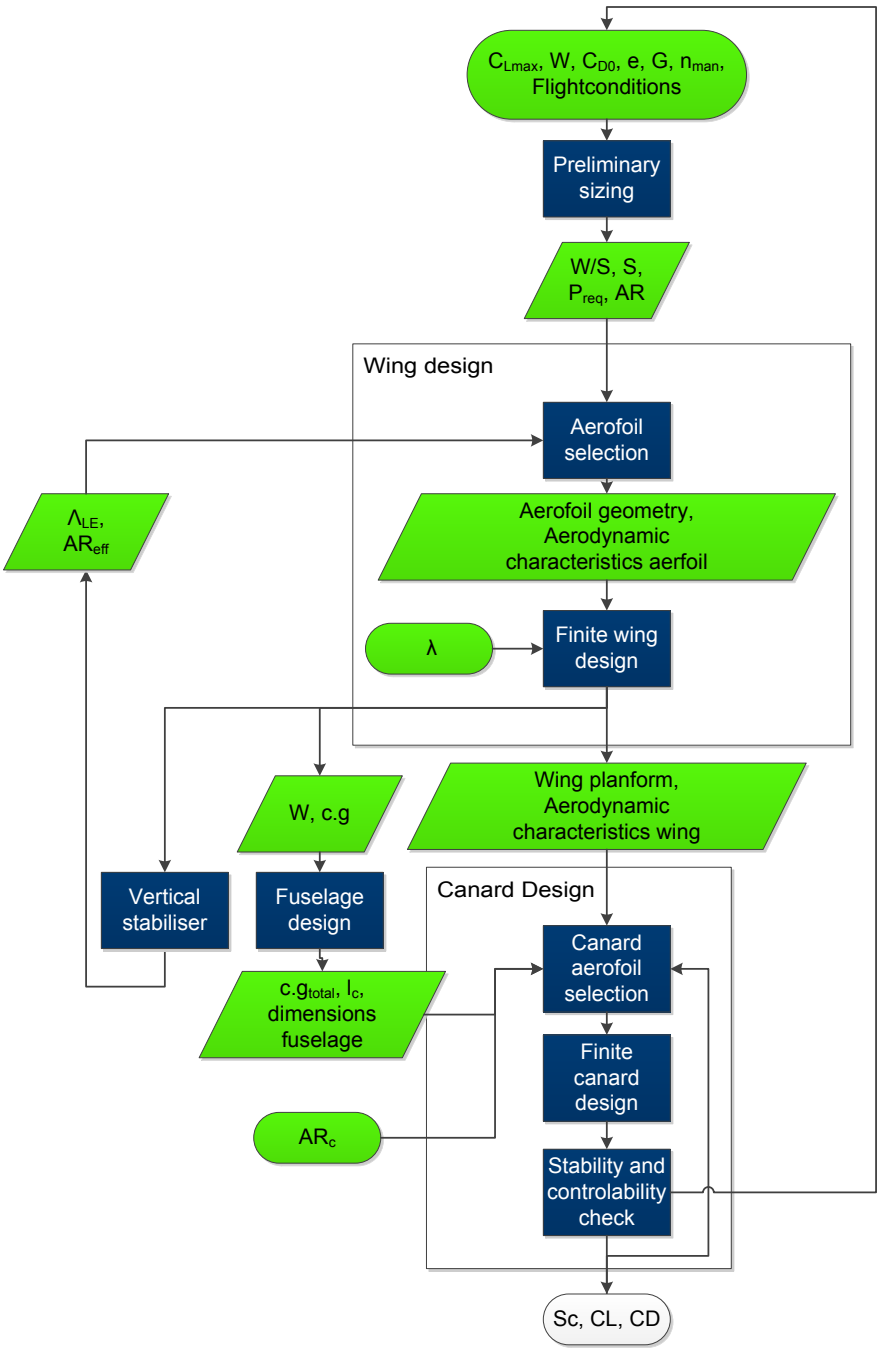

Figure 4.2: Flow diagram of the aircraft design process. The steps are indicated in blue and inputs are indicated in green. Initial inputs are indicated in an oval text box and the outputs from the design steps are indicated in a parallelogram.

4.1 Wing

The wing determines for a large part the performance of the aircraft and therefore of the whole system. The wing design is thus an important step in the design process. In figure 4.2 the steps are presented. This section will start with the preliminary sizing, after which the aerofoil will be selected. Subsequently

the wing planform will be designed. Then the ailerons will be discussed and the load factors will be determined, which can be used during the structural design of the wing.

4.1.1 Preliminary Sizing

The goal of preliminary sizing is to calculate the wing loading W/S and the power loading W/P of the aircraft using the wing loading versus power loading diagram as shown in figure 4.3. From this the surface area S of the wing and the power required P_{req} can be calculated if the weight of the aircraft W is known. The aspect ratio AR of the wing also follows from the diagram. The method that is used to obtain the wing and power loading is described in reference [27] and [28].

The first step is to determine the flight conditions. These flight conditions consist of the density ρ, the Reynolds number Re and the Mach number M. The values are determined using the International Standard Atmosphere. The flight conditions are important during the aerofoil selection. The cruise velocity is 100 km/h and the altitude during cruise is 230 m. The landing conditions are at mean sea level flying at the stall speed of 60 km/h. The Reynolds number must be calculated over a length, which is the taken to be the mean aerodynamic chord length MAC from the last iteration. In table 4.1 the flight conditions are summarised for the wing and canard.

Table 4.1: Flight conditions of the wing and canard for cruise and landing conditions.

Condition	ρ [**kg·m**$^{-3}$]	Re [-]	M [-]
Landing wing	1.225	$5.3{\cdot}10^5$	0.05
Cruise wing	1.198	$8.7{\cdot}10^5$	0.08
Landing canard	1.225	$1.7{\cdot}10^5$	0.05
Cruise canard	1.198	$2.8{\cdot}10^5$	0.08

Different sizing cases are outlined in reference [27] and [28] for the construction of the wing loading versus power loading diagram. Only the sizing cases for stall speed, climb gradient, rate of climb and manoeuvres are applicable for this aircraft design. The landing and take off sizing cases are not considered, because a winch is used for launch and a net is used for recovery of the aircraft.

For the stall speed case the stall speed V_s, the maximum lift coeficient $C_{L_{max}}$ and the conditions during landing are required to calculate the wing loading. The curve does not depend on the power loading.

For the climb gradient case all the parameters that determine the drag coefficient are required. These are the drag coefficient at zero lift C_{D_0}, aspect ratio AR and Oswald efficiency factor e. These values are first obtained from reference aircraft and updated at every iteration. The climb gradient is take a bit higher than 8.3%, which is the minimum required for certification the CS-23 [1]. This is advantageous because the UAV operates in a crowded area and better climb performance will lead to better obstacle avoidance. The value of the climb gradient is set to 10.5%, because with this climb gradient, the climb gradient and climb rate curves in figure 4.3 intersect the stall speed curve at the same location. This means that for neither of these two requirements the aircraft is overdesigned.

The climb rate case requires an estimation of the climb speed V_y at which the best climb rate is achieved. Next to that, the same variables are required as for the climb gradient.

Finally, for the manoeuvring case a maximum manoeuvring load factor need to be determined. The maximum bank angle in scanning mode is 15 °. However, in order to quickly avoid obstacles, a required maximum bank angle of 45 ° is estimated. For a steady turn this means that the manoeuvring load factor is 1.41. This is considered to be sufficient, because the aircraft does not have to perform steeper turns or aerobatic manoeuvres.

In table 4.2 the values are showed that were used to obtain the wing loading versus power loading diagram displayed in figure 4.3. In the diagram an area is shaded in which the wing loading and power loading meet the requirements. It is preferred to maximise both the power loading and the wing loading [27]. Hence, the ideal location for the design point is the upper right corner. The optimum wing loading and power loading combination is indicated as the design point in the diagram. The maximum

wing loading is determined by the stall case and the maximum power loading is determined by the climb rate, climb gradient and manoeuvring cases.

Table 4.2: Input values for the wing and power loading calculation. These values were used during the last iteration.

Parameter	Value
V_s [m· s^{-1}]	16.7
V_y [m· s^{-1}]	22.2
$C_{L_{max}}$ [-]	1.3
C_{D_0} [-]	0.038
AR [-]	7.0
e [-]	0.8
G [%]	10.5
μ [°]	45

In figure 4.3 three reference UAVs are displayed, which have approximately the same size, payload and cruise speed. The obtained wing loading approximately corresponds with the wing loading of the reference aircraft. However, the calculated power loading is much larger than that of the reference aircraft. This is probably because the UAVs must perform at a higher manoeuvre load factor or require a better climb performance.

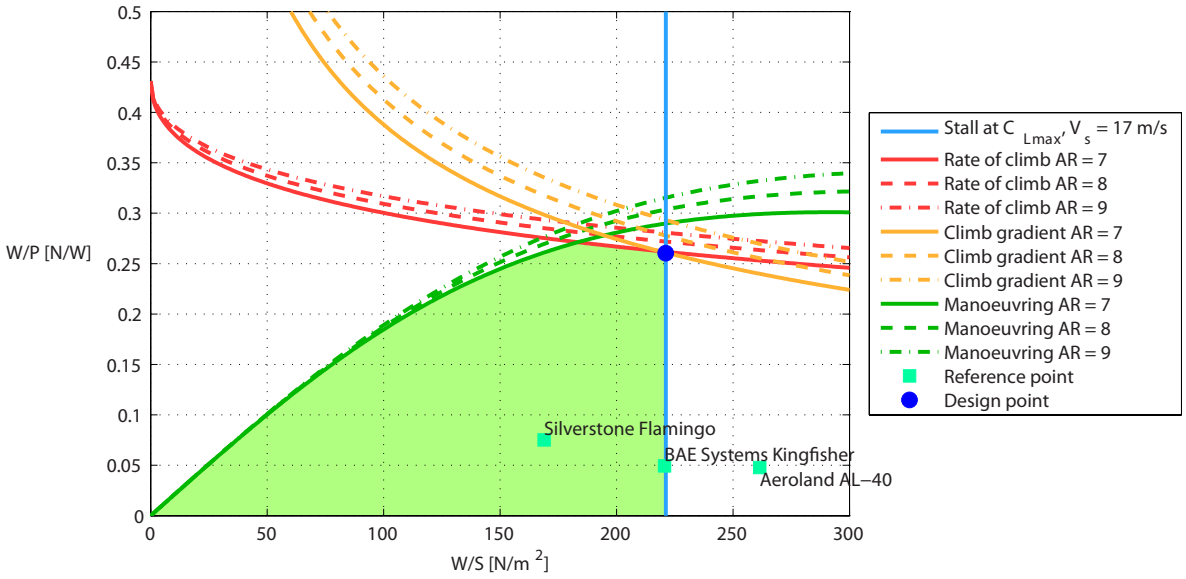

Figure 4.3: Wing loading versus power loading diagram.

Now the design point is chosen and the wing and power loading are obtained, the surface area of the wing S and the power required P_{req} can be calculated using the maximum take off weight W_{TO} of 31.5 kg. The results of the preliminary sizing are presented in table 4.3.

Table 4.3: Resulting wing loading, wing area, power loading and power required from the preliminary sizing of the aircraft.

W/S [N·m^{-2}]	S [m^2]	W/P [N· W^{-1}]	P [kW]
221	1.40	0.25	1.2

4.1.2 Aerofoil Selection

The next step is to select an aerofoil. Since the aircraft is almost continuously in cruise flight, the aerofoil must have the best performance at this flight condition. This means that the aerofoil should have a low drag coefficient at the design lift coefficient. The design lift coefficient of the wing $C_{L_{des}}$ is calculated with equation 4.1 [29].

$$C_{L_{des}} = \frac{2}{\rho V^2} \cdot \frac{W}{S} = \frac{2}{1.198 \cdot 27.8^2} \cdot 221 = 0.48 \tag{4.1}$$

In this equation, ρ is the density in cruise flight, V is the cruise speed of 100 km/h and W/S is the wing loading of the aircraft determined in the previous section.

For canard aircraft, the canard contributes positve lift to the total aircraft lift. Therefore, the required lift coefficient of the wing in cruise could be lowered, because the wing does not have to provide lift for the total aircraft weight. However, no compensation for the canard lift is added (so no decrease in required $C_{L_{des}}$ due to canard lift), because if the aircraft stalls, the canard stalls first. If the $C_{L_{des}}$ of the aircraft is lowered for canard lift, the wing alone will not provide enough lift in case of stall. Hence in case of stall the aircraft would suddenly lose altitude. This can be very catastrophic, especially during landing.

The lift coefficient from equation 4.1 is the lift coefficient of the three dimensional wing. Because for swept wings the aerofoil sees different flow conditions, $C_{L_{des}}$ has to be transformed into the design lift coefficient of the aerofoil $C_{l_{des}}$. The calculation is performed as shown in equation 4.2 [29].

$$C_{l_{des}} = \frac{C_{L_{des}}}{cos^2(\Lambda_{LE})} = \frac{0.48}{cos^2(13.8°)} = 0.51 \tag{4.2}$$

Since this value is close to 0.50, an aerofoil will be selected with a $C_{l_{des}}$ of 0.50. This way the aircraft wing will have a low drag coefficient during cruise. The design lift coefficient is not the only criterion for the selection of an aerofoil. Many other variables are important as well. First of all, the value of the drag coefficient at $C_{l_{des}}$ should be low in order to keep the required power limited. Next to that, the aerofoil should have a high maximum thickness over chord ratio $(t/c)_{max}$. A large thickness ensures a large area moment of inertia of the wing cross section, resulting in smaller stresses in the wing structure. This way the wing mass can be limited. Also, the moment caused by the wing should be small, so that canard size can be limited. The (negative) value of the moment coefficient C_{m_0} thus needs to be small.

A high maximum lift coefficient is required for a low stall speed and for controllability of the aircraft [30]. For the three dimensional wing, a maximum lift coefficient of 1.3 is selected. With this value the planform size and stall speed are limited. The stall speed achieved with the lift coefficient of 1.3 is considered to be sufficiently low to safely loiter over an area and to recover the aircraft using a net. No high lift devices will be installed on the wing, because this adds weight and causes stability problems with canard aircraft. When high lift devices are deployed, the lift vector shifts aft [30]. In this situation the canard lift or its arm should increase to compensate for the larger moment caused by the wing lift force. Methods to assure stability in case of deployed high lift devices are available, but they all add weight.

With the aforementioned criteria, an aerofoil should be selected. For this selection the NACA 4, 5 and 6 series are considered. NACA 4 aerofoils have the most simple shape and therefore a wing built from such an aerofoil is easiest to manufacture. Generally these aerofoils also have a high drag coefficient and large pitching moment coefficient. The NACA 5 aerofoils have a higher maximum lift coefficient and a lower pitching moment. Finally, although NACA 6 aerofoils have the lowest drag, they have higher pitching moment coefficient and their complicated shape makes a wing with such an aerofoil harder to manufacture.

After many iterations, the NACA37014 aerofoil was selected for the wing, because of the limited drag, low pitching moment, high lift coefficient, high thickness and relatively simple shape. The geometry of this NACA 5 series aerofoil is displayed in figure 4.4.

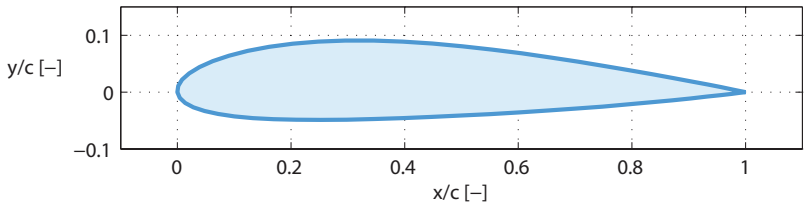

Figure 4.4: Geometry of the NACA37014 aerofoil

In figure 4.5 the lift curves and the C_l-C_d curves of the aerofoil for cruise and landing conditions are shown. These curves are generated using JAVAFoil. Figure 4.6 shows the C_m - α curves of the NACA37014 aerofoil. Table 4.4 displays characteristic parameters describing the curves.

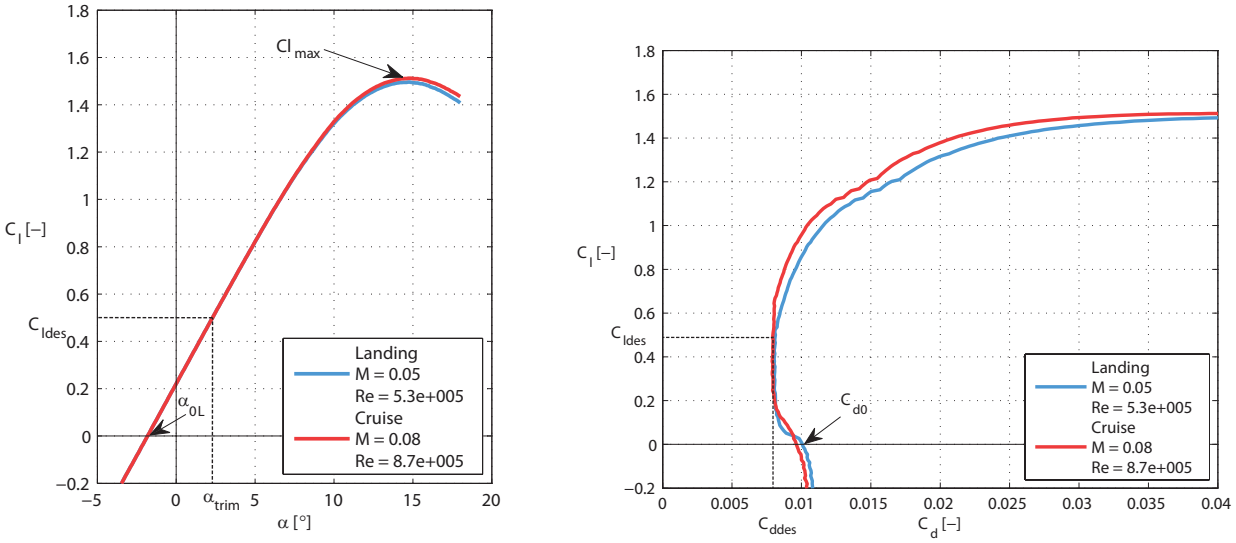

(a) Lift curves.

(b) Lift to drag curves.

Figure 4.5: Lift curves and lift to drag curves of the NACA37014 aerofoil for cruise and landing conditions.

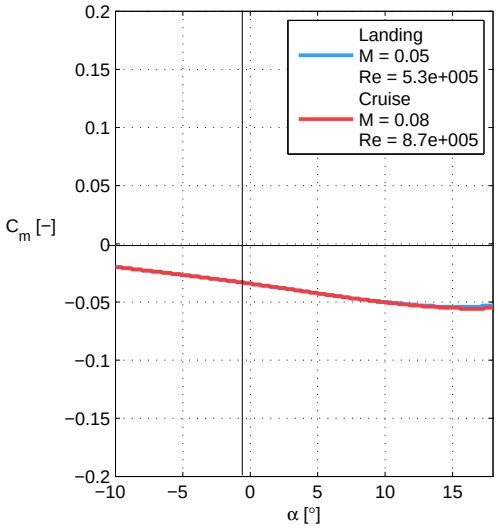

Figure 4.6: Moment coefficient curves of the NACA37014 aerofoil for cruise and landing conditions.

Table 4.4: Lift, drag and moment curve parameters describing the lift, drag and moment curves of the NACA37014 aerofoil. α_{0L} is independent of the flight conditions for the low Mach numbers considered. $C_{l_{des}}$, α_{trim}, $C_{d_{des}}$, C_{d_0} and C_{m_0} are for cruise conditions and $C_{L_{max}}$ is for landing conditions.

α_{0L} [°]	$C_{l_{des}}$ [-]	α_{trim} [°]	$C_{l_{max}}$ [-]	$C_{d_{des}}$ [-]	C_{d_0} [-]	C_{m_0}
-1.8	0.50	2.3	1.50	0.0079	0.0097	-0.033

4.1.3 Planform

Now the area S, aspect ratio AR and the wing aerofoil are determined, the wing planform can be designed. The wing span b follows from the area and aspect ratio. The design of the planform geometry influences the lift distribution, induced drag and weight of the wing. The design also influences the stability and controllability of the total aircraft.

To provide lateral stability, the vertical stabiliser of any aircraft should be positioned behind the centre of gravity of the aircraft [31]. Since the centre of gravity is positioned aft in case of canard aircraft, the vertical stabiliser needs to be very large and heavy if no tail is added. A better option is to position two vertical stabilisers at the wing tips of the wing. By employing aft swept wings, the vertical tail arm l_v is increased. The vertical tail arm is the distance between the aerodynamic centres of the wing and vertical stabiliser in the plane of the wing as shown in figure 4.7. Due to the increase in l_v, the area of each vertical stabiliser is less than half the area required for a single vertical stabiliser, which results in a lighter aircraft. The vertical stabilisers positioned at the wing tips also act as winglets, decreasing the induced drag of the wing. Next to that, the mass of the winglets contributes a tip down moment on the wing, acting against the tip up moment caused by the lift distribution. Due to the lower stresses, the wing weight is decreased. So positioning vertical stabilisers at the wing tips has a large influence on the planform design.

For more information on the design of the vertical stabiliser, see section 4.4. The wing planform design is shown in figure 4.7. This figure also shows the canard and vertical stabiliser planforms, which will be discussed in section 4.3 and section 4.4, respectively. The figure depicts the mean aerodynamic chords with length MAC and aerodynamic centre positions as well. The aerodynamic centre is assumed to be positioned at a quarter of the chord length. Table 4.5 shows the various geometric parameters defining the wing planform.

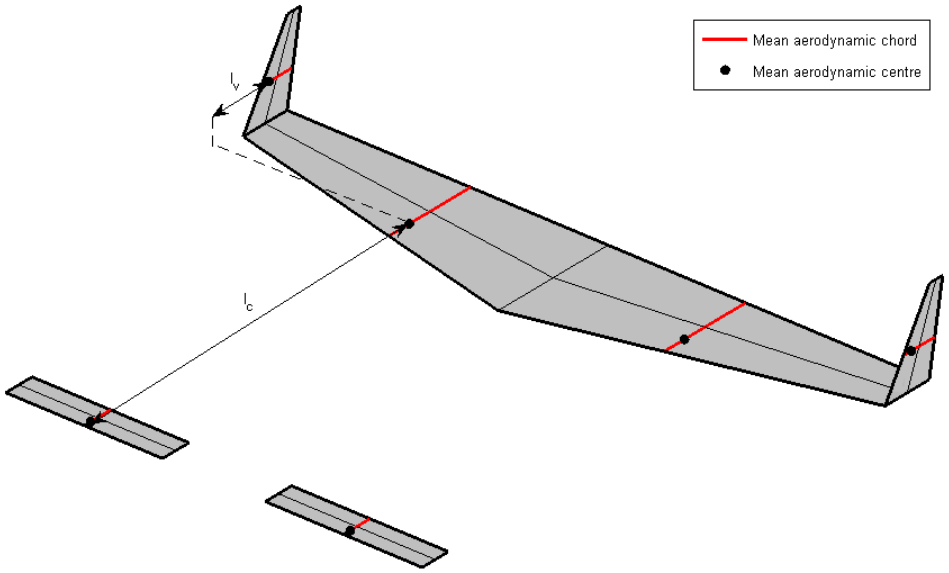

Figure 4.7: Wing, canard and vertical stabiliser planform geometry including mean aerodynamic chords and aerodynamic centre positions. The horizontal tail length l_c and vertical tail length l_v are indicated as well.

Table 4.5: Planform dimensions and parameters describing the wing of the aircraft.

S [m^2]	AR [-]	AR_{eff} [-]	b [m]	λ [-]	c_r [m]	c_t [m]	Λ_{LE} [°]	$\Lambda_{0.5c}$ [°]	Λ_{TE} [°]	MAC [m]
1.40	7.0	8.4	3.10	0.40	0.64	0.25	13.8	7.0	0.0	0.47

The taper ratio λ of the wing equals 0.40. This value is higher than the value found in historic trend lines [32]. However, in this case it is advantageous to have a larger tip chord length c_t. Because a larger tip chord yields a larger vertical stabiliser area for the given shape, the resulting sweep angle of the wing is kept limited.

With this taper ratio, the lift distribution should still be nearly quasi-elliptical, limiting induced drag [32]. By employing taper in the wing design, the wing weight is decreased in comparison to a rectangular wing. This is because for a tapered wing a larger part of the lift is produced near the root chord , resulting in a shorter arm. This decreases the bending moment acting on the wing. With the combination of taper and sweep used in this wing design, no tip stall is expected to occur [32]. This is important since tip stall can cause sudden rolling of the aircraft while rendering the ailerons ineffective [32].

The leading edge sweep angle Λ_{LE} of the wing equals 13.8°. There are two reasons for applying sweep to the wing. The first reason for applying sweep is to increase the vertical tail length l_v of the vertical stabilisers. The second reason is to keep the canard aspect ratio limited and with it the canard weight. To prevent canard aircraft from entering deep stall, the canard should stall before the wing does [30]. Hence the stall angle of the wing should be larger than that of the canard. The stall angle is largely determined by the lift gradient of the three dimensional wing. To achieve large stall angles, low lift gradients are required. By increasing the (effective) aspect ratio or by decreasing the sweep angle, the lift gradient of the wing is increased. To let the canard reach stall conditions first, the (effective) canard aspect ratio should be higher than that of the wing. However, by applying sweep to the wing, the required canard aspect ratio is decreased, lowering the canard weight.

There are a number of disadvantages as well to applying sweep to the wing. At the low cruise Mach number of 0.08, sweep is not required to avoid wave drag. Due to the applied sweep, a higher $C_{l_{des}}$ is

required, which inevitably increases drag. Next to that, the wing weight increases by applying sweep, because now an additional torque is generated as well by the lift distribution. For ease of manufacturing, the wing is designed such that the trailing edge sweep angle Λ_{TE} of the wing equals 0.0°. This required only a very small decrease in the calculated leading edge sweep angle.

The design of the wing is simplified by not applying twist and setting the dihedral angle and wing incidence angle equal to 0°. The latter means that the fuselage is at the same angle of attack as the wing, which somewhat increases the drag of the fuselage. However, as can be seen in figure 4.21, this increase in drag is negligible.

Since the vertical stabilisers also act as winglets, less strong trailing vortices are induced. The resulting decrease in induced drag is accounted for by using an effective taper ratio AR_{eff} of 8.4, which is 1.2 times the geometric aspect ratio AR [33].

In order to judge the structural feasibility of the wing design, the cantilever ratio CR is calculated in equation 4.3 [32].

$$CR = \frac{b/2}{(t/c)_{max}\ c_r\ cos\Lambda_{0.5c}} = \frac{3.1/2}{0.14 \cdot 0.64 \cdot cos\ 7.0^\circ} = 17.6. \tag{4.3}$$

In this equation, c_r is the root chord length and $\Lambda_{0.5c}$ is the half chord sweep angle. For aircraft of various weight categories the cantilever ratio has typical values between 18 and 22 [32]. The calculated cantilever ratio is considered to be sufficiently close to these values. Even though the effects of the vertical stabilisers at the wing tips is not accounted for, the wing structure is expected to be feasible.

4.1.4 Lift Curve

The next step in the wing design is the determination of the lift curves in landing and cruise conditions. Due to three dimensional effects associated with the finite wing, the wing lift curve differs from the aerofoil lift curve. The wing lift curves are constructed from various parameters calculated using the DATCOM method [34]. Table 4.6 shows the parameters describing the curves. These parameters are also indicated in figure 4.8(a) and 4.8(b) which show the resulting lift curves in cruise and landing conditions, respectively. Note that the actual shape of the stall region cannot be determined using the DATCOM method. The curvature shown is only an approximation.

Table 4.6: Lift curve parameters describing the lift curves of the wing. α_{0L} and C_{L_α} are independent of the flight conditions for the low Mach numbers considered. $C_{L_{des}}$ and α_{trim} are for cruise conditions and $C_{L_{max}}$, α_s and $\Delta\alpha_{C_{L_{max}}}$ are for landing conditions.

α_{0L} [°]	C_{L_α} [rad^{-1}]	$C_{L_{des}}$ [-]	α_{trim} [°]	$C_{L_{max}}$ [-]	α_s [°]	$\Delta\alpha_{C_{L_{max}}}$ [°]
-1.8	4.44	0.48	4.4	1.28	16.8	2.0

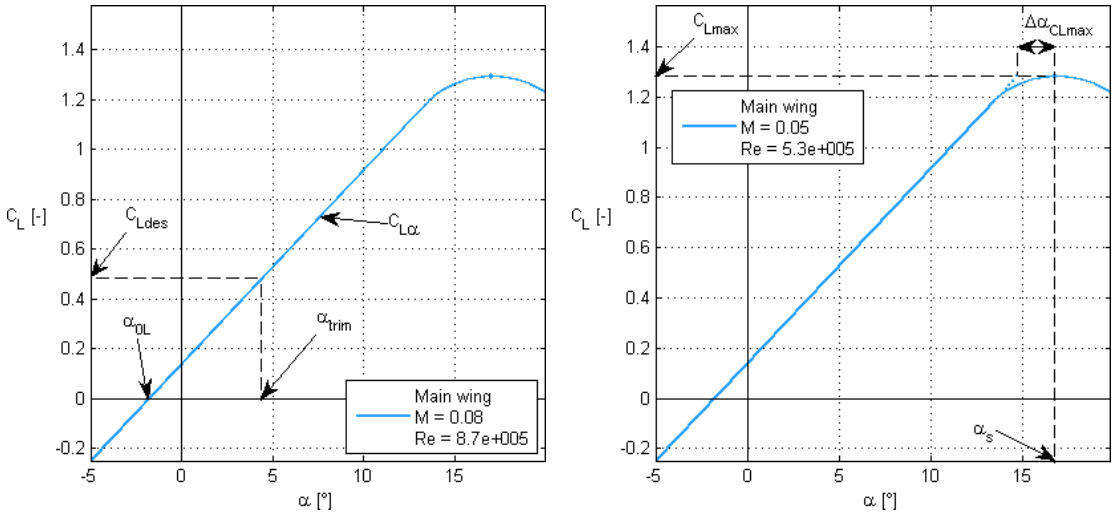

(a) Lift curve for cruise conditions.

(b) Lift curve for landing conditions.

Figure 4.8: Lift curves of the wing constructed using the indicated parameters from table 4.6.

The zero lift angle of attack α_{0L} of the finite wing is equal to that of the aerofoil. The wing lift gradient C_{L_α} is lowered by the finite effective aspect ratio and sweep angle of the finite wing and increased by compressibility effects. For the low Mach numbers considered here, the compressibility effects can be neglected. The wing lift gradient is further lowered by the downwash generated by the canard. Since the canard is positioned more than two wing mean aerodynamic chord lengths ahead of the wing, the effects are accounted for by using equation 4.4 [30].

$$C_{L_{\alpha_{downwash}}} = C_{L_\alpha}(1 - \frac{2C_{L_{\alpha_c}} S_c/S}{\pi AR}) \tag{4.4}$$

In this equation, $C_{L_{\alpha_{downwash}}}$ is the lift gradient of the wing in the downwash of the canard and C_{L_α} and $C_{L_{\alpha_c}}$ are the lift gradients calculated using the DATCOM method of the wing and canard, respectively. S_c/S is the ratio of the canard surface area and wing surface area and AR is the wing aspect ratio.

The design lift coefficient $C_{L_{des}}$ and trim angle of attack α_{trim} the aircraft flies on in cruise are also indicated in table 4.6 and figure 4.8. The four aforementioned parameters are independent of the incompressible flight conditions considered for the aircraft. On the other hand, the values shown for the maximum lift coefficient $C_{L_{max}}$, the stall angle of attack α_s and angle of attack range in stall $\Delta\alpha_{C_{L_{max}}}$ depend on the sweep angle and shape of the aerofoil and are all in landing condition. This is important, because with the higher Reynolds number in cruise, these values would be overestimated if this flight condition was used. The stall angle of attack of the wing is pretty large, which is required because the canard needs to stall first. This large stall angle assures that the required canard aspect ratio is limited.

4.1.5 Ailerons

The primary function of ailerons is to give the aircraft a roll motion. The ailerons shall be mounted on the wing. To achieve the highest efficiency, the ailerons shall be mounted near the tips because then the distance between the centre of gravity and the force generated by the ailerons will be maximised. Another reason to have the ailerons near the tips is to make sure that it stays outside the disturbed flow of the foreplane.

A guideline to size the ailerons according to the dimensions to the wing can be found in [35]. From [35] it is found that the chord ratio of the ailerons over the chord ratio of the wing (C_a/C_w) is 0.15-0.25 and the span ratio b_a/b_w is 0.2-0.3. In this case, it is favourable to have b_a to be low to stay outside the disturbed flow of the foreplane.

From wing design the dimension of the wing is determined. For sizing the ailerons, one side of the wing is used as reference to obtain the dimension of one aileron. Each wing half will contain one aileron. The parameters of the wing are summarised in table 4.7.

Table 4.7: Parameters of one half of the wing

Parameter	Value
$S_w/2$ [m^2]	0.7
$C_w/2$ [m]	0.255
$b_w/2$ [m]	1.55

Note that the tip of the wing chord is used due to the fact that the ailerons will be mounted near the wing tips. To minimise b_a, b_a/b_w is set to be 0.2. Then b_a is 0.31 m, which means that it stays out of the disturbed flow of the foreplane, since it was calculated that the distance between the foreplane tip to wing tip is 0.574 m. The next step is to determine C_a and the value of C_a/C_w will be chosen as 0.25 to ensure that there is enough aileron surface left. This gives a C_a of 0.064 m. Finally the surface of the aileron is $C_a \cdot b_a$ which is 0.02 m^2. At last it is recommended that the maximum deflection of the ailerons is $\pm 30°$.

4.1.6 Load diagrams

The last part before the wing can be designed structurally is to determine the load factors to which the aircraft is subjected. Load factors can be determined by following certification standards. No certification standard is developed for UAVs at the time this project was executed. The normal procedure is to follow the current standards and check whether it applies on the system of interest. This aircraft will follow the current CS-23 standard [1]. This is the general aviation certification. CS-25 was not chosen because it is for large turbine aircraft and CS-VLA was not chosen because the aircraft must also operate during daylight [36].

To determine the load factors the following velocities have to be introduced. V_a is the speed the manoeuvring speed, V_s is the stall speed and n_c is the load factor at cruise speed. V_a must not be lower than $V_s\sqrt{n_c}$, which is 27.5 m·s^{-1} and be not larger than V_c [1]. V_a is chosen to be equivalent to V_c, because the aircraft must be capable to give full deflections of the control surfaces during cruise. V_b is the design speed for maximum gust intensity. This has the requirement that it must be the value of $V_s\sqrt{n_c}$. V_d is the dive speed, this is commonly M_c+0.05 [37], which result into 44.8 m·s^{-1}.

Table 4.8: Overview of the velocities used for the loading diagram.

Velocity type	**Velocity [m· s^{-1}]**
V_s	16.7
V_a	27.8
V_b	27.5
V_c	27.8
V_d	44.8

For the gust loading calculation the gust velocity must be defined. This is given by the certification standards [1] and displayed in table 4.9. With the method described by the certification standard a load factor diagram can be constructed. This is displayed in figure 4.9.

Table 4.9: Gust velocities that are used to determine gust loading. Velocities are obtained from certification standard CS-23 [1].

Velocity	**Gust velocity [m· s^{-}1]**
V_b	20
V_c	15
V_d	8

From this the maximum and minimum load factors can be determined, which are 4.0 and -2.0 respectively. Certification states that a safety factor of 1.5 must be added. But since this maximum load factor is already relative high compared to general aviation [37], this will be omitted. No turns will be executed above 45 degrees and if gust speeds will become high the aircraft can land within a few minutes.

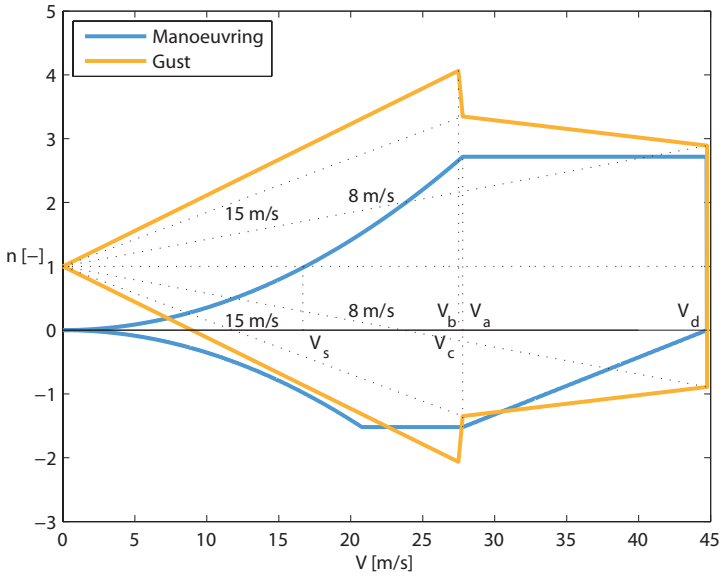

Figure 4.9: Load diagram for manoeuvring and gust loading used for the structural design of the wing.

4.1.7 Structure

In this section the method for determining the structure of the wing is explained. By analysing what forces the wings are subjected to and the stresses associated with them, the minimum strength of the structure can be specified. This is done by varying certain structure dimensions, e.g. skin thickness or selecting a material with an appropriate ultimate strength. Subsequently with the dimensions and material density known the mass of the structure is determined. The weight of the structure also contributes to the stresses in the structure so this analysis is iterated until an optimal solution is found. This analysis is performed in Matlab such that easy iteration is possible.

Material

The material considered for the wing structure is the HexPly® M21 pre-impregnated composite by Hexcel [38], which is commonly used in primary aerospace structures. It comprises of a toughened epoxy resin with either unidirectional or woven carbon or glass fibres. The pre-preg considered for this analysis, which is designated as M21/40%/285T2/AS4C-6K in reference [38], consists of a carbon fibre two by two twill, which is a type of weave. This twill basically has fibres running in two directions

perpendicular to each other, which make a pattern of diagonal ribs. The ply thickness of the pre-preg equals 0.285 mm, however according to laminate design rules [39] several plies per laminate are necessary to ensure sufficient damage tolerance, aero-elastic stiffness, bolted joint strength and the capability to carry loads. The minimum thickness of the laminate is thus about 1 mm.

To manufacture the final shape of the wing the pre-preg is applied to a mould and then placed in vacuum to cure. An autoclave is required to purge out residual gasses. However, a new process called Out-of-Autoclave [40], where only a vacuum bag at atmospheric pressure is used, reduces the costs for producing composite structure while increasing performance. With this process composite structures achieve less than one percent void content and autoclave quality mechanical properties, which is required for primary aerospace structures. The material structural properties are listed below.

- Tension Strength: 885 MPa
- Tension Modulus: 67.6 GPa
- Laminate Density: $1.56 \cdot 10^{-6}$ kg·mm^{-3}

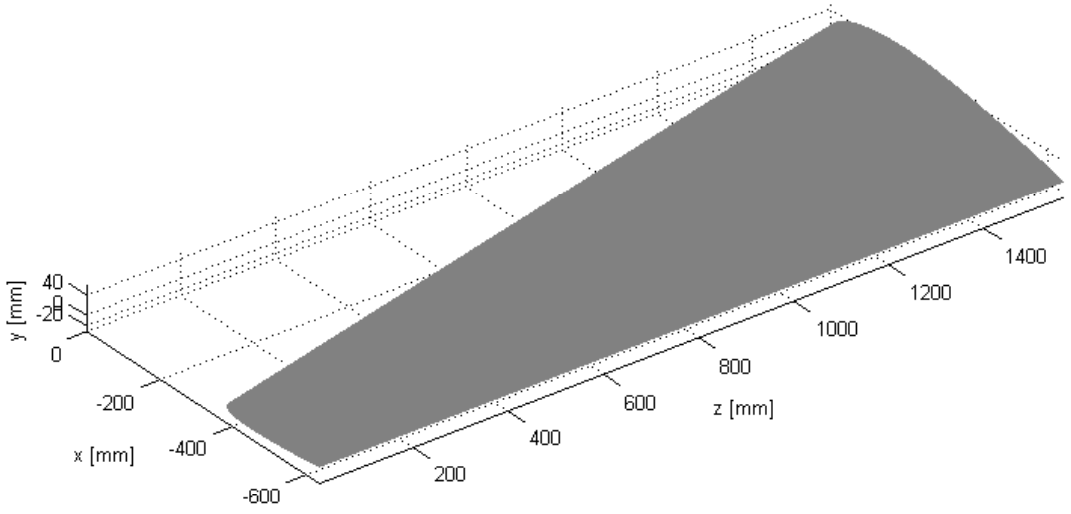

Figure 4.10: Reference frame for the wing.

Forces

The forces acting on the wing are the aerodynamic forces and the weight. In order to find the value of these forces several initial assumptions have to be made. These assumptions include an initial aircraft total weight, a composite material with a density of $1.56 \cdot 10^{-6}$ kg·mm^{-3}, an ultimate tensile strength of 885 MPa, and a minimum skin thickness of 1 mm.

With these assumptions the wing weight can be estimated more accurately. First the wing structure is generated in Matlab using the x and y coordinates of the aerofoil obtained from JavaFoil and the wing planform dimensions found in table 4.5. For each millimetre in span wise direction a wing cross section, with a thickness of 1 mm, is calculated such that the different x, y and z coordinates obtained define the wing structure. The result of this can be seen, together with the reference frame in figure 4.10. Next the skin length of each cross section is calculated as the distance between each point outlining the profile. With an initial skin thickness of 1 mm and the total skin length, the skin cross sectional area

of each section is known. Then the skin volume at each section can be determined as it was assumed that the sections have a thickness of 1mm. Multiplying each section volume with the material density results in a mass per cross section. Adding the masses of each cross section gives the total mass of one wing.

The lift force over two wings is assumed to be eighty percent of the total lift force. This total lift force is found using the maximum load factor that affects the UAV during flight, which is 4 and multiplying it with the total aircraft weight. The forces in y direction are thus the distributed lift force on the wing, the distributed weight of the wing, the remaining weight of the aircraft located at the root and the weight of the vertical stabiliser located at the wing tip.

The forces in x direction is the distributed drag force which is determined with the least favourable lift-to-drag ratio.

Bending Stress

With the forces in the direction of the principle axes known the stresses in the structure are calculated. First the normal stresses due to bending are determined using equation 4.5 [41].

$$\sigma_z = \frac{I_{xx}M_y - I_{xy}M_x}{I_{xx}I_{yy} - I_{xy}^2}x + \frac{I_{yy}M_x - I_{xy}M_y}{I_{xx}I_{yy} - I_{xy}^2}y \tag{4.5}$$

The structure is idealized for each cross section, i.e. the skin is lumped into boom areas. This method assumes that shear stress is uniform through the thickness of the skin and the direct stress carrying capability of the skin is represented as separate booms. This simplification is a discretization of the structure and is performed such that numerical evaluation is possible. With the boom areas of the idealized structure known the second moments of area I_{xx}, I_{yy} and product moment of area I_{xy} for each cross section is calculated. The moments M_x and M_y are determined for each cross section as the forces influencing bending in that cross section. For M_x this includes the lift and weight, and the drag force determines M_y. The normal stress in each boom at each cross section is then calculated with equation 4.5 where x and y are the distances of the boom to the neutral axis in x and y direction respectively. The highest stresses are found in the cross section located at the root of the wing.

Shear Stress

The shear stresses in the skin of the wing are determined by shear forces and torsional moments. First the shear forces are considered. The wing is tapered which introduces additional forces in x and y direction due to the normal force in the booms. These forces and the lift and drag forces contribute to the shear forces S_x and S_y. Using equation 4.6 the open section shear flow in the skins can be calculated per cross section.

$$q_b = \frac{I_{xx}S_x - I_{xy}S_y}{I_{xx}I_{yy} - I_{xy}^2}\sum_{r=1}^{n} B_r x_r \; + \frac{I_{yy}S_y - I_{xy}S_x}{I_{xx}I_{yy} - I_{xy}^2}\sum_{r=1}^{n} B_r y_r \tag{4.6}$$

Closing the section adds the constant shear flow determined with equation 4.7. The total shear flow in the skin due to the shear forces is equal to the addition of the two previous shear flows, see equation 4.8.

$$S_x\eta_0 - S_y\xi_0 = \oint q_b p ds + 2Aq_{s,0} \tag{4.7}$$

$$q_s = q_b + q_{s,0} \tag{4.8}$$

Torsion also causes shear stresses in the skin of the structure. The torsion of each cross section is caused by the shear forces in the other sections. The shear flow due to this is constant in the skin of the cross section and is determined with equation 4.9

$$\mathcal{T} = 2Aq_T \tag{4.9}$$

The total shear flow in each cross section is the constant shear flow due to torsion and the shear flow in the skin due to the shear forces. Dividing this shear flow by the skin thickness where the shear flow acts results in the shear stress. The highest shear stresses are found at the root of the wing.

The Von Mises yield criterion, calculated with equation 4.10, is compared with the ultimate tensile strength of the material. When the von Mises is lower than the ultimate strength, then the structure is capable of coping with the applied forces. If not, then either the skin thickness can be increased where necessary or a different material with a higher ultimate tensile strength can be chosen. The Von Mises stress distribution on the wing can be seen in figure 4.11.

The final iteration has a maximum von Mises stress of 80 MPa, with a uniform skin thickness of 1 mm. With a material yield strength of 885 MPa, this configuration is thus strong enough to cope with the flight loads. The structural weight of the wings equals 4.5 kg. There are, however, other types of failure modes, e.g. delamination, which are not analysed in this report but can have a significant impact on the structure. Further analysis of these failure modes is recommended.

$$Y = \sqrt{\frac{1}{2}[(\sigma_x - \sigma_y)^2 + (\sigma_y - \sigma_z)^2 + (\sigma_z - \sigma_x)^2] + 3\tau_{xy}^2 + 3\tau_{yz}^2 + 3\tau_{xz}^2} \tag{4.10}$$

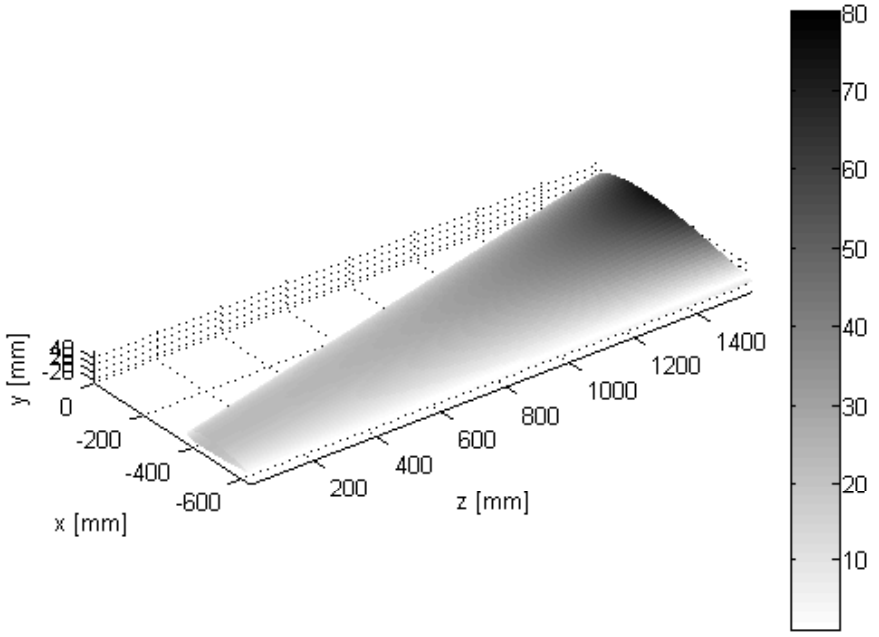

Figure 4.11: Von Mises stress distribution, in MPa, over the wing.

4.2 Fuselage

Now the wing design is discussed, the fuselage design can be elaborated. In the introduction of this chapter several design factors of the fuselage are already mentioned. The main factor is the integration of the PV cells on the side of the fuselage. Another important factor is to have sufficient space inside the fuselage to store all subsystems. Section 4.2.1 contains the fuselage layout, the weight and location of the centre of gravity of each subsystem. The result in the end of this section is the location of the centre of gravity of the total aircraft. The location of centre of gravity is an important variable for the design of the canard. Therefore it is treated before the canard design. After the layout and centre of gravity are determined the structural design will be discussed.

4.2.1 Fuselage Layout

As mention earlier a curved area in required for the PV cells to spread the laser beam and therefore avoiding laser concentrations. The shape of a cross section the fuselage is circular with a radius of 0.25 m. A circular cross section is chosen to avoid flow separation. Shape corners can cause flow separation, which occur even at small angle of attack or sideslip [42]. The front is a cone and the back is designed such that air is guided to the propeller root. Detailed design on these parts in not performed.

The distance between the aerodynamic centre of the wing and canard l_c, is also a design variable. This is important for the stability of the aircraft. The length of the total fuselage is an estimation based on the fineness ratio. This ratio is the ratio between the diameter and the length of the fuselage. Based upon single engine aircraft a fineness ratio of 0.2 was chosen [42]. This resulted into a fuselage length l_f, of 2.5 meters. The location of the leading edge of the canard root chord was estimated to be at 10% of the fuselage with respect to the nose of aircraft. And by placing the wing at the back, so the trailing edge of the wing at 100% of the fuselage with respect to the nose the distance between the aerodynamic centre of the wing and the canard is maximised.

In figure 4.12 the assigned location and volume of the subsystems is displayed. This is an estimation and the figure is not to scale.

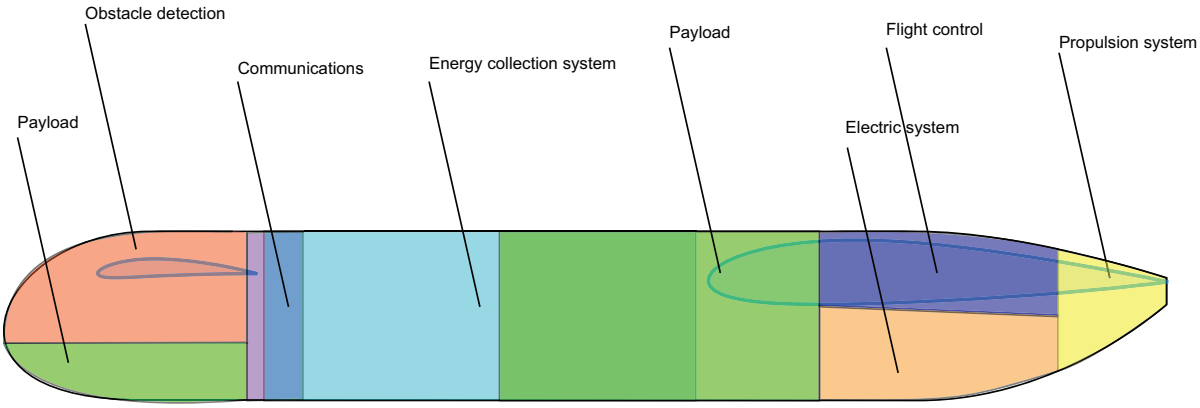

Figure 4.12: Side view of the fuselage with the volumes assigned to the systems.

From this layout an estimation of the position of the centre of gravity can be performed. The weight of each system was estimated or calculated in the previous or upcoming sections and with the location of the centre of each component the total centre of gravity can be estimated. The location of each center of gravity $c.g$, is given as a percentage of the fuselage with respect to the nose of the fuselage.

In table C.3 the weights are given with the corresponding location of the centre of gravity.

Table 4.10: Mass of the systems and the location of the c.g.

Group	**Component**	**Mass [kg]**	**Location c.g in % of l_f [-]**	**Location c.g in [m] from the nose**
Fuselage	Electric System	4.5	85	2.1
	Propulsion system	0.5	100	2.6
	Pv cell	1.3	50	1.3
	Structure	6.4	58	1.5
	Communications	0.6	30	0.8
	Obstical detection	0.7	10	0.3
	Cannard	1.1	10	0.3
	Flight control	0.5	83	2.1
	Total fuselage	15.8	61	1.5
Wing	Structure	4.5	91	2.3
	Control Surfaces	0.1	98	2.5
	Vertical Stabilizer	0.8	95	2.4
	Total wing	5.4	92	2.3
Payload		10.3	60	1.5
MTOW		31.5	66	1.6

Now the dimensions of the fuselage are determined, the fuselage can be designed from a structural perspective.

4.2.2 Structures

This section will discuss the method for determining the fuselage structure w.r.t. the applied loads. It is analogous to the method for determining the wing structure, with the differences being the shape and forces applied on the structure.

Materials

The material considered for the fuselage is GG N026J, a bio composite material manufactured by GreenGran [21]. The granules are based on polypropylene and natural fibres. This material can be used with standard injection-moulding devices, so a fuselage shape can be easily made with the required moulds. The material combines high stiffness and strength with excellent thermal properties. It has a flexural strength of 80 MPa, a density of $1.09 \cdot 10^{-6}$ kg$\cdot$ mm^{-3} and a heat deflection temperature of 156 °C at a load of 45 N$\cdot$cm^{-}1. As the data sheet only states the flexural strength, the tensile strength is assumed as 55 percent of the flexural strength. The tensile strength is required for comparison with the von Mises stress. The 55 percent is derived from data sheets of similar materials [43]. The thermal property is particularly relevant because heat is generated on the PV cells by the laser beam and they are located on the fuselage. Also the fact that the material consists of natural fibres makes it a sustainable product.

Forces

The forces on the fuselage consist of of the lift force and the weight of the structure and the internal weight of the subsystems and payload. The lift force is equal to the maximum load factor, which is 4, times the total weight of the aircraft which was initially equal to 28 kg. It acts on the fuselage at the location of the wings and canards. To determine the weight of the fuselage structure, the shape is first specified. It is assumed that the fuselage can be approximated by an open cylinder with a radius of 0.25 m and a length of 2.5 m. The largest part of the fuselage has this shape except for the front and end. In Matlab the cylinder is generated with circular cross sections per millimetre in length wise direction. The

initial skin thickness is assumed 1.5 mm as this is the minimum thickness that can be manufactured. Assuming a uniform skin thickness around the fuselage and using the density of the material, the total structural weight of the fuselage equals 6.4 kg.

Stresses

The method for calculating the bending and shear stresses in the fuselage uses the same formulas for calculating the stresses in the wing structure found in section 4.1.7. The highest stresses on the fuselage structure are due to bending. The Von Mises stresses are calculated such that failure can be determined. This stress distribution can be seen in figure 4.13.

The highest stress from the last iteration is 6 MPa with a skin thickness of 1.5 mm, which does not exceed the maximum strength of the proposed material.

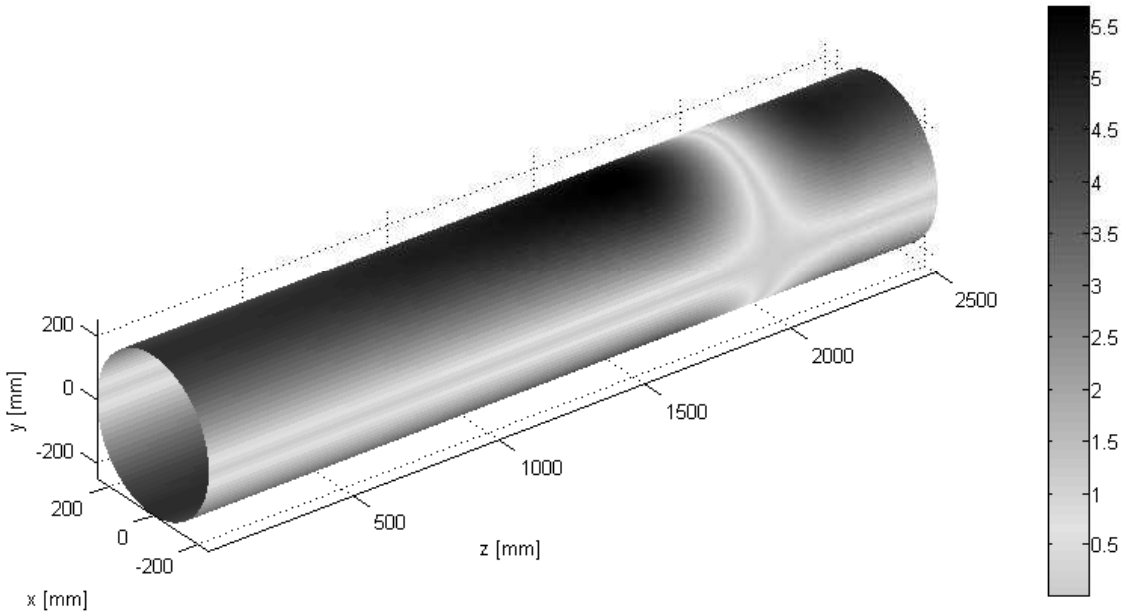

Figure 4.13: Von Mises stress distribution, in MPa, over the fuselage.

4.3 Canard

The next step in the aircraft design is the sizing of the canard. The main function of the canard is to ensure longitudinal stability of the aircraft. The design of the canard is a difficult and very iterative process, because it depends on the mass and position of the other subsystems of the aircraft and the forces and moments generated by the wing and fuselage. Another difficulty with the canard design is that the range in which the centre of gravity can operate is very small. However, for this electrically powered aircraft using batteries, the centre of gravity does not vary during flight. In this section, first the selection of the aerofoil used for the canard is elaborated on. Secondly the planform will be presented. This is followed by the lift curves of the canard and wing. Finally the stability and controllability of the aircraft will be discussed.

4.3.1 Aerofoil selection

In the wing design section an aerofoil was selected based upon the $C_{L_{des}}$. The design of the wing and the canard are closely related, but the canard is not designed upon the design lift coefficient. The canard must have a high $C_{L_{max}}$ at a lower stall angle of attack than the stall angle of attack of the

wing. Whether this requirement is satisfied or not depends on the canard aerofoil and planform designs of the canard and wing. Therefore the canard aerofoil selection is not driven by properties such as its thickness or drag. However, these are taken into account. For the canard the NACA4411 aerofoil is selected. The cross section of the aerofoil is displayed in figure 4.14. Using this aerofoil, the stability and controllability of the aircraft is ensured while limiting the canard size. A cambered aerofoil is chosen since it has a low zero lift angle of attack. This assures that the three dimensional canard has a low stall angle of attack as required. The NACA 4 series aerofoils are also easy to manufacture.

In figure 4.15 the lift curves and lift to drag curves are shown for cruise and landing conditions as obtained from analysis using JAVAFoil. These curves show irregular behaviour at the low Reynolds numbers considered. By slightly increasing the Reynolds number, the curves suddenly show continuous behaviour. Therefore, the curves are estimated by a dashed line. Table 4.11 displays characteristic parameters obtained from these curves.

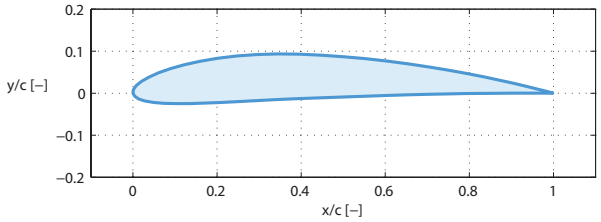

Figure 4.14: NACA 4411, aerofoil of the canard

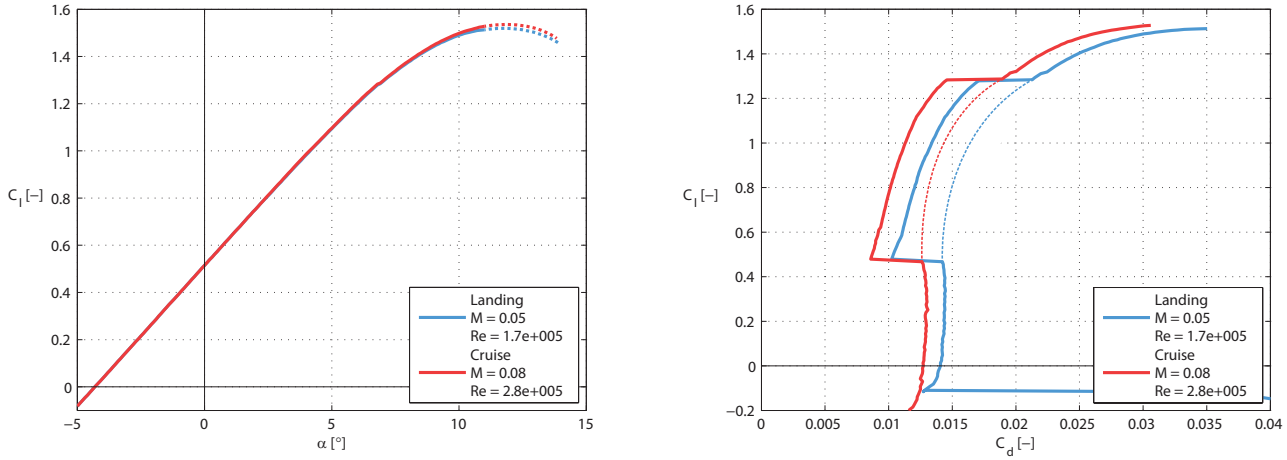

(a) Lift curves.

(b) Lift to drag curves.

Figure 4.15: Lift curves and lift to drag curves of the NACA4411 aerofoil for cruise and landing conditions.

Table 4.11: Lift and drag curve parameters describing the lift and drag curves of the NACA4411 aerofoil. α_{0L} is independent of the flight conditions for the low Mach numbers considered. C_{d_0} is for cruise conditions and $C_{L_{max}}$ is for landing conditions.

α_{0L} [°]	$C_{l_{max}}$ [-]	C_{d_0} [-]
-4.3	1.52	0.0126

4.3.2 Planform

The design of the canard planform is an iterative process which involves the stability, controllability and centre of gravity position of the aircraft and the design of the main wing. The canard area S_c is determined using the stability and controllability curves. As mentioned before, the canard should stall before the main wing does. Although the stall angle of attack depends also on the aerofoil, it depends most on the aspect ratio and sweep angle of the planform via the lift gradient [34]. The canard is thus designed such that it meets the stability, controllability and stall requirements. The result is shown in figure 4.7 and table 4.12.

Note that the reference area of the canard is that of the exposed planform; it does not extend into the fuselage [33]. Therefore, in table 4.12 the semi span $b/2$ of one canard surface is given, while the area is the summed area of the two canard surfaces.

Table 4.12: Planform dimensions and parameters describing the canard of the aircraft.

S [m^2]	AR [-]	$b/2$ [m]	λ [-]	c [m]	Λ [°]
0.24	10.0	0.77	1.0	0.15	0.0

The aspect ratio of the canard equals 10.0, which is larger than that of the wing. This is required for the canard lift gradient to be larger than that of the wing so that the canard stalls first. If the wing had no sweep and did not encounter the canard downwash, the canard aspect ratio would have to be even higher.

Although the high aspect ratio makes the canard rather heavy due to the large moment arm, this aspect ratio is simply required to make the canard stall before the wing does. Lowering the canard aspect ratio and applying more sweep to the wing would also make the aircraft satisfy the stall requirement. The canard structure would be lighter in that case. However, the resulting higher design lift coefficient with associated drag increase and lower maximum lift coefficient of the wing are considered to be highly unfavourable consequences.

No sweep is applied to the canard planform, because it would merely have unfavourable consequences. For the low Mach numbers encountered in flight, the flow over the canard will never reach critical conditions with respect to the occurence of wave drag. Sweep would increase the canard weight (larger torsion moment) and lower the maximum lift coefficient and horizontal tail length l_c. For the selected aerofoils of the wing and canard, not applying sweep to the canard means that the angle of attack range in the stall region $\Delta\alpha_{C_{L_{max}}}$ of the canard lift curve is lower than that of the wing lift curve [34]. This favourably increases the distance between the stall angles of attack of the wing and canard lift curve.

Because no taper is applied to the canard, the planform is rectangular. Therefore the root chord, tip chord and mean aerodynamic chord lengths are all equal and are indicated as the chord length c in table 4.12. Although not applying taper makes the canard a bit heavier and the resulting lift distribution is not favourable for induced drag [32], it is easier to manufacture.

The canard does not incorporate twist in its design. It could be required to set the canard at an incidence angle with respect to the fuselage in order to satisfy the stall requirement by lowering the zero lift angle of attack α_{0L}. However, the cambered aerofoil selected not only provides a high maximum lift coefficient, but already has a sufficiently low zero lift angle of attack. Therefore no incidence angle is employed for the canard planform.

4.3.3 Lift Curve

With the aerofoil selected and the planform designed, the lift curves can be constructed. For this purpose, the DATCOM method is used again. Since the canard is more than two wing mean aerodynamic chord lengths ahead of the wing, the upwash of the wing at the canard can be neglected [30]. The parameters describing the curves are shown in table 4.13. The resulting lift curves are shown in figure 4.16(a) for cruise conditions and in figure 4.16(b) for landing conditions. These figures also show the wing lift curves determined in section 4.1.

Table 4.13: Lift curve parameters describing the lift curves of the canard. α_{0L} and C_{L_α} are independent of the flight conditions for the low Mach numbers considered. $C_{L_{max}}$, α_s and $\Delta\alpha_{C_{L_{max}}}$ are for landing conditions.

α_{0L} [°]	C_{L_α} [rad^{-1}]	$C_{L_{max}}$ [-]	α_s [°]	$\Delta\alpha_{C_{L_{max}}}$ [°]
-4.3	4.94	1.36	13.3	1.8

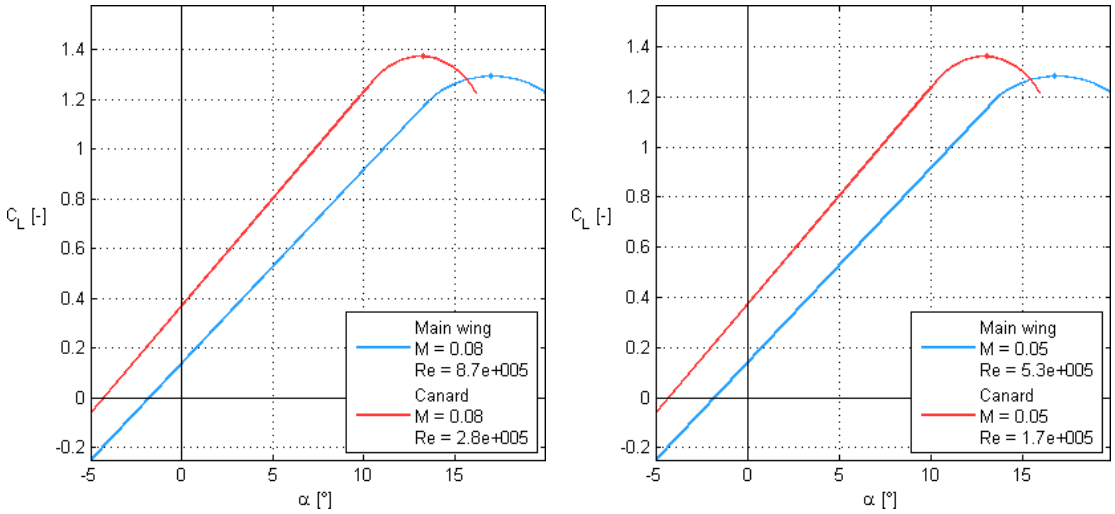

(a) Lift curves for cruise conditions.

(b) Lift curves for landing conditions.

Figure 4.16: Lift curves of the wing and lift curves of the canard constructed using the indicated parameters from table 4.13.

As can be seen from figure 4.16, the combination of aerofoils and planform designs of the wing and canard satisfy the requirement for the canard to stall before the wing does. The difference in stall angle is 3.5°, which should be sufficiently large to ensure a safe recovery from stall situations [44].

The maximum lift coefficient of the canard in landing is rather large. This is required for the controllability of the aircraft. The high maximum lift coefficient limits the required area of the canard and therefore the canard mass and drag.

4.3.4 Stability and Controllability

The main function of the canard is to provide longitudinal stability. In this section it will be explained how this is achieved. The main goal is to determine the ratio between the wing surface and the canard surface Sc/S.

In order to guarantee stability, the derivative of the pitching moment coefficient C_M with respect to angle of attack α must be smaller than zero. This means that with an increase in angle of attack the aircraft must pitch down.

$$C_{M_\alpha} < 0 \tag{4.11}$$

In order to have a longitudinally statically stable aircraft, the centre of gravity $c.g$ must be located ahead of the neutral point $n.p$. The neutral point is defined as the moment centre for which a change in the aircraft angle of attack will result in no change in total moment. If the $c.g$ is located at the $n.p$ the aircraft is neutral stable. In order to prevent neutral stability or unstability a stability margin SM, is introduced. In reference [45] a SM of 0.05 is recommend. Equation 4.12 describes the location at which the centre of gravity must be located x_{cg} in order to provide stability [45]. The bar above, for

example $\bar{x}_{cg}$ means that it is divided by the mean aerodynamic chord MAC. The method to determine the location of the aerodynamic centre $a.c$, of the fuselage and wing divided by the MAC ($\bar{x}_{ac_{wf}}$), can be found in reference [45]. In the equation 4.12 the lift gradient of the finite canard $C_{L_{\alpha_c}}$ is required. This value can be obtained from the previous section. The lift gradient of the finite wing plus fuselage $C_{L_{\alpha_{wf}}}$ can be calculated with equation 4.13. The canard arm (l_c) was determined in 4.2.

$$\bar{x}_{cg} = \bar{x}_{ac_{wf}} + \frac{C_{L_{\alpha_c}}}{C_{L_{\alpha_{wf}}}} \left(1 - \frac{d\epsilon}{d\alpha}\right) \frac{S_c l_c}{S \cdot MAC} \left(\frac{V_{canard}}{V}\right)^2 - SM \tag{4.12}$$

Equation 4.12 is a general equation that is valid for conventional tail plane and canards. The canard has some characteristics that simply this equation. First of all is the canard not subjected to downwash $\frac{d\epsilon}{d\alpha}$ of the wing. If the canard is located close to the main wing (less than two root chords of the wing ahead of the a.c) the canard can be subjected to upwash from the main wing [30]. This is not the case for this design and therefore the upwash can be neglected. This mean that $\frac{d\epsilon}{d\alpha}$ is zero. Secondly the canard is subjected to free stream are and therefore $V_{canard} = V$.

With equation 4.13 $C_{L_{\alpha_{wf}}}$ can be estimated. $C_{L_{\alpha w}}$ is obtained from 4.1 and this lift gradient of the wing corrected for the canard interference. With the fuselage width b_f, wing span b, the wing surface S and S_{net}, which is equal to S minus the projection of the central wing part inside the fuselage, an $C_{L_{\alpha_{wf}}}$ can be calculated.

$$C_{L_{\alpha_{wf}}} = C_{L_{\alpha w}} \left(1 + \frac{2.15 b_f}{b}\right) \frac{S_{net}}{S} + \frac{\pi b_f^2}{2S} \tag{4.13}$$

In table 4.14 the values are displayed with which the stability curve is calculated.

Table 4.14: Used variables to obtain stability curve.

Condition	h
$\bar{x}_{ac}$ [$\%MAC$]	-0.07
l_f [m]	2.5
b_f [m]	0.5
l_c [m]	-1.9
S [m^2]	1.40
S_{net}[m^2]	1.09
MAC [m]	0.47
b [m]	3.1
λ	0.4
$\Lambda_{0.25c}$	10.4
$C_{L_{\alpha_w}}$[rad^{-1}]	4.45
$C_{L_{\alpha_c}}$[rad^{-1}]	4.94
SM	0.05

The next part is to size for controllability. This can be done with the method described in reference [46]. The main equation is presented in equation 4.14.

$$\bar{x}_{cg} = \bar{x}_{ac_{wf}} - \frac{C_{m_{wf}}}{C_{L_{wf}}} + \frac{C_{L_c}}{C_{L_{wf}}} \frac{S_c l_c}{S \cdot MAC} \left(\frac{V_{canard}}{V}\right)^2 \tag{4.14}$$

The maximum lift coefficient of the canard C_{L_c}, can be obtained from the previous section. Two condition are analysed. During cruise and landing, both have different lift coefficients. The moment coefficient of the wing and fuselage $C_{m_{wf}}$ can be determined following the method described in [46]. The values that were used to obtain the controllability curve are showed in table 4.15.

Table 4.15: Used variables to obtain the controllability curve.

Condition	h
$\bar{x}_{ac}$ $[\%MAC]$	-0.07
C_{L_c} cruise	0.5
C_{L_c} landing	1.36
C_{L_0}	0.14
C_{m_0}	-0.033
AR	7.0
AR_c	10.0

The result is presented in figure 4.17. The shaded area is the range in which the aircraft is controllable and stable. The boundary curves are the controllability curve during landing condition and the stability curve with a SM of 0.05. The surface ratio chosen is the surface ratio that has a 0.02 margin with the controllability curve and the intersection with the centre of gravity line. An advantage of this design is that the $c.g$ does not shift, because no fuel or people are on board. There is quite some range where the centre of gravity can be located and still let it be stable and controllable. The centre of gravity can still move to the back. To the front will become more critical.

The found surface ratio is 0.17 [-], which result into a surface area of the canard of 0.23 m^2. The range of centre of gravity at, which the aircraft can operate while staying stable and controllable is from -0.70 to -0.84 x_{cg}/MAC.

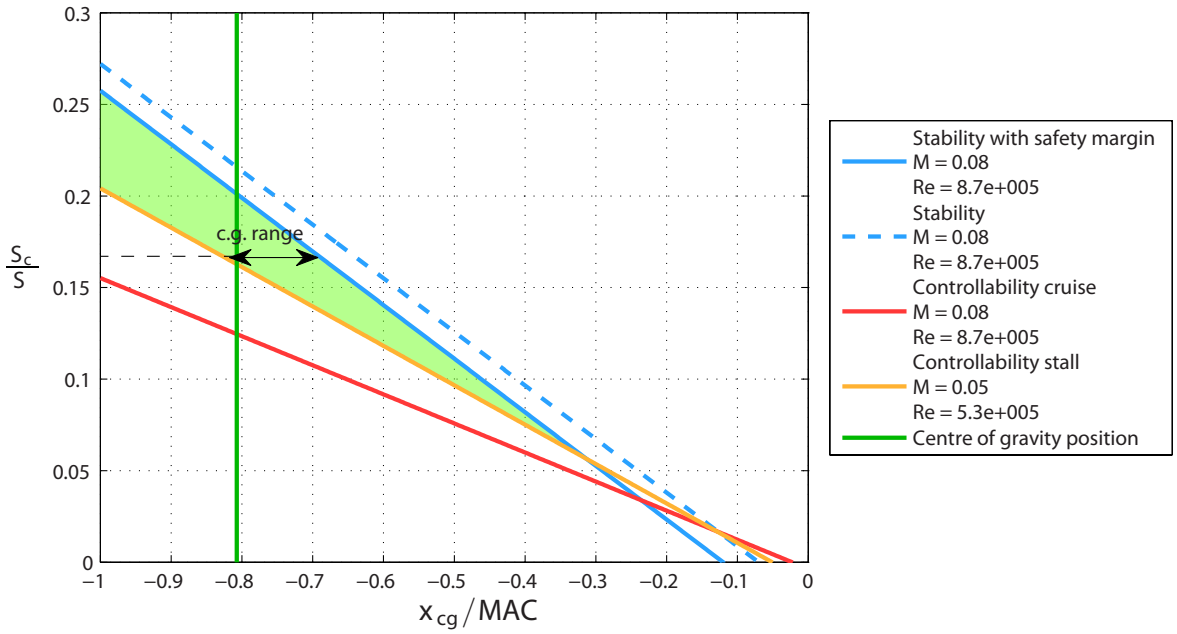

Figure 4.17: Centre of gravity as a fraction of the mean aerodynamic chord versus the ratio between the canard surface and the wing surface.

4.3.5 Elevators

The primary function of the elevators is to control the pitch of the aircraft. It was decided that the aircraft shall be a canard configuration and that the canard will have elevators attached. Typical maximum elevator deflection angles are in the range of -4° to +10° [47].

4.3.6 Structures

The structures for the canard is determined the same way as the wing structure. The difference is that the lift force acting on the canard is assumed 20 percent of the total lift force. The material considered for the canard is the same bio composite material that is chosen for the fuselage. The material properties are stated in section 4.2.2.

The canard dimensions can be found in table 4.12. The Von Mises stress distribution on the canard can be seen in figure 4.18. The maximum strength of the material is 44 MPa and from the final iteration the highest von Mises stress is 28 MPa, with a skin thickness of 1.5 mm. The structure is thus strong enough to handle the applied loads. The structural weights of both canards is 1.1 kg. As for the wing, see section 4.1.7, there are loads which are not considered in this analysis.

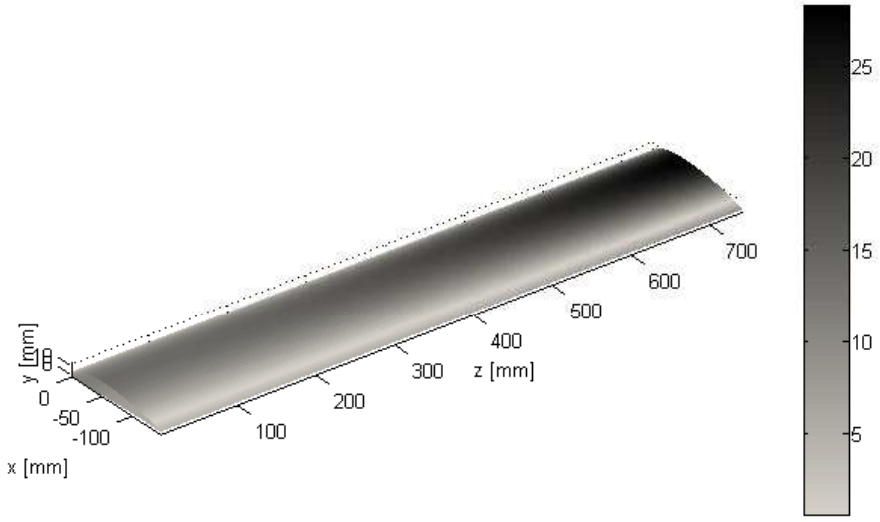

Figure 4.18: Von Mises stress distribution, in MPa, over the canard.

4.4 Vertical Stabiliser

The design of the vertical stabilisers is not considered in great detail in this design phase, because not all required properties of the aircraft are known yet. The shape and size are simply based on reference data. The result is shown in figure 4.7 and table 4.16. Because one vertical stabiliser is actually half of a wing, the table shows the semi span of one vertical stabiliser. However, the area indicated is the summed area of the two vertical stabilisers.

Table 4.16: Planform dimensions and parameters describing the vertical stabilisers of the aircraft.

S [m^2]	AR [-]	$b/2$ [m]	λ [-]	c_r [m]	c_t [m]	$\Lambda_{0.5c}$ [°]	MAC [m]
0.14	5.0	0.41	0.30	0.26	0.08	22.0	0.18

For the estimation of the drag of the vertical stabiliser in section 4.5.2., the zero lift drag coefficient of the aerofoil C_{d_0} is required. Because in symmetric fligth the vertical stabilisers should not produce lift, a symmetric aerofoil is required. For the purpose of acquiring a C_{d_0} value, the NACA 0010 aerofoil is assumed.

For the determination of the vertical stabiliser area S_v, the tail volume coefficient method is adopted [33]. The tail volume coefficient $\bar{V}_v$ is calculated using equation 4.15.

$$\bar{V}_v = \frac{S_v l_v}{Sb} \tag{4.15}$$

In this equation, l_v is the vertical tail length and S and b are the reference area and span of the wing, respectively. Similar aircraft have roughly the same tail volume coefficients. The tail volume coefficient used equals 0.040 and is based on general aviation aircraft [48]. Because the vertical tail length is known from the wing planform design, the reference area of the vertical tail can be calculated. The aspect ratio, taper ratio and sweep angle of the vertical stabiliser are based on reference data as well [33].

4.4.1 Rudder

The rudder is used to control the yawing moment of the aircraft. A rudder shall be mounted on each vertical stabiliser. To get an estimation of the dimensions of the rudders, values from reference aircraft are consulted, which are listed in table 4.17 [49].

Table 4.17: Specifications of rudders from different aircraft.

Aircraft	S_r/S_v [-]	C_r/C_{v_t} [-]	$\delta_{r_{max}}$ [deg]
Cessna 182	0.38	0.42	24
Cessna 650	0.26	0.27	25
Gulfstream 200	0.3	0.32	20
Air Tractor AT-802	0.61	0.62	24
Lockheed Martin C-130E Hercules	0.239	0.25	35
DC-8	0.269	0.35	32.5
Boeing 777-200	0.26	0.28	27.3
Boeing 747-200	0.173	0.22	25
Fokker 100A	0.23	0.28	20
Embraer ERj145	0.29	0.31	15
Airbus A340-600	0.31	0.32	31.6

In this table, S_r/S_v is the ratio of the rudder surface over the vertical stabiliser surface and C_r/C_{v_t} is the rudder chord ratio over the vertical stabiliser tip ratio. Taking the average of the values from table 4.17, the following values can be obtained: $S_r/S_v = 0.3$, $C_r/C_v = 0.33$ and $\delta_{r_{max}} = 25°$. The surface and chord of one vertical stabiliser was determined as 0.07 m^2 and 0.077 m respectively. Using the ratios, S_r and C_r are computed to be 0.021 m^2 and 0.025 m, respectively.

4.4.2 Structures

The vertical stabilisers are placed on the wing, just like winglets. The method for determining the structure of the vertical stabilizers is the same as the method for determining the wing and canard structure, which can be seen in section 4.1.7. The forces on the vertical stabilizers are different in that the lift force acts perpendicular with respect to the weight of the structure. This makes the analysis slightly different. The material proposed for the structure is the same as the material proposed for the canard and fuselage structure, see section 4.2.2.

The dimensions for the vertical stabiliser are found in table 4.16. The following values come from the final iteration. The skin thickness is 1.5 mm and is uniform over the structure. The Von Mises stress distribution on the vertical stabiliser can be seen in figure 4.19. The maximum von Mises on the vertical stabiliser is 20 MPa and the material ultimate tensile strength is 44 MPa. The stress does not exceed the ultimate stress, so the structure is able to cope with the applied loads. The total structural weight of the vertical stabilisers is 0.8kg. Further analysis is required, see section 4.1.7, as not all loads are considered.

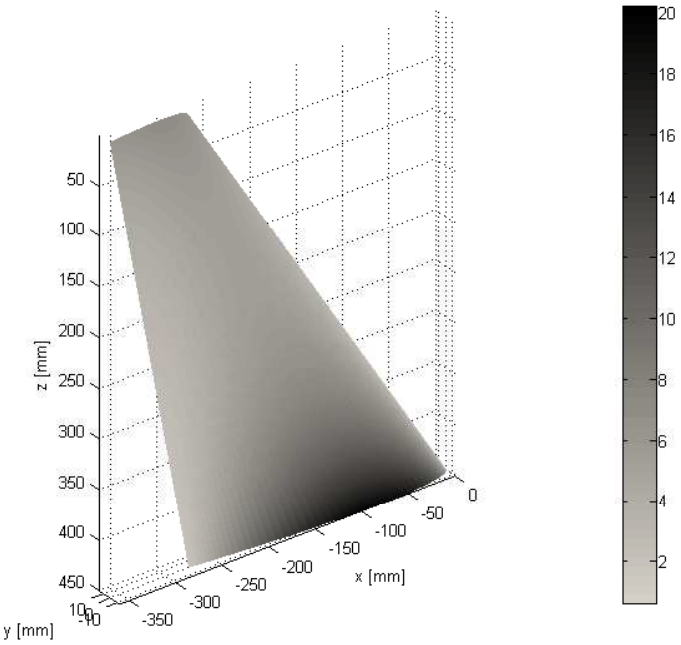

Figure 4.19: Von Mises stress distribution, in MPa, over the vertical stabilisers.

4.5 Aircraft Lift and Drag

4.5.1 Lift Curve

With the lift curves of the wing and canard determined, the lift curves of the total aircraft for cruise and landing conditions can be constructed. From the resulting lift curves, the maximum lift coefficient and lift gradient are required as input for the preliminary sizing of the aircraft in section 4.1. Next to that, the curve for cruise conditions is used to determine the aerodynamic efficiency L/D of the aircraft. The parameters describing the lift curves are shown in table 4.18. Figure 4.20 displays the lift curves of the aircraft along with the lift curves of the wing and canard.

Table 4.18: Lift curve parameters describing the lift curves of the aircraft. α_{0L} and C_{L_α} are independent of the flight conditions for the low Mach numbers considered. $C_{L_{max}}$ and α_s are for landing conditions.

α_{0L} [°]	C_{L_α} [rad^{-1}]	$C_{L_{max}}$ [-]	α_s [°]
-2.2	5.28	1.30	13.3

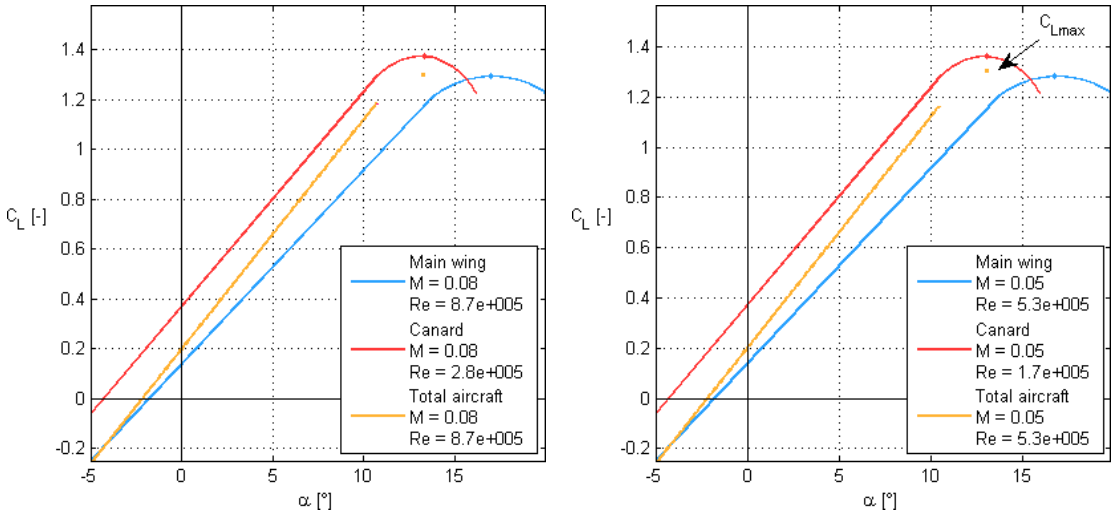

(a) Lift curves for cruise conditions.

(b) Lift curves for landing conditions.

Figure 4.20: Lift curves of the wing and canard and lift curves of the aircraft constructed using the indicated parameters from table 4.18.

The lift coefficients of the wing and canard are defined using different reference areas. Therefore, the lift coefficient of the total aircraft is calculated using equation 4.16.

$$C_{L_a} = C_{L_w} + C_{L_c}\frac{S_c}{S} \tag{4.16}$$

In this equation, C_{L_a} is the lift coefficient of the aircraft, C_{L_w} that of the wing and C_{L_c} that of the canard. S_c/S is the ratio of the canard and wing reference areas.

Because the shape of the lift curve of the aircraft in the stall region depends on the stall behaviour of the wing and the canard, this shape is complicated. As mentioned before, the shape of the wing and canard lift curves in the stall region is only an approximation. For these reasons, an estimation of the shape at the stall region for the aircraft would be very inaccurate. That is why the lift curve of the aircraft is only drawn up to the end of the linear part of the canard lift curve. Fortunately, the maximum lift coefficient and aerodynamic efficiency in cruise of the aircraft can be based on the linear part of the curve.

The maximum lift coefficient of the aircraft is reached when the canard stalls. Therefore the stall angle of attack of the aircraft equals the stall angle of attack of the canard. Since the lift curve of the aircraft is not linear at this angle of attack, the maximum lift coefficient is estimated to be at the point indicated in figure 4.20.

4.5.2 Drag Curve

In order to determine the aerodynamic efficiency of the aircraft in cruise and its zero lift drag coefficient C_{D_0}, the drag of all aircraft parts is calculated. The aerodynamic efficiency in cruise is a parameter indicating the quality of the aerodynamic design. The zero lift drag coefficient is required as input for the preliminary sizing of the aircraft in section 4.1. The drag in cruise of the parts comprising the total aircraft is first calculated, after which the total drag is calculated by summing the drag of the various parts. The values of C_{D_0} of the aircraft parts wing, fuselage, canard and vertical stabilisers as well as the total aircraft are shown in table 4.19. The C_D - α drag curves of the various parts are depicted in figure 4.21.

Table 4.19: Zero lift drag coefficients in cruise of the total aircraft and the parts wing, fuselage, canard and vertical stabilisers.

	Total	**Wing**	**Fuselage**	**Canard**	**Vertical stabilisers**
C_{D_0} [-]	0.038	0.011	0.023	0.015	0.010

Compared to small single engine aircraft with retractable landing gear, which have C_{D_0} values between 0.020 - 0.030 [50], the C_{D_0} of 0.038 is rather high. This is probably caused by the very low Reynolds numbers flown at during cruise. At low Reynolds numbers the skin friction drag is much higher [44]. Next to that, the contribution of the fuselage to the total drag is rather large. An increase in aerodynamic efficiency can be achieved by decreasing the fuselage diameter and length. However, the negative effects of reducing the tail arm of the canard should be taken into account.

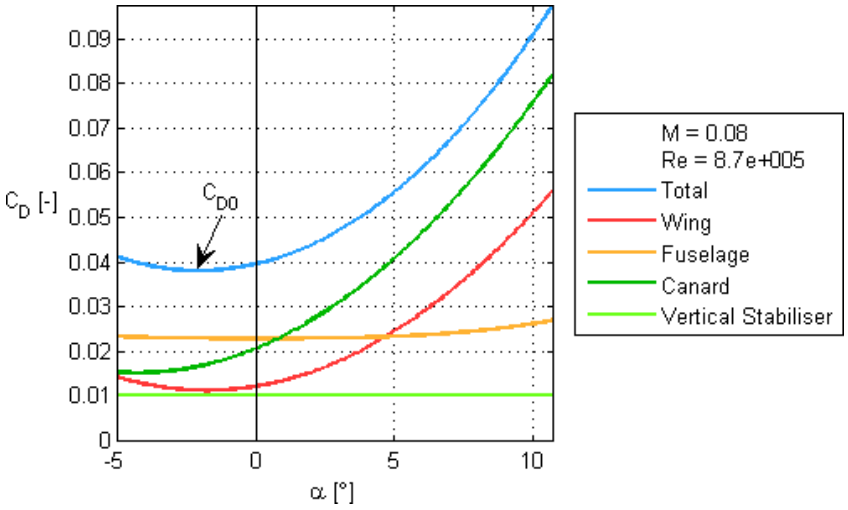

Figure 4.21: C_D - α drag curves in cruise of the total aircraft and the parts wing, fuselage, canard and vertical stabilisers.

The drag of the various aircraft parts is calculated using formulae which account for the Reynolds numbers, wing-fuselage interference and other factors [44]. The fuselage drag is based on its wetted surface area, slenderness, Reynolds number, wing-fuselage interference and angle of attack. The drag of the wing, canard and vertical stabilisers is determined using the aerofoil zero lift drag coefficients shown in table 4.20.

Table 4.20: Zero lift drag coefficients in cruise of the aerofoils of the wing, canard and vertical stabilisers.

	Wing (NACA 37014)	**Canard (NACA 4411)**	**Vertical stabilisers (NACA 0010)**
C_{d_0} [-]	0.00962	0.0141	0.00956

These values are corrected for three dimensional effects and wing-fuselage interference after which the lift induced drag is added as shown in equation 4.17. The assumption is made that in cruise flight no side slip occurs, so that the vertical stabilisers drag has no induced drag contribution.

$$C_D = C_{D_0} + \frac{{C_L}^2}{\pi A R_{eff} e} \tag{4.17}$$

In this equation, C_D is the drag coefficient of the wing or canard at the lift coefficient C_L. C_{D_0} is the corrected zero lift drag coefficient as shown in table 4.19 based on the aerofoil zero lift drag coefficients from table 4.20. AR_{eff} is the effective aspect ratio and e is the Oswald efficiency factor. The Oswald

efficiency factors for the wing and canard are assumed to be 0.8, because the aircraft has no landing gear [50]. Note that the zero lift drag coefficient of the canard is encountered at a lower angle of attack than that of the wing, because of the lower zero lift angle of attack of the canard.

The drag coefficients of the canard and vertical stabilisers are defined using different reference areas than the total, wing and fuselage drag coefficients. Therefore, the drag coefficient of the aircraft is calculated using equation 4.18.

$$C_{D_a} = C_{D_w} + C_{D_f} + C_{D_c}\frac{S_c}{S} + C_{D_v}\frac{S_v}{S} \tag{4.18}$$

In this equation, C_{D_a} is the drag coefficient of the aircraft, C_{D_w} that of the wing, C_{D_f} that of the fuselage, C_{D_c} that of the canard and C_{D_v} that of the two vertical stabilisers. S_c/S and S_v/S are the ratios of the canard and wing and vertical stabilisers and wing reference areas, respectively.

The aerodynamic efficiency in cruise can be determined using the aircraft lift curve of figure 4.20 and the total drag curve of figure 4.21. By constructing the C_L - C_D curve from this data, the aerodynamic efficiency can be obtained from the graph. The C_L - C_D curve is shown in figure 4.22. In this case the aerodynamic efficiency is defined as the ratio of the design lift coefficient and the drag coefficient corresponding to that lift coefficient in figure 4.22.

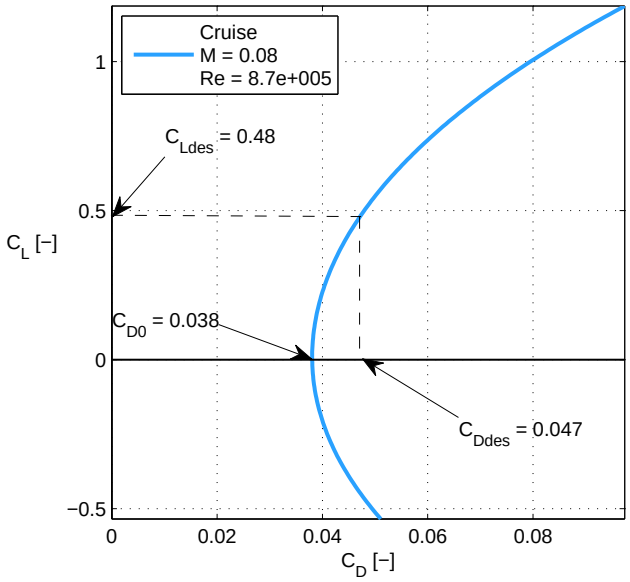

Figure 4.22: C_L - C_D curve of the aircraft in cruise.

The aerodynamic efficiency L/D is determined from the design lift coefficient $C_{L_{des}}$ and the corresponding drag coefficient $C_{D_{des}}$ to be 10.2. By taking into account other minor contributions to the drag, a more accurate value for the aerodynamic efficiency would be slightly lower. The aircraft may best be compared with homebuilt aircraft and single engine piston propeller aircraft for which the aerodynamic efficiencies generally have values between 8 and 10 [27]. Still the achieved aerodynamic efficiency is relatively high. One of the reasons for this high value is that the aircraft has no landing gear. Next to that, since the canard provides positive lift to the total lift of the aircraft, the lift coefficients flown at are lower than would be the case for an aircraft with a conventional tail contributing negative lift. Therefore, the induced drag of this canard design in cruise is lower than that for conventional aircraft.

4.6 Propulsion System

In the early design phase it has been decided that the aircraft shall use a push propeller with an electric motor as propulsion system. The push propeller shall provide thrust for the UAV in cruise flight as well as to perform manoeuvres. For the design of the propulsion system for this vehicle, both the propeller and the electric motor shall be designed.

4.6.1 Propeller

The first step to design the propeller is to consider the following fundamental equations 4.19 and 4.20

$$P_r = T \cdot V \tag{4.19}$$

$$\eta_{prop} = \frac{P_a}{P_{shaft_{prop}}} \tag{4.20}$$

The descriptions and values of the variable from these equations are listed in table 4.21

Table 4.21: Input parameters for sizing the propeller

Variables	Description	Value	From
T_{peak}	Peak thrust [N]	43.2	Equation 4.19
$T_{nominal}$	Nominal thrust [N]	36.04	Equation 4.19
V	Cruise velocity [m s^{-1}]	27.78	Requirements
$P_{r_{peak}}$	Peak power required [W]	1228	Aerodynamic Analysis
$P_{r_{nominal}}$	Nominal power required [W]	1001	Aerodynamic analysis

Equation 4.20 describes the efficiency of the propeller, which is the ratio between the shaft power ($P_{shaft_{prop}}$) and P_r. The higher the efficiency, the lower $P_{shaft_{prop}}$ needs to be, which is favourable for power consumption. To determine the efficiency 4.19 and 4.20 are combined and becomes equation 4.21

$$\eta_{prop} = \frac{T \cdot V}{P_{shaft_{prop}}} \tag{4.21}$$

From equation 4.20 it can be seen that the efficiency depends at least on T and V. Furthermore T depends on the diameter and the angular velocity of the propeller [51] and the aerofoil of the propeller [52]. For de dependence of the diameter, a new dimensionless parameter is defined in equation 4.22

$$J = \frac{V}{n\mathcal{D}} \tag{4.22}$$

Where J is called the advance ratio, n is the number of revolution per second and $\mathcal{D}$ is the diameter of the propeller in metre. Thus for a certain propeller with a certain aerofoil, $\mathcal{D}$ and n, η_{prop} differs with a different combination of T and V. Since the performance of different propeller aerofoils cannot be analysed using fundamental equations, experimental testing must be performed for analysis. However computer software can be used to simulate propeller characteristics under different conditions with combinations of different factors. For the propeller design of the aircraft, the software PropCalc 3.0 is used [53]. This software is used because it allows the user to select $\mathcal{D}$, n and an aerofoil for the propeller and PropCalc 3.0 give the efficiency as output for different η_{prop} for different combinations of T and V. Figure 4.23 shows a typical plot from PropCalc 3.0. This plot displays T, η_{prop} and $P_{shaft_{prop}}$ of a propeller with a given $\mathcal{D}$, n, number of blades and aerofoil.

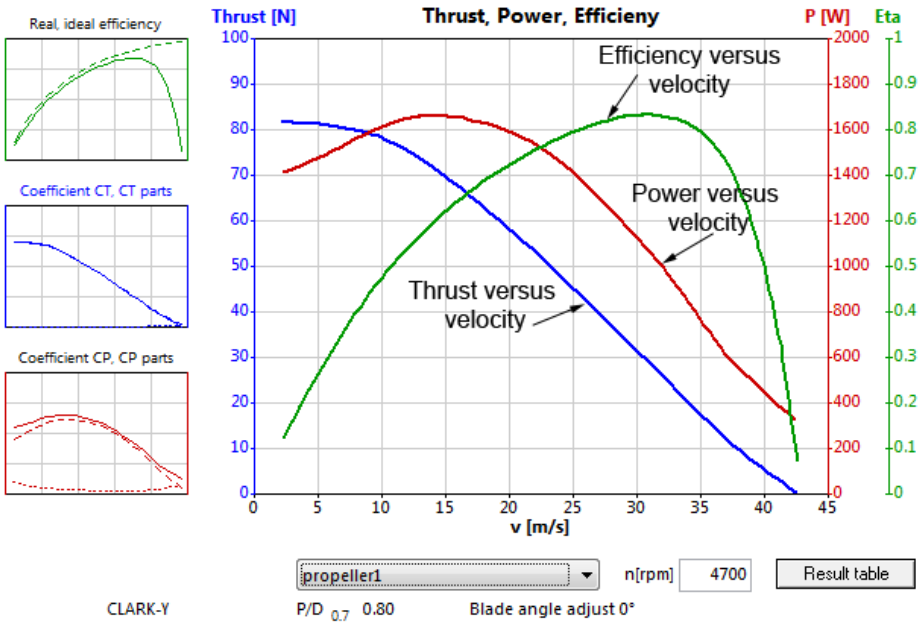

Figure 4.23: A typical plot from PropCalc 3.0 showing the thrust, shaft power and efficiency against the flight velocity with a given diameter, number of blades, aerofoil and rotation rate.

Note that n used in the tool is given in revolution per minute (rpm) while for calculation it is in revolution per second. The first step to size the propeller is to determine the diameter and the number of blades, the next step is to select an aerofoil. Hereafter the material is selected and finally the noise of the propeller is considered. From figure 4.23, it can be concluded that it is favourable to design the propeller in a way that the cruise velocity is in front of the optimum efficiency. This is because after the optimum efficiency, the efficiency drops rapidly and same goes for the thrust and shaft power.

Diameter and Number of Blades

To deliver enough thrust and power, the propeller can either have a high rotation rate and low diameter or vice versa. A rule of thumb is to maximise the diameter if possible, because generally a larger diameter requires a lower rotation rate, which is favourable for noise mitigation [52]. Also a larger diameter is generally more efficient as stated in Bolly's propeller [52]. However a larger diameter also increases the weight and induced drag. Typical diameters of propellers are in range of 7 to 22 inch or 18 to 60 cm [54].

Another possibility is to increase the number of blades, so that the propeller can deliver the required thrust running at a lower rotation rate and having a smaller diameter. This, however, is not recommended by [52], because the more blades a propeller contains, the more a blade will interfere with the air stream of the other blades, which will lower the efficiency. So a larger diameter is preferred over more blades again stated in Bolly's propeller [52].Barnard Microsystems [54] recommends to only use three or more blades when the diameter is limited to a certain value.

To determine a diameter for the propeller, reference UAVs will be considered to determine propeller diameters for maximum take off weights. These data are obtained from Jane's database [55]. The UAVs considered for the analysis are listed in table 4.22.

Table 4.22: Some reference UAVs from Jane's UAV database considered for estimating a value of a propeller diameter.

UAV Designation	**MTOW** [N]	**Prop Diameter** [m]
MK I	131	0.51
Luna X-200	392	0.56
Trogon	22	0.28
Nasnas Mk I	1226	0.75
Coyote	63	0.33
BQM-147A Exdrone	405	0.51

To estimate the propeller diameter in metres with the maximum take off weight in Newton from the aircraft, a trend line is drawn through the reference UAVs from table 4.22 which can be seen in figure 4.24

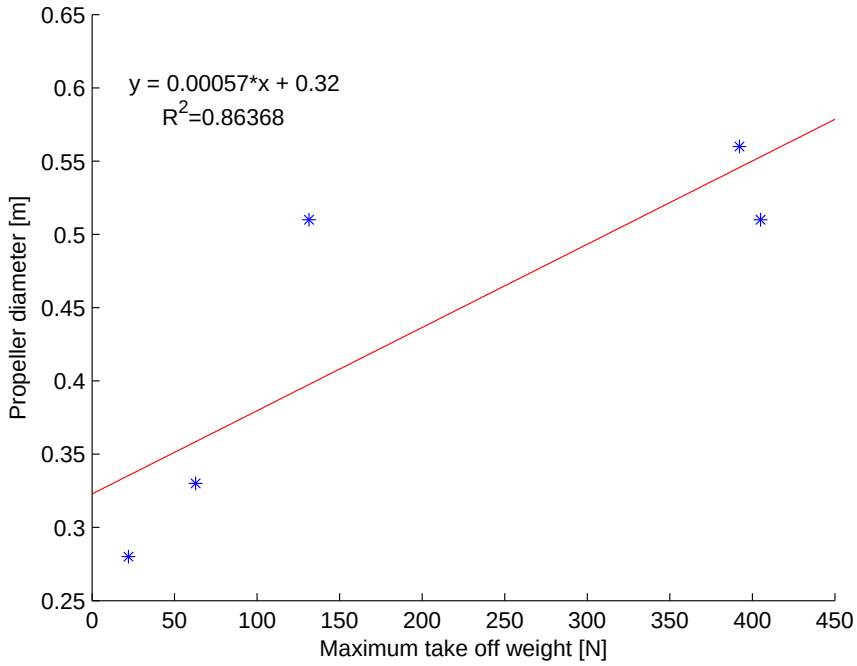

Figure 4.24: Trend line maximum take off weight versus propeller diameter.

The maximum take off weight of the aircraft is $35 \cdot 9.81 = 343$ N. From the trend line equation, this gives a diameter of 0.52 m and a corresponding available propeller diameter is 20 inches. However, from PropCalc 3.0 analysis, propellers of 20 inches have to run at a rotation rate close to 7000 rpm in order to achieve the desired thrust and velocity combination. When a propeller of 18 inches, exceeds 7000 rpm, the tip velocity exceeds Mach 1 and efficiency drops dramatically due to the appearance of a shock wave. Also for noise consideration, this is unwanted. This will be discussed in more details in the section about noise consideration. The best efficiency that can be achieved for 20 inches is 0.77.

From analysis with PropCalc it is much more efficient to use a propeller of 22 inches. A propeller of 22 inches can achieve the desired thrust and velocity combination at a much lower rotation rate and higher efficiency. The next section shows some data of 22 inches propellers with different aerofoils.

Thus $\mathcal{D}$ is 22 inches or 0.5588 m and the number of blades is two.

Aerofoil selection

For the propeller, it is desired to have the right velocity and thrust combination at a high efficiency and at a low rotation rate. The first thing to do is look at what rotation rate is required for a certain velocity and thrust combination. A visualisation of the method is shown in figure 4.25.

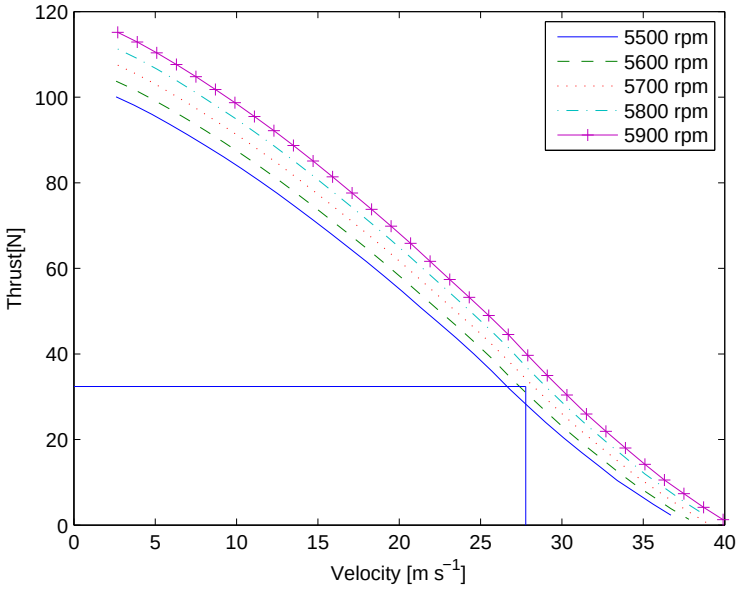

Figure 4.25: Speed against thrust of a propeller with different rotational rates.

However it is not possible to select a rotation rate that exactly matches the desired thrust, since the rotation rate of propeller is commonly rated at intervals of 100 rpm [52]. When the desired thrust is in between two different rotation rates, the rotation rate at the upper bound is selected to ensure that there is enough thrust.

The different aerofoils that are considered are the CLARK-Y, E193, E387 and E392. These aerofoils are considered because they are available in the database of PropCalc 3.0 and thus can be used to compare against each other. Performing the analysis as described above, the specifications of the different aerofoils are listed in table 4.23. The selection is made based on peak power required and nominal power required.

Table 4.23: Specifications of propellers from different aerofoils.

Aerofoil	**Nominal rotation rate** [rpm]	**Nominal efficiency** [-]	**Nominal thrust** [N]	**Peak rotation rate** [rpm]	**Peak efficiency** [-]	**Peak thrust** [N]
CLARK-Y	4700	0.82	37	4900	0.82	45.1
E193	5000	0.82	38	5100	0.81	43.42
E387	5000	0.83	36.2	5200	0.82	44.53
E392	4900	0.83	38.86	5000	0.81	46.24

It can be seen that the CLARK-Y has the lowest rotation rate required to obtain the required nominal and peak thrust. As for the efficiency, it can be seen that these are more or less the same for all the different aerofoils. Based on this information, the CLARK-Y is chosen as aerofoil. From equations 4.19 and 4.21 it is computed that $P_{shaft_{prop}}$ is 1.5 kW at peak condition and 1.2 kW at nominal condition.

Material Selection

In [54] it is explained that typical materials used to fabricate propellers are wood, fibreglass filled nylon, carbon fibre and pure nylon. Wooden propellers are the lightest, but it also the most fragile material [54]. Fibreglass filled nylon propellers are the heaviest, but also the most durable. Carbon fibres are very rigid, but also very expensive. It is commonly used for aircraft with large engines. The last material is pure nylon. Pure nylon propellers have the worst performance because they are flexible. This makes the propeller pitch change constantly and causes a lot of vibrations [54].

From the information about the different materials, wood propellers and pure nylon propellers are excluded immediately. The recovery method of the aircraft is to use a net, and this comes with quite some force acting on the UAV when the net puts a stop on the UAV. The nylon propeller gives poor flight performance and therefore shall not be used.

Since the recovery of the vehicle is quite rough, the most durable material should be considered, which is in this case fibreglass filled nylon. Hence fibreglass filled nylon is the material used for the propeller.

Noise Consideration

The noise produced by the UAV mostly comes from its propulsion system. The first consideration is that the upper tip Mach number should stay below 0.72 for acceptable noise as suggested by Roskam [56]. The equation to calculate the tip Mach number M_{tip} is seen in equation 4.23

$$M_{tip} = \frac{\sqrt{(\pi \mathcal{D} n)^2 + V^2}}{a} \tag{4.23}$$

Where a is the speed of sound, which is 340 m s^{-1} at the cruise altitude of the aircraft when considering ISA conditions. The rotation rate is 4900 rpm, which is equal to 81.67 rad s^{-1}. Filling in the remaining parameters of the propeller gives an M_{tip} of 0.43, which is well below 0.72.

However, the aircraft shall operate at low altitude and thus noise can be a problem the tip speed below the state limit. Further noise mitigation method is to implement rounded tips because rounded tips produces less noise compared to square tips [52]. Therefore the propeller shall consist rounded tips.

Other Consideration

Since the recovery method of the aircraft is to use a net, there is a chance that the propeller gets stuck in the net and get damaged. To avoid this problem, a folding propeller can be used to solve this problem. Another advantage of a folding propeller is when the motor jams, the induced drag from the propeller is lowered when folded, which enhances the gliding performance since the frontal area of the propeller is reduced. An example of a folding propeller is shown in figure 4.26 [57].

Figure 4.26: Example of a folding propeller

Weight and Cost Estimation

The weight of the propeller is estimated based on available propellers with the same size. Unfortunately there are no weight data available from propellers made of fibreglass filled with nylon with a diameter 22 inches. To estimate the weight, a propeller of 22 inches made of carbon fibre will be used as reference and the density of carbon fibre will be compared with the density of fibreglass filled nylon. [58] gives a weight of 0.14 kg. The density of carbon fibre and fibreglass filled nylon are 1577.75 kg·m^{-3} and 1290 kg·m^{-3} respectively [59] [60]. Taking the ratio of the fibreglass filled nylon density over the carbon fibre density and multiply this ratio with the weight of the carbon fibre propeller gives a weight of 0.11 kg.

A cost analysis has been performed for the propeller and it turns out that propellers of 22 inches made from fibreglass filled nylon is around EUR 30 [61] [62].

4.6.2 Electric Motor

Having the propeller designed, the electric motor that drives the propeller is sized based on the maximum shaft power of the propeller. The motor must be able to deliver the same shaft power and rotation rate as the propeller. Also it is desired to have a high motor efficiency so that the power consumption is minimised. The fundamental equations, which are obtained from [63] used to size the motor are seen from equation 4.24 till equation 4.27/

$$n_{motor} = (v - I\mathcal{R}) \tag{4.24}$$

$$P_{shaft_{motor}} = (I - I_0)(v - I\mathcal{R}) \tag{4.25}$$

$$P_{elec} = vI \tag{4.26}$$

$$\eta_{motor} = \frac{P_{shaft_{motor}}}{P_{elec}} \tag{4.27}$$

Here I_0 is the motor current at zero load in Ampere, K_v is called the motor speed constant, which is in rad·s^{-1}·Volt^{-1} for the equation. However for motor specifications, it is usually given in rpm· Volt^{-1}. At last $\mathcal{R}$ is the motor resistance. These values are called motor constants [63].

Reference Motors

To get a rough estimation of the motor constants, reference electric motors are used to obtain some initial values. One company that provides these data for their electric motors is E-flite [64]. These electric motors with their specifications are listed in table 4.24 [64].

Table 4.24: Reference motors from E-flite with its specifications

Motor	$\mathcal{R}$ [Ohm]	K_v [rpm · Volt^{-1}]	P_r [W]	I_0 [A]	**Mass** [kg]	**Cost** [EUR]
Power 10	0.043	1100	375	2.1	0.122	45
Power 15	0.03	950	575	2	0.152	49
Power 25	0.03	870	600	2.4	0.19	53
Power 32	0.02	770	800	2.4	0.2	57
Power 46	0.04	670	925	3.9	0.29	68
Power 52	0.016	590	1650	2.3	0.346	83
Power 60	0.06	400	1700	2.7	0.38	83
Power 90	0.02	325	1800	2	0.45	98
Power 110	0.03	295	2000	1.2	0.49	105
Power 160	0.03	245	2700	1.45	0.65	113

Note that in table 4.24 P_r is the recommended power required specified by the company. As it can be seen, $\mathcal{R}$ and I_0 are not correlated with P_r while K_v is. So the initial values for $\mathcal{R}$ and I_0 will be the average of all the motors and Kv will be estimated using a trend line similar to the propeller

diameter estimation. The linear equation for K_v against P_r is $K_v = -0.3721 \cdot P_r + 1109.8$. The initial values for I_0, $\mathcal{R}$ and K_v are 2.25 A, 0.032 Ohm and 9 rad·s^{-1}·Volt^{-1} respectively. With these values I, v, $P_{shaft_{motor}}$, P_{elec} and η_{motor} can be calculated. The motors from table 4.24 will only be used as reference and the idea is not to pick one of these.

Calculate the Motor Specifications

To calculate the motor specifications, the fundamental equations of the motors must be slightly rewritten. Equation 4.24 needs to be written into the function of the current so that $P_{shaft_{motor}}$ and η_{motor} only have the voltage as unknown.

$$I = \left(v - \frac{n}{K_v}\right)\frac{1}{\mathcal{R}} \tag{4.28}$$

Equations 4.25 and 4.27 then becomes equation 4.29 and equation 4.30 respectively.

$$P_{shaft_{motor}} = \left[\left(v - \frac{n}{K_v}\right)\frac{1}{\mathcal{R}} - I_0\right]\frac{1}{K_v} \tag{4.29}$$

$$\eta_{motor} = \left[1 - \frac{I_0\mathcal{R}}{v - n/K_v}\right]\frac{n}{vK_v} \tag{4.30}$$

In order to deliver the required shaft power to the propeller, $P_{shaft_{prop}} = P_{shaft_{motor}}$ and $n_{motor} = n_{prop}$. Rewriting equation 4.29 into a function for the voltage as seen in equation 4.31

$$v = \left(P_{shaft_{motor}}\frac{K_v}{n_{motor}} + I_0\right) + \frac{n}{K_v} \tag{4.31}$$

makes it possible to calculate the voltage for the required $P_{shaft_{motor}}$ and n_{motor}. Using equation 4.28 the corresponding current can be computed and eventually equation 4.26 can used to calculate P_{elec}. The values for v, I, η_{motor} using the initial values for the motor constants are 14.51 Volt, 171.02 A and 0.62 respectively.

Optimise the Motor Constants

Using the initial values of the motor constant gives a rather poor η_{motor}. To get a better η_{motor}, different motor constants should be considered. In table 4.24 it can be seen that both $\mathcal{R}$ and I_0 are rather the same for different motors. So to optimise η_{motor}, different values for K_v shall be considered because this value is the easiest to vary. Another requirement is that the voltage of the motor does not exceed 28 Volt, which is restricted by the electric systems.

A plot of η_{motor} versus K_v at peak condition is shown in figure 4.27.

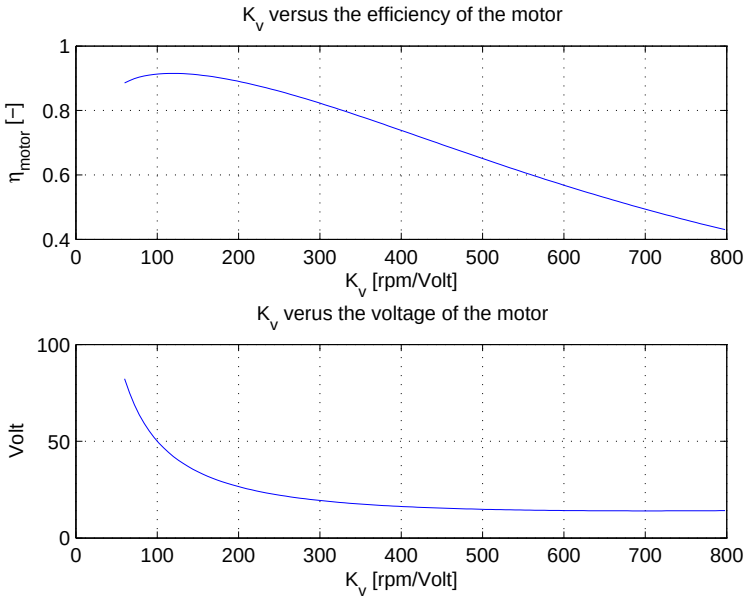

Figure 4.27: The motor efficiency and voltage versus different speed constants of the motor

In figure 4.27 it can be seen that there is a K_v value containing the optimum efficiency and after the optimum it decreases almost linearly. It can also be seen that at a low K_v, the required voltage exceeds the 28 Volt limit when K_v is lower than 200 rpm·Volt^{-1}.

Although it would be wise to optimise the motor efficiency for the nominal power required, the optimisation will be performed for the peak power required. This is to make sure that at peak condition, the voltage stays below 28 Volt. At v is 28 Volt, the values K_v, I and P_{elec} are calculated as 3.2 rpm·Volt^{-1}, 62.1 A and 1708.1 W respectively. For nominal condition, K_v will remain the same to make sure that the voltage stays below 28 Volt and I and P_{elec} are calculated as 53.45 A and 1400 W respectively and η_{motor} is 0.9.

Weight and Cost Estimation

To estimate the cost of the electric motor, the data from table 4.24 will be considered. The same method will be performed as estimating the initial motor constants. Drawing a trend line for the mass and cost against the power required gives the linear equation $mass = 0.0002 \cdot P_r + 0.0403$ with $R^2 = 0.9695$ and $cost = 0.0315 \cdot P_r + 34.025$ with $R^2 = 0.9591$. The mass is in kilograms and the cost is in Euro. Note that the price given in table 4.24 are given in US Dollars on the website. A conversion factor of 0.75 is used to convert it in Euro. Filling P_r in the equations gives a cost of EUR 82 and a mass of 0.35 kg.

4.6.3 Sensitivity Analysis

Sizing of the propeller was mainly performed using fundamental equations like equation 4.20 and software simulation. The software PropCalc 3.0 has limitations. Although the accuracy of the software is not given in the manual, experimental data has been compared to data obtained from PropCalc 3.0 [65]. In the experiment shown in [65] the propeller "Mini Ava" running at 4454 rpm, flying at a velocity of 10.2 m/s, PropCalc 3.0 provides a shaft power of 188 W and an efficiency of 0.65 as output. However from experiments a shaft power of 201 W and an efficiency of 0.66 is obtained. From other test performed it can also be seen that in some cases the efficiency is overestimated [65]. Thus for the detail design it is wise to perform experimental test and compare it with the results obtained from PropCalc 3.0.

As for the motor, the motor speed constants, cost and weight estimations are obtained from linear interpolation, and $\mathcal{R}$ and I_0 are the average values of the different reference motors. Since the R^2 values

for the linear equations of the trend lines are very close to 1, it can be concluded that there is a strong correlation of the values in table 4.24 for the linear interpolated values. However the reference motors are based on motors of the same manufactures. The reason for that is because this company is one of the few companies that provides detailed specifications of their motors. If motors from other companies were considered, the linear trend line might look different and the R^2 value will probably be much lower. Therefore the cost and weight estimations should be considered as rough estimations and during the detail design, the actual values can deviate from the calculations.

4.7 Electric System

The propulsion, communication, obstacle detection and control subsystems can generate large electrical loads. The primary power is supplied from the PV cells. The batteries provide energy storage and also act as a backup power source. A Power Management and Distribution (PMD) system links the energy generation source to the energy storage elements and to the aircraft electric loads. A schematic representation of overall aircraft power system is shown in figure 4.28.

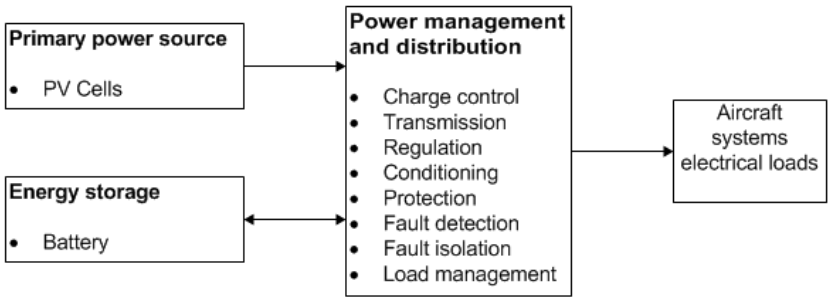

Figure 4.28: The power system of the UAV which gives an overview of the tasks of the power management and distribution.

The main functions of the PMD system are listed in figure 4.28. It is paramount to have a PMD system because different electric devices have different voltage and/or current requirements. Supplying devices with the wrong power requirements may render the device inoperable [66]. The PMD system controls the available power depending on whether electric devices are active or not. The output power from the PV cells and the battery vary over their life or operating conditions. A PMD system accounts for this variation to avoid damages and conditions power to a given load.

4.7.1 Power Management and Distribution System

The PMD consists of a Power Processing Unit (PPU), a Battery Management System (BMS), cabling and switches. The PPU is a module that controls the electric power supply for the other subsystems of the UAV [67]. It handles the direct current (DC) from the PV cells and adjusts the power output to the varying demands of the several subsystems. A schematic representation of the PPU is outlined in figure 4.29.

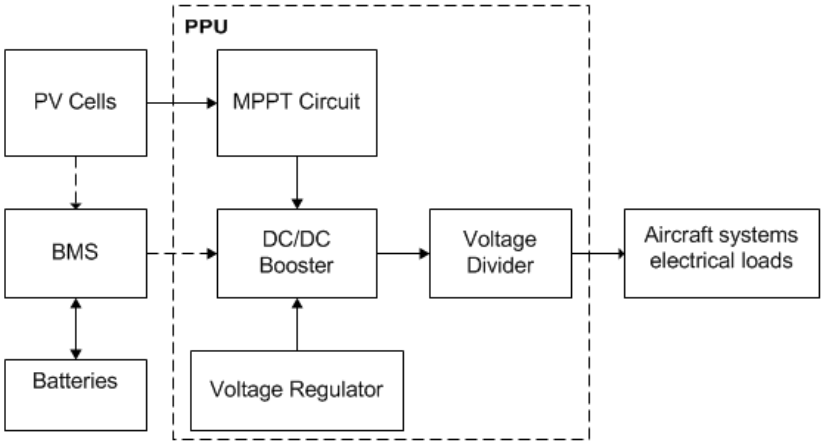

Figure 4.29: Power management and distribution system

Power produced by the PV cells is directly supplied to the electrical loads for level flight. This power goes to the MPPT (Maximum Point Power Tracking) electronic device. The MPPT optimise maximum power that could be obtained from the solar cells [68]. The power consumers do not operate at the same voltage range, consequently a DC/DC booster is used to convert voltage from one level to another. A voltage regulator automatically maintains constant voltage. The power is divided to the different loads using an adjustable potentiometer as a voltage divider.

Any solar cell power exceeding the power required by the electrical loads is used to recharge the battery. Prior to flight fully charged batteries are installed. Batteries are used in an event of temporary power collection failure or in situations that require more power than available from PV cells. If the power required exceeds current power available the nonessential loads are shut off and the flight critical systems remain operational. In case of total failure of energy collection, the batteries provide power for to flight- critical procedures. This enables the UAV to land safely for maintenance procedures.

The BMS consists of a battery controller, charge or discharge regulator and power control unit [66]. A battery controller initiates charging and stops discharging when the critical level has been reached. The regulator adjusts the voltage to the optimum point for battery charging or discharging. The power control unit measures the battery voltage and senses the level of battery charging. The BMS communicates to the ground station the amount of available power at each given time.

The power system wiring distributes the power from the source to the loads. The wiring is shielded to prevent electromagnetic induction effects from other electronics [56]. Connectors are used to harness wiring between power interfaces. Flight-critical and non-flight-critical power busses are separated to improve reliability. A failure on the non-flight- critical does not affect the other power buss. Switches are used to turn the electrical loads on and off.

4.7.2 Electrical Block Diagram

The average and peak power required by different subsystems is shown in table 4.25.

Table 4.25: UAV Subsystems Power Consumption

Subsystem	**Average power required [W]**	**Peak power required [W]**
Propulsion	1000	1700
Communication	20	30
Obstacle detection	30	50
Control	80	130

A graphical overview of the power distribution of the UAV is shown in a form of an electrical block diagram, illustrated in figure 4.30. The power budgeted for each subsystem is the peak power required.

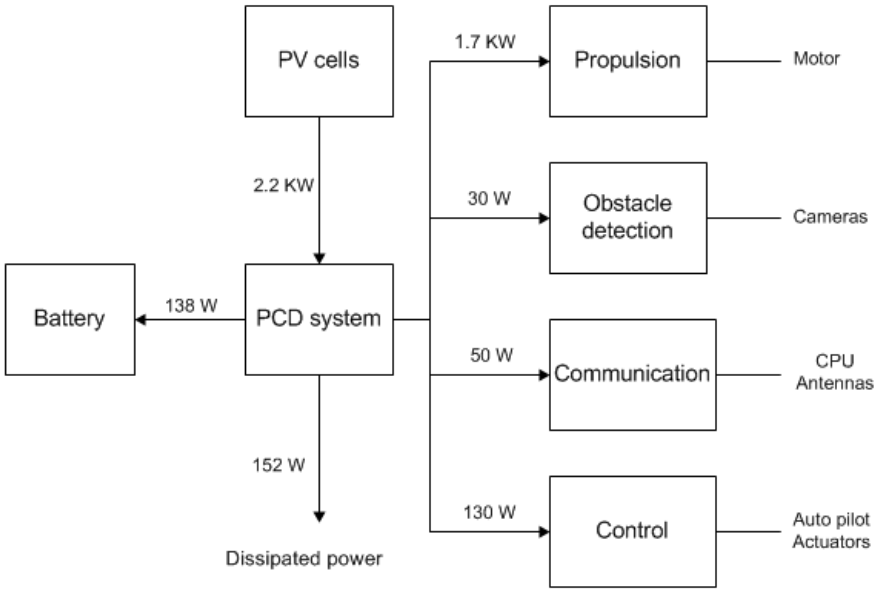

Figure 4.30: Electrical Block Diagram of the UAV

4.7.3 Battery Sizing

Lithium-ion battery is used for power storage and its properties are given in table 4.25 [66][69][70][56][71]. The properties are used to size the most appropriate battery for the UAV. The sizing process takes into battery degradation and battery cycle management discussed in the following section.

Table 4.26: Lithium-ion battery properties

Specific energy [Wh/kg]	**Energy density** [Wh/l]	**Nomial cell voltage** [V]	**Nomial cell capacity** [Ah]	**Cycles** [-]	**Charging efficiency** [-]
265	250	3.6	3.7	>1500	85%

The power available from the solar cells P_{PV} is 2200 W. The total power required P_{req} given by equation 4.32 is the sum of electrical loads for each subsystem and the system power loss (P_{loss}). For battery sizing peak required power is used. Power loss is estimated to be 8 % of P_{req} [72] and this compensates for the energy lost in the form of heat due to the impedance of the electronic circuits and wiring losses.

$$P_{req} = P_{subsytems} + P_{loss} \tag{4.32}$$

The battery is sized by using the critical power provision scenario. This is a situation where by the battery provides power required continuously for 30 minutes. This time is sufficient for the UAV to safely land in case of total power transfer failure and for European Aviation Safety Authority certification regulations [73]. Battery capacity is 988 Wh obtained by equation 4.33, where $Endu$ is endurance, the time the battery have to provide power .

$$E_{totreq} = Endu \cdot P_{req} \tag{4.33}$$

The mass of the battery is obtained by equation 4.34, where E_{spec} is the battery specific energy.

$$m_{batt} = \frac{Endu \cdot P_{req}}{E_{spec}} \tag{4.34}$$

Battery volume is obtained by equation 4.35 where E_{dens} is the energy density.

$$Vol_{batt} = \frac{Endu \cdot P_{req}}{E_{dens}} \tag{4.35}$$

Actual battery volume is 1.2-2.5 times larger than the total cell volume and actual mass is about 0.1-0.4 kg heavier per litre of actual battery volume [66]. This is because of the battery case holding the cells, electric circuitry and instrumentation. The actual battery weight and volume is 3.92 kg and 0.004 cubic metres respectively.

The amount of energy contained in each cell E_{cell} is given by equation 4.36 , where C_{cell} is the cell capacity and V_{cell} is the cell voltage.

$$E_{cell} = C_{cell} \cdot V_{cell} \tag{4.36}$$

Energy in each cell is 13.3 Wh hence to obtain the required power 75 battery cells are needed. Connection of cells is done in done in parallel and the battery voltage is given by equation 4.37, where n is the number of cells. UAV electrical loads mainly operate at 11-28 V dc [56]. To produce 28 Volts, 8 cells are needed. Resultantly the battery system is composed of 10 packs of 8 cells each which are able deliver the required power.

$$V_{pack} = n \cdot V_{cell} \tag{4.37}$$

Excess power P_{excess} is given by equation 4.38.

$$P_{excess} = P_{PV} - P_{subsytems} - P_{losses} \tag{4.38}$$

When excess power is positive, the excess power is used to charge the battery and the stored energy E_{stor} is

$$E_{stor} = \int P_{excess}(t) \cdot \eta_{charge} \cdot dt \tag{4.39}$$

where η_{charge} is the efficiency of the stored energy conversion process. This integral is discretised into multiple time steps when the excess power is positive. The time to continually charge the battery to full capacity is 5.11 hours and is calculated by equation 4.40.

$$t = \frac{E_{stor}}{P_{excess}(t) \cdot \eta_{charge}} \tag{4.40}$$

The amount of energy provided by the battery when the primary energy source cannot deliver power is

$$E_{out} = P_{req} \cdot \eta_{discharge} \cdot t \tag{4.41}$$

where η_{charge} is the discharging efficiency of the battery and t is the duration of discharge.

4.7.4 Battery cycle management

Battery cycle life is defined as the number of complete charge - discharge cycles a battery can perform before its nominal capacity falls below 80 % of its initial rated capacity[66]. Some deterioration of the battery occurs on each charge/discharge cycle, hence when designing a battery management system cycles are considered. The battery cycle for the lithium ion battery is greater than 1500. To prolong the battery life, the cycles are minimised as much as possible. When the UAV is following the flight path, there are instances when the laser system cannot transfer power. It is during this time when the battery powers the UAV. The UAV is not charged after every power loss phase, instead charging starts when the battery has reached a certain capacity, hence minimising battery cycles. The capacity reached is the Depth of Discharge (DOD).

When the UAV is following a flight path it takes 25 minutes to complete one lap. During each lap the total time for which solar power is not available is approximately 3 minutes as discussed in section 2.3.2. The power required for each lap is calculated by equation 4.33. Using the average power required, the capacity required to complete 6 laps is 360 Wh and charging starts after every six laps. The DOD is 64 % which is more than the allowable lithium ion battery DOD [74] and the reserve energy of 628 Wh can provide average power for more than 30 minutes. A day has approximately 60 laps and consequently the number of battery cycles is 10 per day. Considering that lithium ion battery has a minimum of 1500 cycles, the minimum battery life is 150 days. During its operational time the UAV will have a new battery after every 5 months.

4.7.5 Cost Estimation

The estimated cost of the electric subsytem is obatined by summing the sub components of the system. The lithium ion battery consumer price is 5 Wh/US$ [71] and resultanly the battery cost is EUR 160. The initial cost of the system is estiamated to be EUR 1290 and the cost break down is presented in table 4.27 [75][76]. The battery should be changed every 5 months giving an operation cost of EUR 320 every 10 months.

Table 4.27: Electric System Initial Cost

Item	**Cost** [EUR]
Battery	160
PMD system	60
Wiring and connetors	1 070
Total Cost	1 290

4.8 Verification and Validation

For the design of the aircraft numerical computations are done. The codes of these computations are verified in order to guarantee that a correct analysis is performed. First the code is double checked to make sure that there are no mistakes. Secondly either a simple hand calculation is done, which is then compared with the results of the code using the same inputs or the results are compared with references.

Validation, which is checking whether the results are comparable with reality, is not performed. The reason for this is that the design is not at the required stage to do this yet. One way of doing this is by building a scale model of the design and testing it in a wind tunnel. The results of the wind tunnel experiment can then be compared with the calculated results. If there is a large deviation then the assumptions taken during the design process have to be reconsidered.

CHAPTER 5

CONTROL AND OPERATIONS

In the previous chapters the design step for the aircraft and laser base station is explained. Having the laser base station and the aircraft designed, it is required that these systems interact with each other in order to perform its mission. This chapter describes the procedure of how the aircraft is controlled and communicate with its operators. During its first use the aircraft needs to be launched and for maintenance purposes the aircraft needs to be recovered over time. Section 5.1 explains the control procedure of the aircraft and section 5.2 describes how the aircraft detect and avoid possible obstacles that enters its flight path. Section 5.3 explain how communication is established within the network and section 5.4 describes the launch and recovery procedure. Finally section 5.5 explains the general operation procedure of the UAV and the network where it shall operate.

5.1 Aircraft Control

The aircraft is controlled by deflecting the control surfaces. Deflecting the ailerons results in a roll moment, deflecting the rudder results in a yaw moment and deflecting the elevators will result in a pitch moment. In order to deflect the control surfaces, servo actuators need to be installed in the aircraft to deliver a torque to deflect the actuators. Furthermore the aircraft shall be unmanned and thus it shall receive its flight path commands from ground station. To execute the command, an autopilot is installed to process the received commands and control the control surface deflection. In this the selection of the servo actuators and an autopilot are described. After the selection a weight and cost estimation will be performed and eventually a sensitivity analysis is performed to explain what the effect is in case of changes in the design.

5.1.1 Servo Actuators

Having the control surfaces sized, a mechanism is required to give these the required deflection. To give the control surfaces the desired deflection, a torque has to be applied. For UAVs the torque is commonly delivered using servo actuators. In order to select the actuators that delivers the right torque, the required torques to deliver the deflection shall be computed.

Fundamental Equations

The torque that needs to be delivered depends on the dimensions, flight velocity, angle of attack and the maximum deflection. The fundamental equation for the hinge moment is [77]

$$H = C_h \frac{1}{2} \rho V^2 S c \tag{5.1}$$

where H is the hinge moment and C_h is the hinge moment coefficient. C_h depends on the angle of attack and the deflection and the equation for this variable is

$$C_h = C_{h_\alpha} \alpha + C_{h_\delta} \delta \tag{5.2}$$

where $C_{h_\alpha} \alpha$ is the hinge moment derivative with respect to the angle of attack and $C_{h_\delta} \delta$ is the hinge moment derivative with respect to the deflection. The variable used for the different control surfaces are listed in table 5.1.

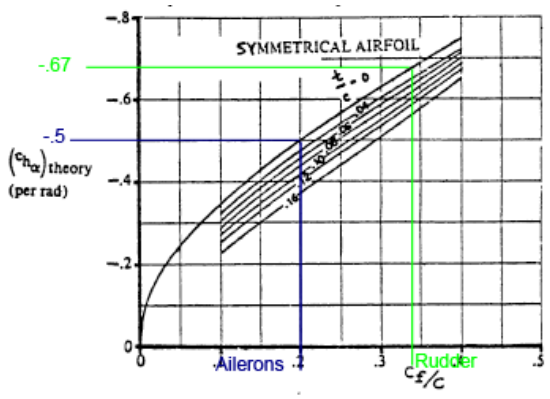

Figure 5.1: Graph used to determine the value of C_{h_α}

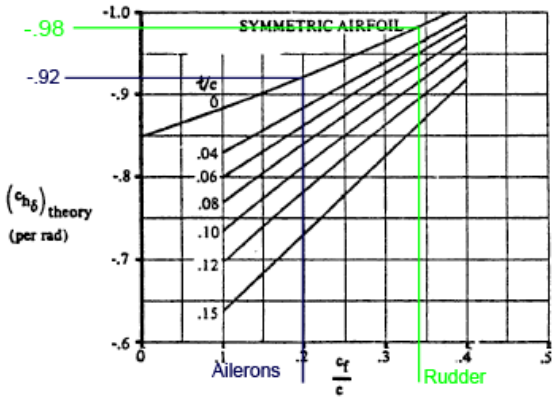

Figure 5.2: Graph used to determine the value of C_{h_δ}

Table 5.1: Symbols of the hinge moments description.

Symbol	Description
H_a	Hinge moment ailerons [Nm]
H_r	Hinge moment rudder [Nm]
H_e	Hinge moment elevator [Nm]
$C_{h_{\alpha_a}}$	Hinge moment derivative with respect to angle of attack ailerons $[rad^{-1}]$
$C_{h_{\alpha_r}}$	Hinge moment derivative with respect to angle of attack rudder $[rad^{-1}]]$
$C_{h_{\alpha_e}}$	Hinge moment derivative with respect to angle of attack elevators $[rad^{-1}]$
$C_{h_{\delta_a}}$	Hinge moment derivative with respect to aileron deflection $[rad^{-1}]$
$C_{h_{\delta_r}}$	Hinge moment derivative with respect to rudder deflection $[rad^{-1}]$
$C_{h_{\alpha_e}}$	Hinge moment derivative with respect to elevators deflection $[rad^{-1}]$

The method used to determine the hinge moments derivatives is obtained from [77], which shows that the determination shall be performed graphically. A visualisation of the method is shown in figure 5.1 and figure 5.2 [77].

C_f/C is the ratio of the chord of the control surface over the chord of the attachment surface. For example for the aileron the ratio is C_a/C_w. These ratios are determined in sections 4.1 and 4.3. It is determined that $C_{h_{\alpha_a}}$ and $C_{h_{\alpha_r}}$ are -0.5 and -0.67 respectively and $C_{h_{\delta_a}}$ and $C_{h_{\delta_r}}$ are -0.92 and -0.98 respectively.

The hinge moment derivatives from figure 5.1 and figure 5.2 are the theoretical values and some assumptions are made when using these values. First it is assumed that the aerofoils are symmetric. The second assumption is that the gap between the control surface and the surface at which it is attach is unsealed. Furthermore the effect of Mach number is neglected. The error due to the first assumption is negligible for the rudder because for lateral stability the rudder needs a symmetric aerofoil. For the ailerons hinge moment derivatives can have errors up to 2 rad^{-1} as it can be seen in figure 5.1. This is when the thickness ratio (t/c) is 0.15. So if the aerofoil is not symmetric, one shall revise this assumption. Neglecting the effect of Mach number is a valid assumption because $M < 0.1$. Equation 5.3 shows the effect of Mach number

$$(C_{h_\alpha})_M = \frac{C_{h_\alpha}}{\sqrt{1-M^2}} \tag{5.3}$$

which is obtained from [77] and from this equation it can be safely concluded that the effect of Mach number can be neglected at low Mach number. Since the elevators are not integrated into a structure and are attached on the fuselage instead, the methods provided by [77] cannot be used. However [78] provided typical values for $C_{h_{\alpha_e}}$ and $C_{h_{\delta_e}}$ which are -0.59 and -0.9 respectively.

To calculate the hinge moment derivatives, the maximum angle of attacks at which the control surfaces operates and their maximum deflections are used. The maximum angle of attack of the ailerons and rudder are equal to those of the wing rudder respectively. Same goes for the elevator. Those values were obtained in sections 4.1 and 4.4. Previously it was also assumed that the downwash angle of the elevators on the wing is negligible and thus $\alpha_a = \alpha_r$.

These values are summarised in table 5.2

Table 5.2: Maximum angle of attacks of the control surfaces.

$\alpha_{controlsurface}$	**Value** [°]	**Obtained from**
α_a	16	4.1
α_e	16	4.4
α_r	10	[79]

Having the hinge moment derivatives for each control surface obtained, equation 5.2 is used to derive the hinge moment coefficient. The maximum angle of attacks and deflections are found in 4.1 and with these values the maximum hinge moments are derived from equation 5.1. The dimensions of the control surfaces are obtained in 4.1, 4.3 and 4.4.

Thus H_a, H_r and H_e are 0.37 Nm, 0.4 Nm and 5.4 Nm respectively. Based on these values, the proper servo actuators are selected. Actuators considered for the aircraft shall be delivered from the company Pegasus Actuators GmbH [80]. This company delivers high quality servo actuators for UAVs and different actuators are available depends on the torque required. For the computed hinge moments, the product Pegasus PA-R-135-4 with a maximum torque of 0.6 Nm [81] shall be used for the ailerons and the rudder and the actuator Pegasus PA-R-250-9 with a maximum torque of 7 Nm [82] shall be used for the elevators. For the calculation of the hinge moments of the ailerons and rudders, one aileron and one rudder are considered. And for the elevators, both elevators are considered. This is because the elevators can be driven by using one actuator in the centre while for the ailerons and rudders, two separated rudders are required.

5.1.2 Autopilot

In order to control the aircraft, the ground station has to know the attitude and position of the aircraft. It is also required that the aircraft receive commands from the ground station and follow a pre programmed flight path and avoid obstacles autonomously. To achieve all these requirements, an autopilot system needs to be installed in the aircraft. The autopilot shall determine the position and attitude of the aircraft, process the information obtained from the obstacle detection systems, which are described in section 5.2 and control the actuators and communication systems.

Selection

Different autopilot systems are considered for the aircraft. The autopilot system with its specifications is obtained from [83]. The autopilots considered are summarised in table 5.3.

Table 5.3: Different UAV autopilot systems with its specifications.

Autopilot	Kestrel	MP 2028	Piccolo LT	Unav 3500
Mass [kg]	0.0167	0.028	0.045	0.042.5
Power consumption [W]	2.5	0.91	4	0.6
Price [EUR]	3750	4125	-	-
Waypoint navigation [Yes/No]	Yes	Yes	Yes	Yes
Altitude hold [Yes/No]	Yes	Yes	Yes	Yes
Multi-UAV support [Yes/No]	Yes	No	Yes	No

It is required that the autopilot has a waypoint navigation and multi UAV support. The only autopilot systems that contain these features are the Kerstrel and the Picollo LT. However table 5.3 shows that the autopilot Kestrel is cheaper, consumes less power and is lighter. Based on this information the autopilot Kestrel will be selected.

A more detailed specification of this autopilot can be found in [9]. It is stated that the autopilot utilises GPS and a 3-axis rate gyroscope to determine its position and attitude respectively. Furthermore it provides features to support payloads.

Power Consumption and Data Transfer Rate

The autopilot shall be powered by the electric systems and operates at a voltage of 5 Volt and a current of 0.5 A [9]. Thus the power consumption of the autopilot will be 2.5 W.

A requirement with respect to aircraft control is that the aircraft shall receive its flightpath from the ground station. The ground station shall in return receive the attitude and position of the UAV. This can only be achieved if the aircraft communicates with the ground station and thus an uplink and a downlink for the aircraft is required. A typical status message from a UAV is 3569 bytes including header, inertial measurment unit, flight control unit, power, warnings, communication, payload, GPS and obstacle and avoidance data [84] and during mission 1 message every 10 seconds is typically required [84]. During take-off and landing this will be one message per second is required [84] and this gives a required downlink data transfer rate of 3569 bytes/s, which is 28552 bits/s. The uplink is used to upload and change the flight plan of the UAV [84]. A typical flight plan is 8000 bits in size containing the begin and end waypoints in GPS coordinates and the setup of the mission and for a fully autonomous aircraft an update rate of 1 time per second is typical [84]. Thus for the uplink a required data transfer rate is 8000 bits/s.

Safety and Redundancy

In the description [9] it is mentioned that the autopilot contains multiple user configurable failsafes features, including loss of communications, loss of GPS lock, flight termination and terrain elevation data. These features prevent the UAV from being a threat to the environment in case of critical functions of the UAV fails.

However, the failsafe features are not able to recover the aircraft once the autopilot fails. Once the autopilot fails, the aircraft is not able to receive commands from ground station and in the worst case this can lead to a loss in a UAV. To minimise the chance that such an event occurs, a backup autopilot is installed.

Since the elevator is driven by one servo actuator, pitch control can be a problem when that actuator fails. In case if this happens, the pitch shall be controlled by using thrust regulation which shall be preprogrammed in the autopilot. In case if the autopilot fails this task, a human operator shall take over control and make sure that the aircraft will not become a threat.

A visualisation of the autopilot and the whole aircraft control system is shown in figure 5.3 and figure 5.4 respectively.

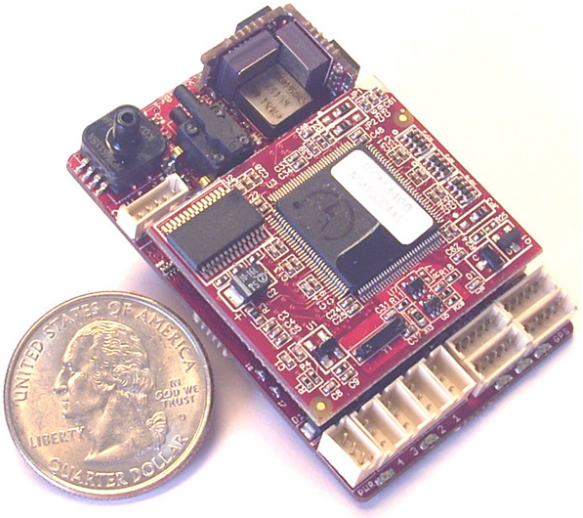

Figure 5.3: The flight control system of the aircraft.

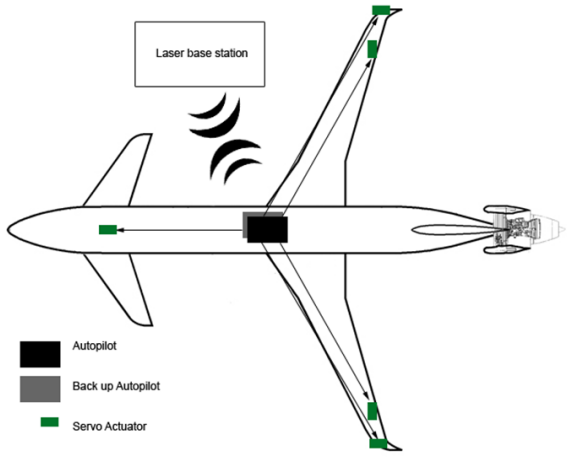

Figure 5.4: The flight control system of the aircraft.

5.1.3 Weight and Cost Estimation

A weight and cost estimation was performed for both the servo actuators and the autopilot.From an Email to the to the company, the price of several actuators are obtained [85]. The weight of the servo actuators are published on the website [80]. The cost and weight of the servos are listed in table 5.4.

Table 5.4: Price and weight list of the actuators

Actuator	**Weight** [kg]	**Cost** [EUR]
Pegasus Par-R-135-4	0.065	350
Pegasus Par-R-205-4	0.125	962
Pegasus Par-R-205-6	0.15	1,160

Unfortunately the price of the Pegasus Par-R-205-9 was not given and is estimated to be around EUR 1,260 based on the price difference between the Pegasus Par-R-205-4 and the Pegasus Par-R-205-6. The weight and cost of the autopilot can be found in table 5.3. With these information the total weight and cost for the flight control are estimated to be EUR 10,160 and 0.6284 kg respectively. The price includes the back up autopilot, which costs as much as the main autopilot.

5.1.4 Sensitivity Analysis

The selection of servo actuators are based on the geometry and the cruise speed of the aircraft. If these parameters change, then different servo actuators need to be considered, which has consequences for the weight and cost.

Changes in the design shall not affect the selection of the autopilot, because the autopilot is pre programmed based on the flight control characteristics and the on board payloads [9]. However if the requirements change then a different autopilot might need to be considered. For example if it is no longer required to support multiple UAVs or if real time piloting is considered, then an even less advanced autopilot can be considered than those in table 5.3.

5.2 Obstacle Detection

Nowadays many aircraft fly above the Hague. Birds are also fond of the Hague [86]. The chances for collisions are therefore relatively high. Although modern commercial aircraft can easily withstand a collision with a bird, the UAV will not be able to withstand the collision. A rough estimation was done on the impact strength and it is shown that a collision with a bird will have no impact on the structure of the UAV [21]. However obstacle detection is still needed due to the internal subsystems being less resistance to collisions. This suggests that obstacle avoidance procedures are required for avoidance of birds, buildings, aircraft and other obstacles. In the mid-term report [5] it is chosen that conventional and infrared cameras and radar systems are needed for obstacle avoidance. The information from the air traffic control will also be used to avoid obstacles. A radar and an infrared camera will be placed on the ground, while a conventional and infrared camera will be placed on board the UAV. The methods used for obstacle detection are explained in detail in this section.

5.2.1 Obstacle detection on board

Range and field of view

In order to size the cameras the maximum range, the smallest object at that range and the speed of that object have to be known. The maximum range the cameras have to sense is calculated with the turn radius and climb gradient of the UAV. The civil aviation authority published a recommendation which will require an UAV to avoid another aircraft by at least 500 ft, which is 152 m [87]. From the aircraft performances 4.1 it is calculated that the UAV needs a range of 1.6 km and 3 km to avoid an obstacle to the sides or by climbing respectively. This means that the climb is the critical factor for range calculations. However the distance needed for avoiding aircraft is not implemented in the calculations of the on board cameras. The on board cameras are meant for sensing obstacles not registered by the air traffic control such as birds. The avoidance distance of 152 m is used for the calculations of the radar specifications.

The range of the cameras is calculated by estimating the distance needed to avoid an obstacle, r_{climb} and the time needed for a pilot, t_{pilot}, to avoid an obstacle comfortably. A bird is used as a reference obstacle since this is the fastest and smallest possible obstacle that flies around frequently. The peregrine falcon is used as a reference bird since this is the fastest bird in the Hague with a relative large span. The cruise speed, V_{bird}, and span of the falcon are 24.58 m $\cdot$ s^{-1} and 1 m respectively [88]. A comfortable time for a pilot to avoid an obstacle is experimentally tested to be ten s [89]. The distance to safely avoid a bird is assumed to be ten m. Although the autopilot of the UAV will only needs 15 ms [90], the range is still calculated for the pilot to act without any rush during obstacle avoidance. Equation 5.4 shows the calculations for the range, r. As a safety factor the climb gradient is halved.

$$r = t_{pilot} \cdot V_{UAV} + t_{pilot} \cdot V_{bird} + r_{climb} = 753.5m \tag{5.4}$$

The minimum field of view needed to avoid the bird is calculated by analysing the situation of a bird flying perpendicular to the flight path of the UAV. Although the field of view will be less than it should actually be, the high consideration time of the pilot will compensate for this. The same range, decision time of 10 s and the climb gradient can be used again. This means with a range, r, of 753.5 m the total azimuth angle, ϕ, is 82°. The equation for the azimuth field of view can be found in equation 5.5 if the sensors are assumed to be at the nose of the UAV.

$$\phi = \arctan \frac{\frac{r}{V_{UAV}} \cdot V_{bird}}{r} = 82° \tag{5.5}$$

Although this field of view is required for a fast flying bird, this field of view will just be used as an indication. There are no other obstacles that fly this fast besides the birds. A research was done on the reaction of birds on smaller aircraft by the 'Proceedings of the National Academy of Science' [91] and three out of the thousand birds that frontally approached an smaller sized aircraft, without warning lights, seem not to take evasive manoeuvres. These birds can be detected and avoided. However birds

approaching the blind spot of the UAV, such as the back of the UAV, will avoid the UAV by using appropriately arranged lights on the sides and back of the UAV [91]. Birds will avoid the aircraft by being warned by the lights. These lights will be pulsed LED flash lights in the violet colour range. The colour violet gives the birds the impression that the UAV is a predator [92]. Launch and landing will only be done when no birds pass by instead of using conventional methods such as using noise or falcons to harass the bird population [93].

Wavelength and sensitivity

All objects emit and absorb a certain amount of energy at certain wavelengths [94]. In order to sense an obstacle the correct wavelength has to be chosen which the obstacle emits the most. This can be done by using Plank's law and assuming the earth, the camera and the obstacle are black bodies [94]. The spectral radiation curve is then plotted for a bird at a body temperature of 20° above room temperature [95] with an emissivity of 0.95 [96] in figure 5.5(a).

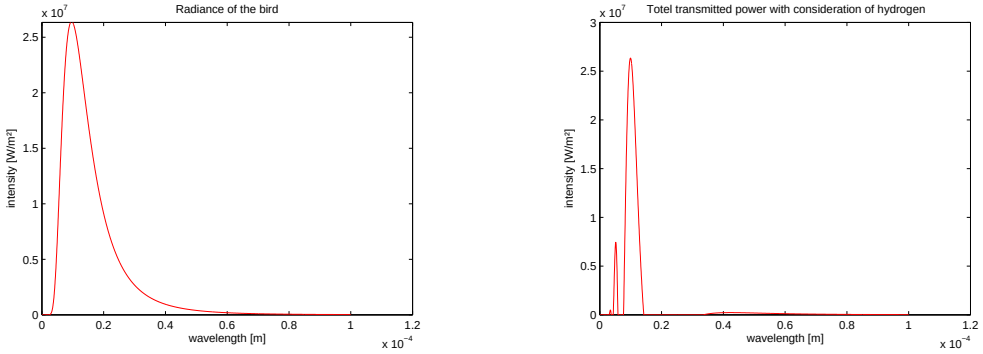

(a) At vacuum

(b) With consideration of hydrogen

Figure 5.5: Spectral radiance of a bird

From the plot it can easily be seen that the peak of the emittance of the bird is at a wavelength of 10 µm, which is in the infrared spectrum. However the atmosphere is filled with gasses that absorb the radiance emitted by the bird. The critical gasses are ozone and hydrogen. A new plot, shown in figure 5.5(b) shows the radiance incident on the camera with consideration of the transmittance of hydrogen. The transmittance of hydrogen was modelled using the critical vibrational frequency of hydrogen [97]. The absorption of ozone and other gasses is also accounted for further calculations [98]. It can clearly be seen that the optimal wavelengths to sense a bird is still from 9.5 to 14 µm.

The radiance emitted by the bird incident on the lens of the camera can be calculated as a function of the angle of the lens. This can be done by integrating the radiance in figure (b) between the desired wavelengths of 0.4-0.7µm and 9-14µm for the calculations of the conventional and infrared camera respectively. The radiance will then be a function of the solid angle. By multiplying the radiance with the angle of the lens with the bird, the radiance incident on the lens is calculated. However the radiance absorbed by the camera can be engrossed by the radiance from the background composed by the sun and earth. The spectral sky radiance is shown in figure 5.6(a) [99] and (b) [100] for the visible and infrared region respectively.

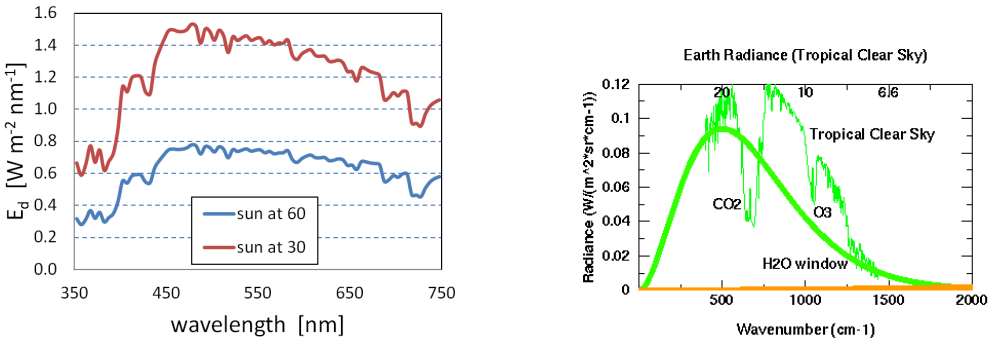

(a) At the visible spectrum

(b) At the infrared spectrum

Figure 5.6: Radiance of the background

The radiance incident on the camera from the bird is 0.76 mW, while the radiation from the background is 0.0358 mW for the infrared region. However the intensity from the bird at the visible spectrum is $1.013 \cdot 10^{-22}$ mW , while the background intensity is $2.11 \cdot 10^{-2}$ mW. The intensity from the bird at foggy weather is even less. This means that it is more convenient to detect a bird with an infrared camera from this distance. The radiance of the background being lower than that coming from the bird means a bird can easily be seen by an infrared camera at clear daylight and during clouded weathers. In order to sense the bird with an infrared camera the camera needs to have a certain sensitivity, meaning the minimum temperature difference the camera has to sense. NETD is the abbreviation for the 'Noise Equivalent Minimum Temperature Difference' [101]. The lower the NETD of a camera is for a certain range, the better the quality is. The required NETD can be calculated by dividing the incident intensity from the bird on the camera, $I_{detector}$, by the optics conversion factor. The optics conversion factor is the intensity from the bird, I_{bird} that causes the temperature of the surroundings to increase by 1 K [102]. The average peregrine falcon has a frontal area, A_{bird}, of 0.05 m^2 and a body temperature, T_{bird}, of 300 K [88]. Equation 5.6 shows the calculations performed to gain the NETD.

$$NETD = \frac{I_{detector}}{\frac{A_{bird} \cdot I_{bird}}{T_{bird}}} \tag{5.6}$$

A lens has great influence on the sensitivity of the camera; The greater the diameter the higher the NETD can be for this case [101]. A diameter of 100 mm gives a clear view of the bird at a NETD of 18.2 mK, while a diameter of 25 mm gives the same clear view at a sensitivity of 4.6 mK [101]. This means that a lens diameter of 100 mm is much more convenient to use. Objects equal or smaller than the assumed bird will not be sensed by a lens with a diameter of 25 mm if the camera is of lesser quality and has a higher minimum sensitivity. Object bigger than the assumed bird size will be sensed by the detectors. This however depends on the detectable temperature range of the camera, which is calculated in the section 5.2.1. Even though most metals have a high reflectivity and thus a high intensity, metals will be shown as a bright spot depending on the size of the aircraft.

Resolution, data rate and chosen cameras

Due to the infrared camera having a sensitivity of 18.2 mK, the system requires 55 colours to show one kelvin on a screen as shown in equation 5.7. To detect obstacles for example a bird a temperature difference of at least 10 K is required, thus a minimum of 550 colours. This means as calculated in equation 5.8 a system with a minimum colour depth of ten bits is needed to show these colours [103]. The minimum pixels needed to detect the falcon of one meter span is approximately three pixels [104]. A horizontal field of view of 100 m at a range of 753 m is used for the infrared camera to avoid obstacles. Since the field of view is 100 m and the falcon has a meter span the minimum horizontal resolution will need to be 300 pixels to recognize the bird on the screen. From a bit calculator[105] the compressed data

rate for the infrared camera is found to be 210 kb $\cdot$ s^{-1} with a horizontal resolution of 352 pixels and frame rate of 15 Hz. This frame rate is acceptable since the UAV only moves 1.8 m per frame at cruise speed. Keeping in mind the possible maximum data rate available for the uplink of the visuals from the camera that will be explained in the communication section 5.3, the conventional camera resolution can be chosen. The remaining uplink for the conventional camera is 0.6 Mb s^{-1}. An eight bit colour depth system will give a horizontal resolution of 702 pixels. Again three pixels are required per meter, this gives a field of view of approximately 234 m. Since the conventional camera is only used for obstacles nearby, the field of view of 82° calculated in equation 5.5 is assumed to be over the 234 m. This assumption is made because the conventional camera cannot be used during foggy weather to detect an obstacle that far and the field of view of the infrared camera is to low to cover obstacles from the sides. With these values a distance of 270 m is derived, which is just sufficient to avoid a bird coming from the sides even if the UAV is controlled manually. However these values are all calculated for the worst case scenario of the aircraft performances. Even if an obstacle is unexpectedly coming from the sides with a distance of less than 270 m, due to no pilot being on board, the UAV can take emergency measurements to avoid an obstacle at full force within a few meters as explained in section 4.1.

$$Colour\ per\ K = \frac{1}{18.2 \frac{mK}{colour}} = 55\ colours \tag{5.7}$$

$$Colour\ depth = \log_2 550 = 9.1\ bits \tag{5.8}$$

Now that the desired field of view, frame rate, range, resolution, sensitivity and temperature range are known a camera which is available on the market can be chosen. The cameras that reflect the desired specifications the most with consideration of the permitted weight and size is the FLIR T440 [106] and the HERO3 [107] for the infrared and conventional camera respectively. The FLIR T440 has the ability to adjust the field of view to sense obstacle further away. When interpolating the minimal sensitivity of this camera over the range or spatial resolution the sensitivity required for sensing the bird is sufficient. The weight of the camera is 880 grams. However the weight of the battery and the WiFi antenna provided in the camera by the manufacturer can be subtracted. When these are subtracted the total camera weight will be 650 grams [108]. The conventional camera already has the desired minimal specifications within the mass and volume limits. The data rate and resolution of the Hero3 camera can be lowered remotely if the pilot needs to take over. This is very convenient, because the autopilot will be able to see much further ahead with a higher resolution. The important specifications of both cameras can be found further in this chapter in table 5.5.

Avoidance algorithm

The algorithm compatible with the chosen cameras is 'Optical flow' [109]. The algorithm defines a certain background such as the sky. With the change in the background by the intensity coming from the obstacle, the distance to and position of the obstacle can be measured. By defining a new background each frame and subtracting the latest background with the one before the direction and speed of the obstacle can also be calculated. This means that even if an obstacle is not moving, for example a hot air balloon, the UAV will still be able to avoid obstacles since the position of the hot air balloon changes with respect to the UAV. The UAV will avoid the obstacle with a safety margin of ten m as specified before.

The steps taken by the UAV to avoid an obstacle are as follows. The UAV detects an obstacle as an intensity with a vector as shown in figure 5.7. The UAV will then compare the information from the ground with each frame obtained on board. This is done to avoid the UAV from avoiding a bird without consideration of other aircraft sensed by the radar and air traffic control. The radar will be designed in the next section. If an obstacle is present and the background is interrupted the UAV will avoid the obstacle with a safety margin of 10 m if it is an obstacle sensed on the on board cameras. Aircraft and other obstacles will be avoided with a safety margin of 152 m. Once the obstacle is avoided the UAV will resume the preprogrammed flight.

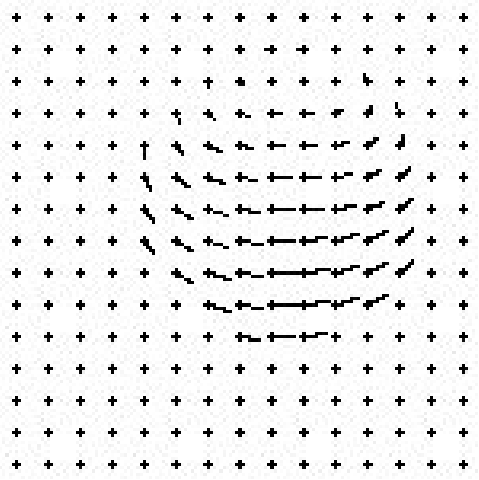

Figure 5.7: New frame sensed by a sensor subtracted with last frame

5.2.2 Obstacle detection on the ground

Obstacle detection on ground is mainly done to provide the UAV with information about the speed and position of other aircraft and to avoid laser hazards. The laser will be shut down immediately if an obstacle gets in the range the pilot or bird could be blinded. This means these obstacles must be tracked on the ground.

Radar system

Obstacle detection is also performed at each laser base station by means of radars and thermal cameras. In order to choose a radar some minor calculations and analysis are performed. The choice of a radar system depends mainly on the revolutions per minute, the operative frequency band and the maximum and minimum range. The operative frequency band is chosen on basis of the range and the propagation during rain which is shown in figure 5.8 [110]. The optimal frequency to operate at according to the figure is ten GHz. The range is estimated to be the range of the laser plus the time needed to take actions, for example to turn off the laser or take evasive manoeuvres for the UAV. However a helicopter which is the fastest object at the UAVs height nears the laser base station while taking actions. The range of the radar is extended with the time needed for actions times a speed of 260 $\frac{km}{h}$ of the helicopter. The revolutions per minute is calculated in equation 5.9 since the range is known. The bird is again used as the smallest obstacle to be detected.

$$Delay\,time = \tau = R \cdot 2/c \tag{5.9a}$$

$$Angle\,with\,bird = \zeta = \arctan\frac{1}{R} \tag{5.9b}$$

$$rpm = \frac{360^\circ}{\zeta} \cdot \tau \tag{5.9c}$$

If the UAV flies at an altitude of 230 m and the maximum vertical angle the laser can operate at is 40° this would give a minimum range of 300 m. Now that the most important parameters are known a radar system can be chosen from the market. The chosen radar system is the 'Furuno-far 2117'[111] which has slightly different values for the parameters calculated and estimated. The Furuno-far 2117 operates at the X-band with a frequency of 9.5 GHz. This frequency has like the suggested 10 GHz in figure 5.8 a low attenuation. Although the Furuno-far 2117 has a lower RPM of 42 instead of 52 RPM, the difference in time between each frame will only differ 0.3 s. This loss in time is however compensated for by the full coverage of the target area by all four radars together.

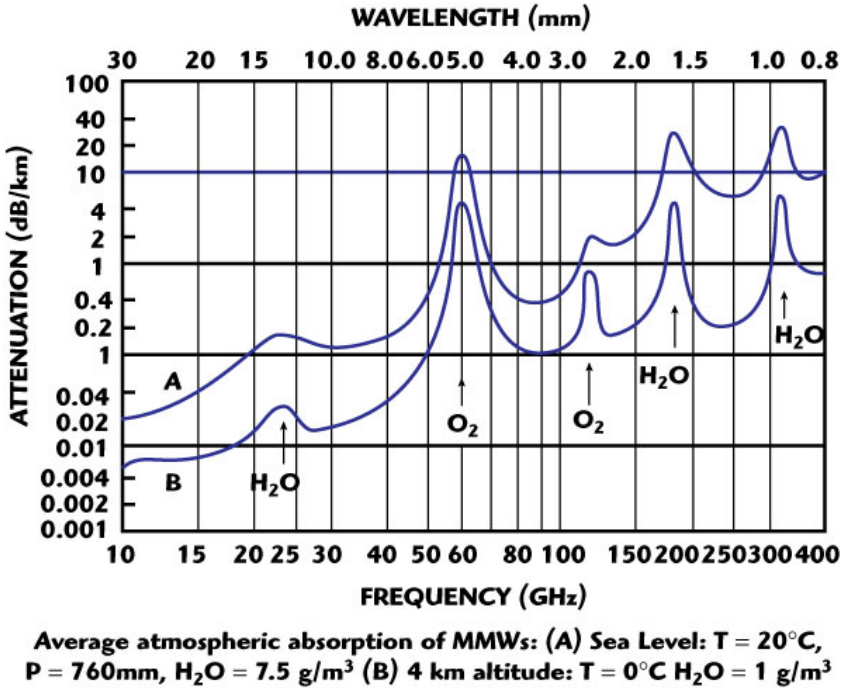

Figure 5.8: Atmospheric absorption of MMW

Thermal camera

The thermal camera used on the ground has several purposes. It can be used to detect obstacles on the laser path but also to detect if malfunctions occur at the laser panels. This means that the thermal camera can be placed on the laser platform to move along with the laser.

Detecting the malfunctions or performance degradation of the laser panels needs a relatively higher sensitivity and thermal range. This due to the small size and high temperatures of the panels. The same equations for the thermal camera on board can be used for the ground camera. The camera that meets the desired specifications the most is the 'FLIR PT606' [112] with a lens diameter of 100 mm and a sensitivity of 15 mK at a range of 3.2 km. The obstacles will also be detected and laser hazerds can be avoided with the field of view of this camera shown in table 5.5.

Table 5.5: Specifications of the detectors

Parameter	Unit	Conventional	Thermal(UAV)	Radar	Thermal (ground)
Range	km	7	0.8	5	3.2
Sensitivity	mK	-	< 45	-	15
Resolution	pixels	adjustable	320·240	-	640·320
Field of view/Beamwidth	°	120	25·19	0.95·20	34·28
Weight	g	70	650	-	-
Cost	EUR	449	8650	15788	23300

5.2.3 RAMS analysis

The chosen cameras and radar are reliable in the sense that they will perform the requested tasks for the required 5 years. However the conventional camera will not be available to operate when the view is blocked by fog or mist. The thermal camera compensate for this. Even if all on board cameras are malfunctioning. The radar and thermal camera on ground are sufficient to provide the UAV with

information to continue the flight which is why the overall systems reliability and safety are 100% and 0 accidents respectively. The system will however not be available at heavy rain and snowfall [111] [112]. The UAV must land to prevent any laser hazards or collisions due to the all cameras and the radar being unable to sense any obstacles at such weather conditions. Maintaining the obstacle detectors is not needed frequently. The ground obstacle detectors do not require the UAV to land and can be maintained or replaced if needed. The obstacle detectors on board can be maintained or replaced relatively fast during the regular maintenance stops of the UAV. This due to the cameras being plug and playable [107] [106].

5.3 Communications

In the previous stage of the project [5], it is decided that the UAV shall use a radio communication system to transfer the data to the laser base stations. The communication system consists basically of a transmitter, receiver and an antenna. Although the same transmitter and receiver will be on the UAV as on the laser base station, two different antennas are used for the laser station and the UAV. An omnidirectional antenna is used on the UAV and a sector antenna is used for the laser base station. The sector antenna is kind of a directional antenna but with a sector shaped radiation pattern as it can be seen in figure 5.9. The communication link is established between the UAV and the nearest laser base station to provide a link with the least amount of losses. Then the data received at the laser base station are provided to the ground station through conventional lines. Also the ground station provides and is provided by data from all parties through conventional lines.

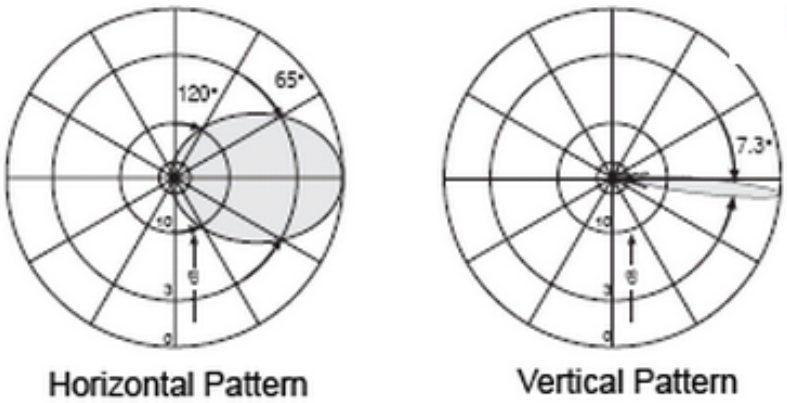

Figure 5.9: Plot of sector radiation pattern

5.3.1 Link Budget

Communication systems are crucial for every mission where data transfer is essential. To ensure a functional link to support the data transfer rate, a link budget calculation is done to determine the link margin. The link margin is measured in decibels and requires positive value, otherwise the chosen communication system needs to be readjusted. The link budget calculation will account for all the gains and losses from the transmitter to the receiver. A link overview is presented in figure 5.10

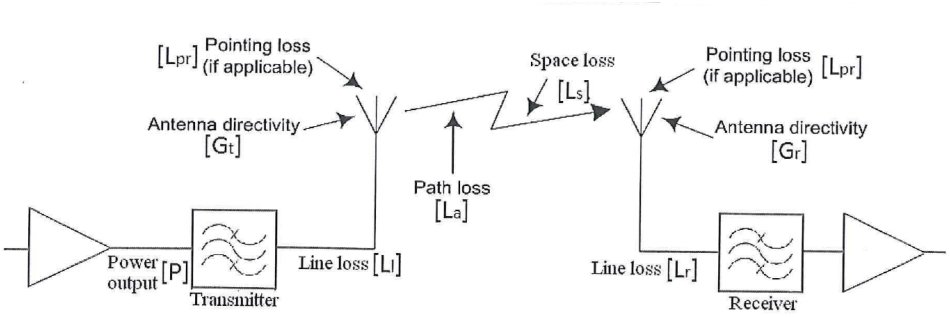

Figure 5.10: Link overview of the communication system.

The transmitter used for this system is the Clyde Space transmitter S-band STX with data rates up to 2 Mb s^{-1} [113]. The receiver used is the VDR1 Analog FM Diversity Video which is provided by Rugged RF and Microwave Products. The antenna used on the UAV is an omnidirectional antenna with 4 dB gain [114]. A sector antenna is used for the laser base stations with antenna gain of 16 dB [114]. Both antennas are provided by Cobham Antenna systems. Using the data sheets provided by the manufacturer of these units [113] [114] [115] and using some assumptions based on the book [56], the link budget calculation is done and the output is presented in table 5.6.

Table 5.6: Output link budget from the different components of the communication systems.

		Operation	**Value**	**Unit**
Transmitter	T_x Power P_T	+	30	[dBm]
	T_x Line losses $L_{T,Line}$	+	-0.15	[dB]
	T_x Antenna gain G_T	+	4.0	[dBi]
	T_x pointing losses $L_{T,Point}$	+	0.0	[dB]
	T_x Radome loss $L_{T,Radome}$	+	0.0	[dB]
	EIRP	33.85		[dBm]
Propagation	Free space loss FSPL	+	-112.1	[dB]
	Atmospheric absorption L_{ATM}	+	-0.5	[dB]
	Precipitation absorption $L_{P,Precip}$	+	0.0	[dB]
	Total Propagation loss	-112.6		[dB]
Receiver	R_x Antenna gain G_R	+	16	[dBi]
	R_x Pointing loss $L_{R,Point}$	+	-0.5	[dB]
	R_x Radome loss $L_{R,Radome}$	+	0.0	[dB]
	R_x Line losses $L_{R,Line}$	+	-2.5	[dB]
	R_x Spread loss $L_{R,Spread}$	+	-1.0	[dB]
	R_x Polarization loss $L_{R,Polar}$	+	-6	[dB]
	Effective carrier power	-72.3		[dBm]
Noise	Thermal noise	-	-174	[dBm Hz^{-1}]
	R_x Noise bandwidth BW	-	80	[dBHz]
	R_x Noise figure NF	-	3.0	[dB]
	Effective noise power	-91		[dBm]
Summary	Available SNR	+	18.63	[dB]
	Required SNR	-	9.6	[dB]
	Link margin	9.03		[dB]

Transmitter

The power output P_T of the transmitter depends on the specifications of the transmitter. The chosen transmitter has a RF power of 1 W which is 30 dBm. The line loss $L_{T,Line}$ is found using the data sheet

of the cable providers [116]. The Totoku CF500 cables are used which have a total line losses for the UAV of -0.15 dB. The transmit antenna gain depends on the specified antenna which is 4 dBi which is suitable for the frequencies from 2400 to 2500 MHz . Since the antenna used is an omnidirectional antenna, the pointing losses $L_{T,Point}$ of the transmitter is negligible so it is considered zero [56].

Some antennas require a radome which is a structural barrier to protect it from rain, ice and humidity. These radomes affect the electromagnetic signal which creates some radome losses for the link signal. However this is not the case for both antennas used for transmitting and receiving because they both do not require radomes. So the $L_{T,Radome}$ and $L_{R,Radome}$ are considered zero [56].

The Effective isotropic radiated power of the system (EIRP) is the sum of the transmitter power, gain and losses. This is determined to be 33.85 dBm which is still until the regulated limit set by the Federal Communication Commission. This limit is set to prevent jamming from other RF systems. However in emergency situations, this limit is exceeded to establish a stronger communication link.

Propagation

Due to the fact that the electromagnetic wave travels through a medium like air there exists some losses which are counted for in the propagation calculation. The free space loss (FSPL) is proportional to the square of the frequency and the square of the distance. Since the maximum distance (d) considered is 4 km and the frequency (f) used is 2400 MHz, a space loss of -112.4 dB is found using the equation 5.10. Other losses like the atmospheric absorption L_{ATM} is estimated -0.5 dB because for frequencies lower than 3 GHz it is negligible [117]. Perception absorption is caused by heavy rain which causes high attenuation at frequencies higher than 5 GHz, so $L_{P,Precip}$ is considered to be zero [56]. Eventually the total propagation losses are summed up to -112.6 dB.

$$\mathbf{FSPL} = 20(\log_{10}(d)) + 20(\log_{10}(f)) - 147.5 \tag{5.10}$$

Receiver

The same calculation process is used for the receiver. The antenna gain is 16 dBi. An estimation of -0.5 dB for the pointing losses $L_{R,Point}$ is done based on the fact that the tracking system of this design is considered pretty accurate. Also using the same cable for the receiver, the line loss $L_{R,Line}$ is found to be -2.5 dB [116]. Other extra losses also exist for the receiver like spread implementation loss $L_{R,Spread}$ which is the loss due to spreading the signal in a frequency domain resulting in signals with wider bandwidth. This is done to improve resistance to interference, noise and increase the data transfer security. So a loss -1 dB is taken based on a typical range given by [56]. Furthermore the polarisation losses that arises from the way the antennas are positioned, if any of the antennas used during transmission or receiving is titled losses are generated. These losses are proportional to the square of the misalignment angle which equals the bank angle for aircraft. Using the maximum bank angle of 45 °, the loss is calculated using equation 5.11 [56] which gives a loss of - 6 dB. The effective carrier power is the sum of the EIRP, all the receiver losses L_R and the receiver antenna gain resulting in a -72.3 dBm.

$$L_{R,Polar} = 20(\log_{10}[\cos(\theta_{Align})]) \tag{5.11}$$

Noise

The thermal noise of this system is caused by the molecular vibrations and is proportional to the absolute temperature. Considering an average temperature of 290K, the thermal noise is determined to be -174 dBm Hz^{-1} [56]. Then the receiver noise bandwidth depends on the used ideal receiver bandwidth and it is calculated to be 80 dB. The Noise figure is provided by the receiver manufacturer and it has a value of 3 dB [118]. The effective noise power is the sum of the thermal noise, receiver noise and the noise figure.

Summary

The available signal to noise ratio (SNR) is the effective carrier power minus the effective noise power which gives a SNR of 18.6 dB. Now that the available SNR is found, the required SNR is crucial to know if the communication link works. The required SNR is found using the equation 5.12. Where the E_B/N_o for Bit Error Rate (BER) = 10^-5 is for the QPSK modulation -9.6 dB [119] and the ratio R_{data}/B for QPSK is approximately 1 [56]. So the link margin is found to be 9.03 dB. This means that the communication system provides a functional link to support our required transfer data rate.

$$\mathbf{SNR} = \frac{E_B}{N_o} + 10(\log_{10} \frac{R_{data}}{B}) \tag{5.12}$$

5.3.2 Data Management

All communication systems have a common purpose of transferring data from one point to another as efficient as possible. For this mission profile there are different types of data required to be transferred like flight control, tracking, obstacle detection and payload data. Due to the transfer rate limit of 2 Mb s^{-1}, managing the transferred data is essential which is done by dividing the data into different packages that have to be transferred in a specific situation. Flight control and tracking data which are crucial to keep the UAV in the sky are constantly being transferred to the nearest laser base station. Flight control and tracking data are 5 kb s^{-1} and 8 kb s^{-1} respectively as stated in section 5.1 and 3.1. Obstacle detection data is a collection of two cameras a conventional camera and a thermal camera that require approximately 600 kb s^{-1}, 208 kb s^{-1} respectively as it can be seen in section 5.2. So the only the conventional camera image and data are transferred to the station during cruise flight. This gives a minimum requirement of 613 kb s^{-1} to keep the aircraft in the air. Furthermore the data of both cameras will be sent to the station during emergency situations when the autopilots fail. Payload data that are very important to the customer are transmitted only during cruise flight conditions because during emergency situations only the minimum required data that have to be transferred is sent to prevent any unnecessary losses. From the minimum required data rate for the cruise flight, a transfer rate of 1360 Kb s^{-1} is available to be used for the payload data. For this mission profile the available data rate is enough to support a camera with resolution of (704·480) and 25 FPS as frame rate [105].

As mentioned before in the previous stage of the project [5], a processor is used to handle all the internal communication within the UAV. The processor sends and receives all the data and commands required for proper operations. Also the processor is used to compute the tracking data on board instead of sending all the data back to the station to be processed in the ground station. This reduces the tracking data required to be transferred by a factor of 100 which was determined in section 3.1. A summary of the managed data rates is presented in table 5.7. Furthermore a data handling block is presented in figure 5.11, the data being transferred from the different subsystems to each other is defined in the figure.

Table 5.7: Data rates required from the different subsystems.

System	**Required data rate** [kb s^{-1}]
Flight Control	5
Tracking	8
Obstacle Detection	600 208
Cruise Flight	613
Payload	1387
Emergency Conditions	821

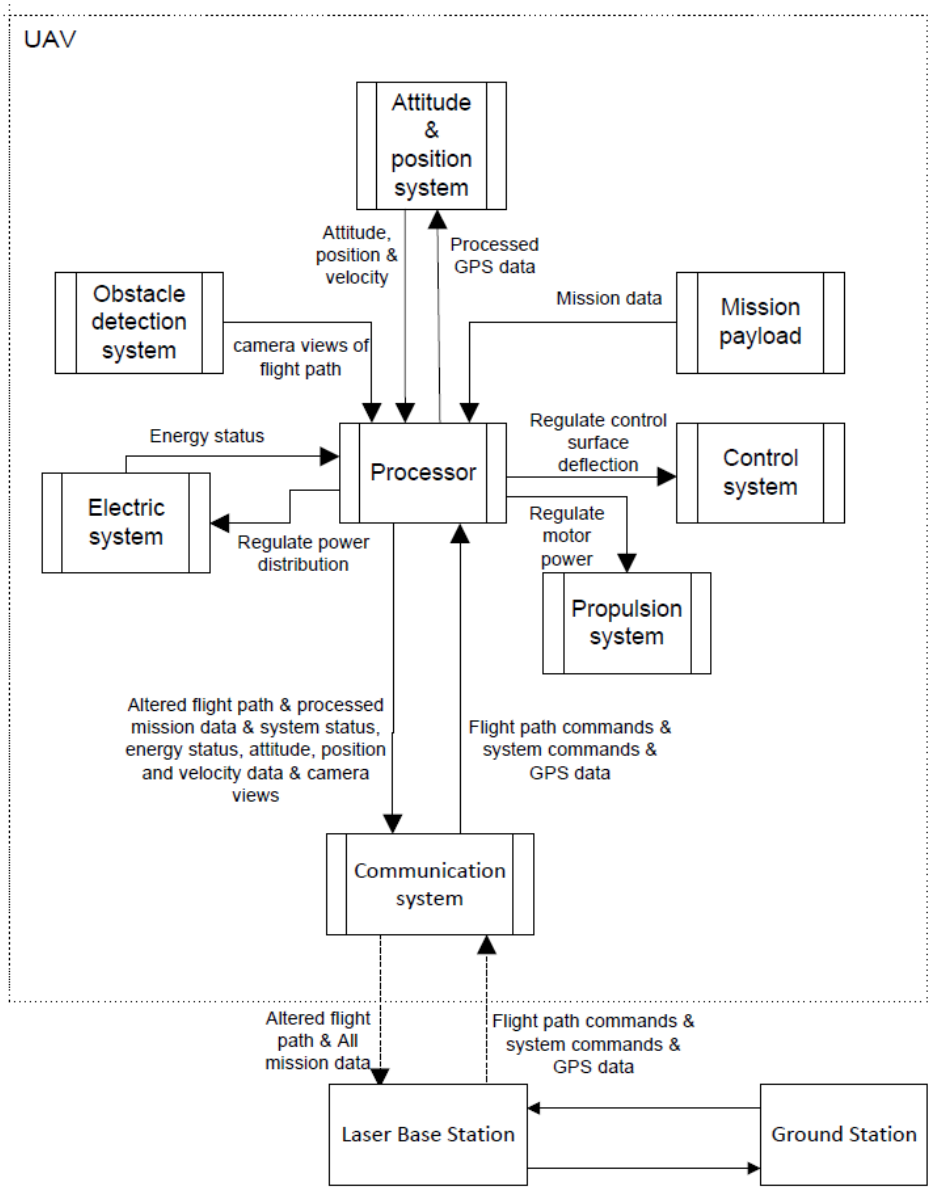

Figure 5.11: Plot of the Data Handling Block.

5.3.3 Weight and cost Estimation

The weight of the communication system is easily estimated using the weight data sheets provided by the manufacturer[113] [120] [115]. The total weight of the communication system on board the UAV is 0.63 kg. The weight of the system components on the UAV is presented in table 5.8.

To estimate the cost of the communication system, the cost of the different components is just summed up to give an initial estimation cost, then an estimation of the operational cost is deduced using a logic approach. So the total initial cost of the communication system for four laser base stations and the UAV is approximately EUR 52,122. The cost of each component is presented in table 5.8. These costs are found either by using the data sheets of component or contacting the manufacturers[113] [120] [115].

Furthermore the operational cost is estimated on the assumption that the communication system

Table 5.8: System Weight and Costs

Item	**Weight** [kg]	**Cost** [EUR]
Transmitter	0.08	6,670
Receiver	0.17	3,252
Omni Antenna	0.38	440
Sector Antenna	1.7	518
Total On board Sys.	0.63	10,362
Total Base Station Sys.	1.95	10,440

on the laser base station is maintained one day per month by one engineer for EUR 40 per hour. This gives us a yearly estimate of EUR 3,840 per station. Although the same approach is used to estimate the operational cost of the UAV communication system. The system on board is only checked one day every 2 month because the system on board uses an omnidirectional antenna so there is no mechanical components that affect the link strength. Taking that into account the cost becomes EUR 1,920. In conclusion this gives a yearly cost of approximately EUR 17,280.

5.3.4 Sensitivity Analysis

The communication system is one of the most systems that are built to serve a specific goal, any change in the parameters or the design requirements the whole system could have to be rebuilt. Most important parameters that affect the whole system are the required transfer data rate, weight and the polarisation of the antenna. The required transfer data rate is mainly dependable on the type of data sent since a video data require much higher than a normal command. This is the reason why most video cameras compress their data before being sent. In this mission profile MPEG-4 is considered as a compressing code. MPEG-4 is used since they are most compatible with most cameras and delivers improved compression efficiency [121], furthermore this coding delivers a live feedback with high enough efficiency as mentioned in the section 5.2. Weight is another constraint because of the small size of the UAV, the weight of the communication system is limited. So a trade off between the weight and the communication performance is done. This means that there are communication systems with higher data rates but they are 5 times heavier which is unacceptable for the mission profile. Also the polarisation of the antenna is important due to the fact that both the transmitting and receiving antenna need to have the same polarisation or losses will exist.

However the communication system built for this mission profile should be suitable for the mission requirements. But due to the nature of electromagnetic waves the 2 Mb s^{-1} transfer data rate will not be a constant transfer rate, however this signal deterioration is low so it will not affect the operation of the aircraft. This irregularity is caused by the interference and jamming by other radio communication systems and fading of the signal power. To solve this problem a spread spectrum is implemented to prevent these interferences, jamming and noise. This is done by using modulations like frequency shift keying (FSK) for this mission profile. Also phase shift keying (PSK) is used by the manufacturer to produce higher data rates.

5.4 Launch and Recovery

A conceptual design of the launch and recovery mechanisms are made. The UAV requires a launch system capable of deploying it to the desired altitude within certain design limits. The same design limits are also considered for the recovery system to land the UAV safely for maintenance procedures. A winch is used to launch the UAV, while a net is implemented to recover the UAV.

5.4.1 Launch

Conventional aircraft use landing gears and thrusters to take off. This however requires a lot of energy and weight. Winch launching the UAV is much more convenient since the landing gear can be left out of the equation. Although winch launching is mainly done for gliders, the UAV will also be able to get up to the desired height and speed [122]. The principle of winch launching is as follows. An aircraft will be pulled by a winch at its belly, which is driven by a diesel or electric motor. Pulling it at the nose will cause a high strain which requires structural improvements [123]. Once the aircraft has reached its stall speed it can leave the ground. This is done by pulling the nose slightly up to create lift. The cable will keep pulling the aircraft until until the desired height and aircraft flight path angle are achieved. The cable will then drop by means of a parachute [124].

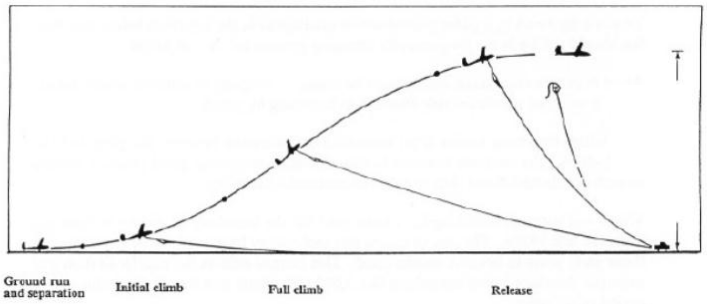

Figure 5.12: Phases of winch launching

Winch launching consists of three situations as can be seen in figure 5.12 [125]. The first situation is the ground run. The transition from the ground to the desired height is the second situation. The third situation starts once the UAV pulls its nose back down and the cable is dropped. The figures shown in this chapter are for a conventional glider, but the same principle accounts for a canard wing aircraft. The results of the calculations done in the launch section are put in table 5.9 at the end of this section.

Ground run

While on the ground the UAV is pulled by the winch to get the UAV to the stall speed. A free body diagram is set up for this situation in figure 5.13(a) [126]. Due to the stall speed being an unstable speed to fly at, a launch speed of 1.3 times the stall speed is assumed. During the ground run the weight, W, will be greater than the lift, L. However just before the moment the stall speed is reached and the UAV is about the leave the ground the lift will be equal to the weight. Since the speed is known to be 1.3 times the stall speed the lift coefficient, C_L can be calculated by first setting up the equations of motion. The equations of motion are shown in equation 5.13a and 5.13b. The right side term in equation 5.13a is the circular acceleration of the UAV with V being the speed of the aircraft at that moment. The UAV is assumed to be placed in a loop during the ground run and transition phase [127]. R is the height the UAV has to be placed at. By replacing lift in equation 5.13a with equation 5.13c the lift coefficient can be calculated. With the lift coefficient the drag coefficient, C_D, can be gained from the C_L-C_D curve in figure 4.22. Once the drag coefficient is known, the tension in the cable can be calculated with equation 5.13b. However the tension in the cable depends on the chosen acceleration, a. The optimal acceleration can be chosen by iteration from further analysis, because the load factor in its turn depends on the tension in the cable. The length of the ground run is also calculated from the acceleration, this is done in subsection 5.4.1.

$$L - W = \frac{m \cdot V^2}{R} \tag{5.13a}$$

$$C - D = a \cdot m \tag{5.13b}$$

$$L = \frac{1}{2} \cdot \rho \cdot V^2 \cdot S \cdot C_L \tag{5.13c}$$

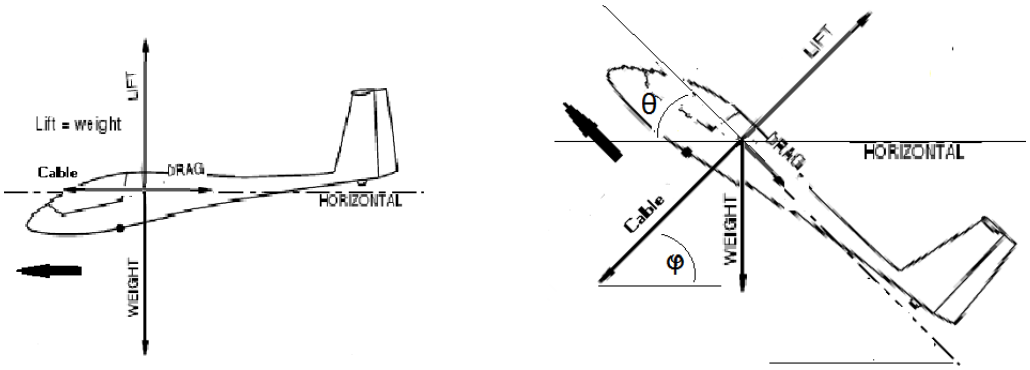

(a) During the ground run

(b) During the climb

Figure 5.13: Free body diagram

Climb

After rotating into the climb phase, as done in figure 5.14 [128], the UAV will fly up with a steady flight path angle as in figure 5.13(b) until it has reached the desired height. The equations of motion for this

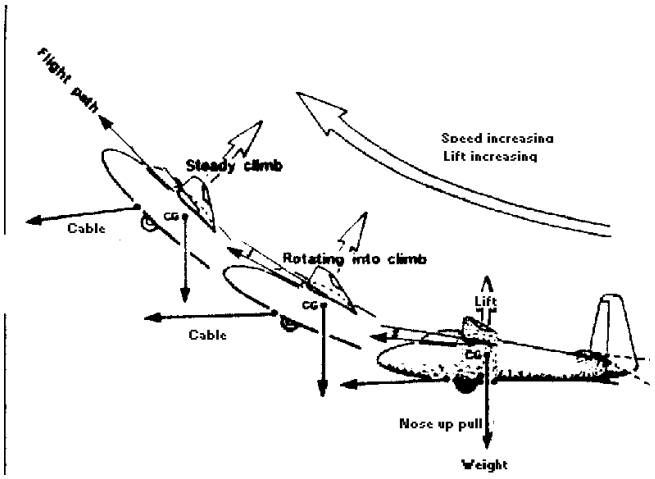

Figure 5.14: Transition from ground to mid-air

situation are shown in equation 5.14a and 5.14b. Since the speed, weight and cable tension are known the C_L can be calculated as a function of ϕ_c and θ. ϕ_c is a vector from 0° to 90°, while θ is from 0° to 45° and back to 0°. θ has a maximum of 45° because this is the assumed to be the optimal flight path angle at which all forces outweigh each other [123]. With C_L known for every ϕ_c from equation 5.14a, the maximum load factor can be calculated. The load factor is found by dividing the lift over the weight of the UAV. The lift can be calculated with equation 5.13c since all values are known. Figure 5.15 shows the load factor plotted against the angle of the winch cable with the ground, ϕ_c. The values used to plot this figure are put in table 5.9. According to the technical requirements for designing a winch the steady climb should be achieved as soon as possible [129]. Once the UAV has pulled its nose up and reached the steady climb with a flight path angle, θ, of 45° the load factor and C_L increase

linearly with the sine of ϕ_c as the only variable.

$$L - W \cdot \cos\theta - C \cdot \sin\phi_c \cos\theta = \frac{m \cdot V^2}{R} \tag{5.14a}$$

$$C \cdot \cos\phi_c \cos\theta - D = a \cdot m \tag{5.14b}$$

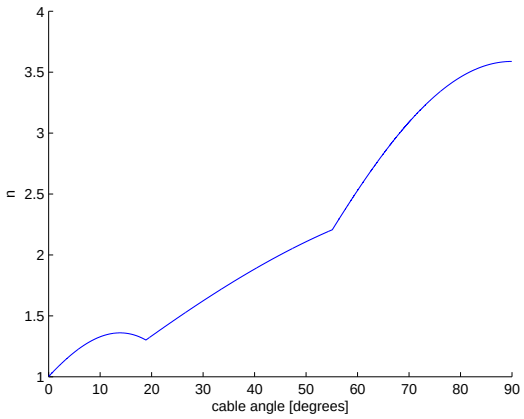

Figure 5.15: Load factor against ϕ_c without releasing the cable at 70°

Release

Now that the UAV has arrived at the desired height the nose can be lowered again. The cable is still on the UAV at around 55° while pulling the nose down. Pulling the nose down increases the load factor more because of the excessive lift generated by the increase in speed as can be seen in figure 5.15. Once a certain ϕ or maximum allowable tension in the cable has been reached the cable can be dropped. If the maximum allowed load factor on the UAV is surpassed during the climb the cable will break by means of a weak link in the cable as shown in figure 5.16. Once the cable breaks or is dropped the lift and thus angle of attack needed will be lower. This will lower the load factor on the UAV.

The reason that this much lift is needed to be generated during the launch is due to the speed of the UAV, the horizontal acceleration and cable tension being assumed to be constant over the whole climb. In a real situation the cable tension will be lowered gradually. A simulation where all three of these constant are implemented as variables will be much more accurate. Thrust is also not implemented in this case. For a smooth transition at the release of the cable the power from the propeller must equal the tension of the cable in the direction of the flight path. The transition is however assumed to be done in an instant.

Cable length and pull speed

The cable length can be estimated with the energy method and the acceleration. Equation 5.15 is used to calculate the ground run length, s, and contraction speed of the winch, $\frac{dL}{dt}$. t is the duration of each phase and V_z the speed of the UAV in the direction normal to the ground. . The speed of the UAV is equal to the speed of contraction of the winch at phase 1. Equation 5.16 is used to calculate the cable contraction speed needed at phase 2, while equation 5.17 is used for phase 3. These three summed up plus the aimed height of the UAV will give the minimum total length of the cable. The required horsepower can be calculated by dividing the energy needed over the time it needed to achieve that energy level. The highest energy level change occurs during the ground run. This means the maximum horsepower the winch needs can be calculated from the ground run.

The maximum power needed increases even more if the UAV is pulled on its belly, dragging over the ground. This causes a high friction drag due to the ground friction. However in order to reduce the structural weight and the friction drag during the ground run the UAV will not be moving on its belly but on a board. The UAV is connected with a board which moves on rails. This connection of the UAV with the 'railboard' is done by small walls, which are put in front of the wing. While pulling the aircraft the railboard will also be pulled by the wings of the aircraft till the aircraft points its nose up slightly to fly. The railboard walls will not have a high influence on the structures of the wing since the weight of the railboard and the drag caused by the rails are relatively low. The connection of the cable with the aircraft is done by means of a tow hook. The tow hook will glide out of the attachment part at the chosen flight path angle. This attachment part is a ring which is shown in figure 5.16.

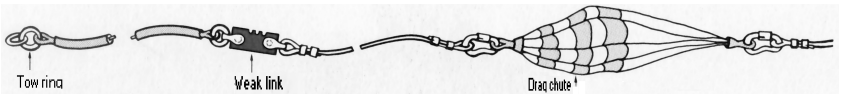

Figure 5.16: The weak link and drag chute implemented in the cable

$$t = \frac{V}{a} \tag{5.15a}$$

$$s = \frac{1}{2} \cdot a \cdot t^2 \tag{5.15b}$$

$$\frac{dL}{dt} = \frac{s}{t} \tag{5.15c}$$

$$E = \frac{1}{2} \cdot m \cdot V^2 + m \cdot g \cdot h \tag{5.16a}$$

$$V_z = V \cdot \sin\theta_{steady} \tag{5.16b}$$

$$t = \frac{h}{V_z} \tag{5.16c}$$

$$\frac{dL}{dt} = \frac{\frac{E}{C}}{t} \tag{5.16d}$$

$$t = \frac{h \cdot \tan\phi_{c@release}}{V} \tag{5.17a}$$

$$\frac{dL}{dt} = \frac{h_* - h}{t} \tag{5.17b}$$

Table 5.9: Results of calculated and assumed parameters

Parameter	**Value[unit]**	**Parameter**	**Value[unit]**
Destination height	300[m]	Horizontal acceleration	2.5G[m·s^{-2}]
Runway length phase 1,2 and 3	10, 125 and 40[m]	Allowable acceleration on UAV structure	4G[m·s^{-2}]
Length cable	481.3[m]	Cable pull speed phase 1,2 and 3	10.9, 6.4 and 1.9[m·s^{-1}]
Release cable angle	60[°]	Maximum load factor during climb	2.5 [-]
Winch power	8 [kW]	Allowable load factor on UAV structure	4 [-]
Cable tension	799.4[N]	Propeller power at release	247[N]
Constant UAV speed	22[m·s^{-1}]		

Cost analysis

The cost for the deployment can be divided into operational and acquisition costs. Operational costs include fuel, rope replacement,engine maintenance, rope retrieving mechanism maintenance. Table 5.10 [130] shows the operational costs.

Table 5.10: Operational costs

Parameter	**Value[EUR]**
Fuel (1/2 Litre)	0.38
Cable maintenance(including drag chute)	1.5
Railboard maintenance	0.23
Total operational cost per launch	2.11

The acquisition costs are the buy-in costs divided over the expected amount of launches. The winch costs EUR 30,000 and the end of life is expected by the manufacturer to be at least 30 years by the manufacturer [122]. The launches per month will approximately be one launch for own needs. The cost per launch would be EUR 84 per launch. However the winch can according to the specifications of the manufacturer launch 120000 UAVs and gliders over the same 30 years. A 120000 launches per lifetime would mean EUR 1.5 per launch [122]. Leasing the winch to others for EUR 1.5 per launch will cover up the acquisition cost. The lease can be increased much more according to the operational costs and the market demand to cover up the operational costs too[130]. The winch launcher that reflects the desired specifications the most is the EVO2 [122], which weights 1800 kg and is designed for the launch of gliders. However a winch launcher, with approximately a fourth of the EVO2 weight, is being designed by manufacturer Skylaunch [122] for the launch of the laser assisted UAV. The winch will be designed with approximately the same parameters as shown in table 5.9 and a dyneema cable of 2mm to pull the UAV with [131]. The cost will be approximately EUR 30,000. The location of the launch site has great influence on the load on the UAV; The longer the runway is the more the horizontal acceleration of the UAV can be decreased. The location of the launch site is shown in figure 5.18. This location is chosen as such since it has a runway which fits the calculated parameters of table 5.9 and is next to one of the landing sites. This is done to minimise the transportation of the UAV.

RAMS Analysis

The winch system is reliable in the sense that it can perform its task for the required 5 years. However it will not be available every second. The launch can be postponed due to an obstacle interrupting the launch which is why the availability is low. This obstacle can for example be a bird passing by. Maintaining the winch launch is theoretically not required. Due to the winch being able to perform 120,000 launches over an end of life of 30 years [122], the winch will be able to withstand 60 launches over the required 5 years. Winch launching has its risks. Winch launching failures often occur due to pilot errors [128]. Pilots tend to increase the angle of attack to much during the climb which increases the load factor to much [128]. The structure of the UAV may fail afterwards. This is however compensated for by a weaklink as explained earlier in this section. Due to the launch being a process with a few variables it can be preprogrammed into the autopilot. The pilot will be replaced by the autopilot which can be perform the launch without any pilot errors.

5.4.2 Recovery

The UAV is recovered by using a net system. The sequence of events is illustrated in Figure 5.17 [56]. The UAV flies into the net and its motion relative to the landing platform is stopped. Just before flying into the net the UAV flight path angle is increased to reach stall so the UAV will hit the net with its bottom side. Once the UAV is arrested, the kinetic energy is exchanged into potential energy resulting in the height loss at rest as shown in Figure 5.17.

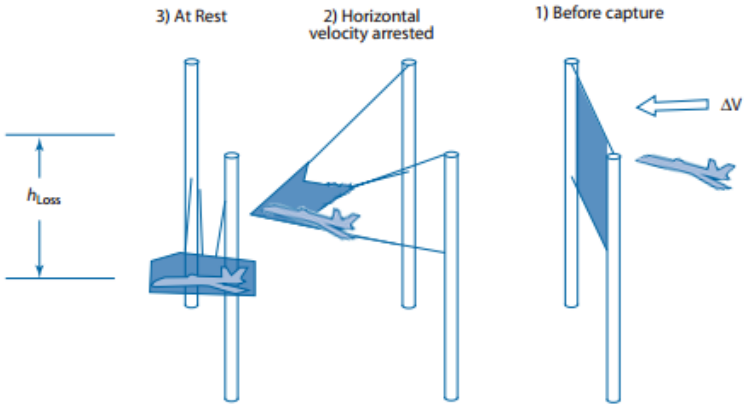

Figure 5.17: Net recovery sequence

Net system

The net system is sized by employing the energy equation. Neglecting the thrust losses and the changes to the stored energy, the energy that the net has to absorb is given by equation 5.18.

$$E_{recovery} = \frac{W_{recovery}}{2 \cdot g} \cdot |\Delta V|^2 + W_{recovery} \cdot h_{loss} \tag{5.18}$$

Where $W_{recovery}$ is the weight of the UAV, ΔV is the change in speed, which is the difference between the stall speed and the speed at rest. h_{loss} is the change in height as illustrated in Figure 5.17. By considering the length and the span of the UAV which are 2.5 m and 3.1 m respectively, a safe value of 4 m is estimated for the h_{loss} . Using the stall speed 60 kmh^{-1} and the weight 31 kg, the energy of the net is found to be 5523 J.

The work to counter the UAV energy comes from the tension of the four cables supporting the net. Equation 5.19 gives the relation between the net energy and the tension in each cable T_{cable}. The tension in each cable is assumed to be constant.

$$E_{net} = 4 \int T_{cable}(t) \cdot \frac{\partial L_{extend}}{\partial t}(t) \cdot dt \tag{5.19}$$

Where L_{extend} is the linear extension of the cable supporting a corner of the net. The time t is the time from the moment the UAV comes in contact with the net to when it comes to rest. The time when the linear extension is assumed to be maximum is when t equals 1. The extension is calculated using

$$L_{extend} = \frac{a}{2} \cdot t^2 \tag{5.20}$$

where a is the UAV deceleration which is mainly the load exerted on the UAV by the net. The structure of the aircraft should be able to handle a load factor of 4 but for landing only a load factor of 1 is considered. Using a linear cable transducer the load factor in the cables is adjustable, so the linear extension of the cable is approximately found to be 5 m.

Using the value found for the $E_{recovery}$ using equation 5.18 and cable extension found with equation 5.20, the required cable tension is found to be 277 N. From the required tension, a cable is chosen which is a nylon coated stainless steel that handles that kind of tension [132] [133].

Material, Operations and Cost

The landing system is built out of two steel poles for support. Four linear transducers with nylon coated stainless steel cables are fixed on the two poles from one end and the other end are attached to the net. The material used for the net is made of plastic netting reinforced by rubber bands [134] and the dimensions of the net are 6 by 6 meters. The are two landing sites in the 10 by 10 kilometre area to be able to land both UAVs flying in the network simultaneously in the extreme event of both failing at the same time. Furthermore using two landing sites, reduces the amount of time and power needed to reach the landing site. The total initial cost of the landing mechanism is EUR 779 for each landing site. The individual cost of each unit is given in table 5.11 [134] [135] [136]. The location of landing sites is shown with the network in the figure5.18. The landing sites are chosen to be in an open space where landing will not cause any safety problems. The landing site located in the west is only used during emergencies. This is done to decrease the transportation time of the UAV.

Table 5.11: Recovery System Costs

Item	**Cost**[EUR]
4 Cable Transducer	620
Net	45
2 Support pole	114
Total Cost	779

RAMS Analysis

The net system is reliable as it can carry out its functions for the specified conditions. The fail rate of the landing mechanism is kept under control by adding a safety net to catch the UAV in case of a landing failure. The recovery by net system is already being produced for larger UAVs and all the units are relatively easily assembled. Furthermore considering the cost of the landing site and its design, multiple landing sites are constructed. The maintainability of the system is performed ocassionally and in a short time due to the relatively simple design of the system. However the landing using a net is a safe method, the risk lies with the pilot controlling the aircraft just before landing because he has to reach stall speed in front of the net.

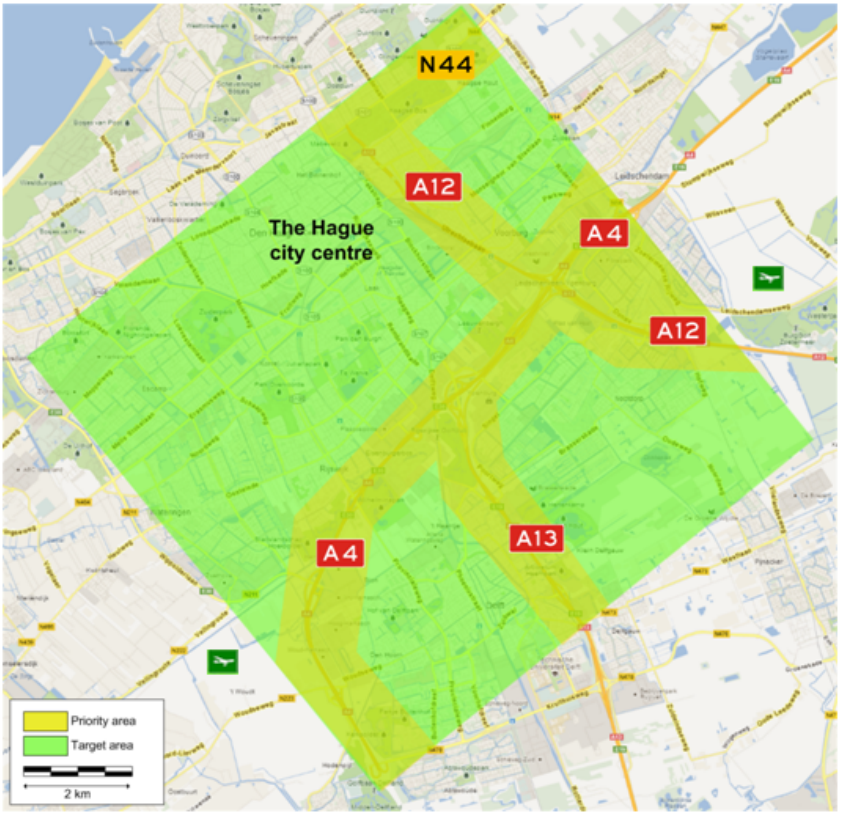

Figure 5.18: Landing Sites of the UAV

5.5 Operations and Logistic Concept

This section outlines the operations and logistic concept description of the final concept. This determines the system characteristics that are part of the design. Operational flow diagrams illustrate the support of the system. This section explains the maintenance, ground station and laser base station support systems.

5.5.1 Maintenance support system

The maintenance support system is illustrated in figure 5.19. Maintenance starts with either a need for urgent repair or a scheduled maintenance procedure. The ground station personnel checks if there is a UAV that is scheduled for maintenance. There are situations when there is an urgent need for maintenance, for example when there is a malfunction or if the UAV is damaged. Once maintenance is required for a UAV, the standby UAV on the ground is deployed to the target area instead of the one that is withdrawn for maintenance. This is performed to avoid or minimise temporary disruptions of the mission. A reparation or a scheduled maintenance of the malfunctioning part of the UAV is then carried out. Preflight tests are performed afterwards to assure high quality. The UAV is then put on standby, waiting for deployment when a need for maintenance arises among the UAVs in service.

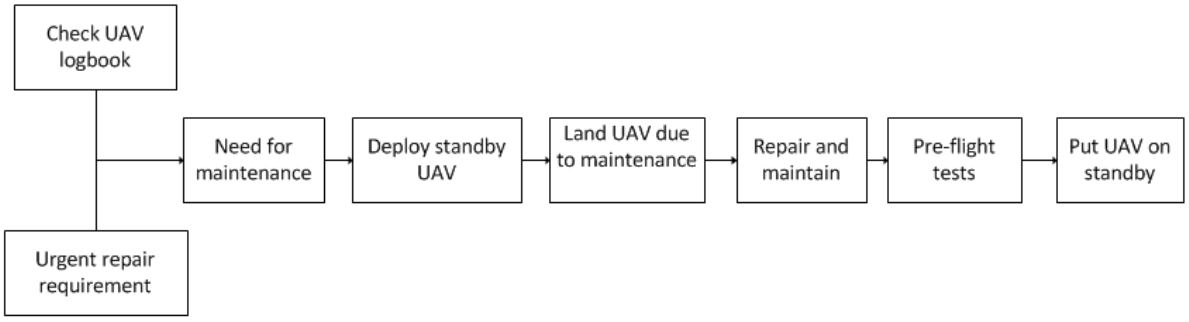

Figure 5.19: Operational flow diagram showing the maintenance support system.

The maintenance procedure scheduled for every three months. On-board mechanisms checked during the maintenance procedure are given in Table 5.12.

Table 5.12: Mechanisms checked during maintenance.

Subsystem	**Mechanisms to be checked**
Electric	• Battery(New battery every 5 months) • PMD sub-assemblies
Propulsion	• Propeller • Motor
Communication	• Sector antenna (Mechanical rotary)
Obstacle detection	• Camera lenses
Control	• Actuators • Autopilot

Structures and materials: The maintenance procedure emphases on the prevention of possible damage of the UAV. Composite materials are used for the UAV structure. Unlike metal structures, where fatigue crack initiations are the primary threat to the structural integrity, accidental damage is a critical threat for composites [137]. For damage inspection first visual inspection methods are employed. For detecting non visual damage tap testing, x ray and thermography techniques are used.

5.5.2 Mission control and operation station

The Mission control and operation station support system is illustrated in figure 5.20. This ground station works to support the UAV as it carries out its mission. When the UAV is following the preprogrammed flight path, the ground station personnel check the monitoring of the traffic network. If there is a traffic congestion, accident or other emergencies in the area of the preprogrammed flight path the UAV is made to loiter above that target area. If the target area is outside the preprogrammed flight path the UAV is controlled to this area. It is then ordered to loiter above it and to monitor and record the situation. The ground station personnel work in collaboration with the local police and emergency services for information regarding the accidents and emergencies outside the preprogrammed flight path.

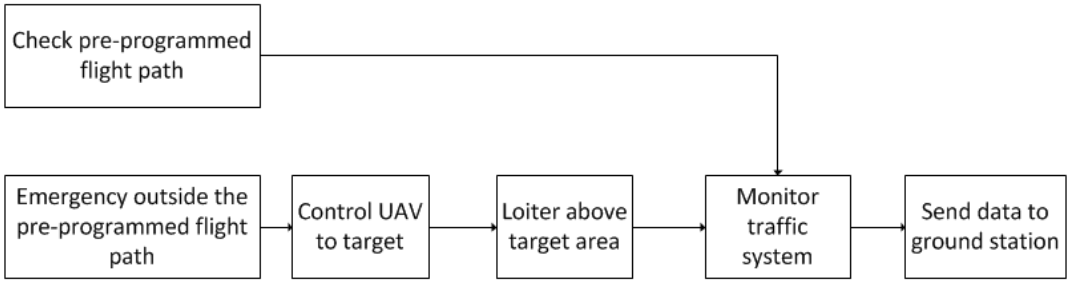

Figure 5.20: Operational flow diagram showing the ground station support system.

5.5.3 Laser base station

The laser base station support system is illustrated in figure 5.21. The laser base station supports the system by providing power to the UAV in several situations. The first situation is when an UAV is following the preprogrammed flight path. A check is done to determine if the UAV is in the range of the laser base station. The UAV is then accurately tracked. If there are no obstacles, the laser is beamed to the UAV to transfer power. In case the UAV has to deviate from the preprogrammed flight path to a certain target area, a check is performed if the UAV is in the range of a laser base station. The similar procedure is done as outlined for the first situation in order to transfer power.

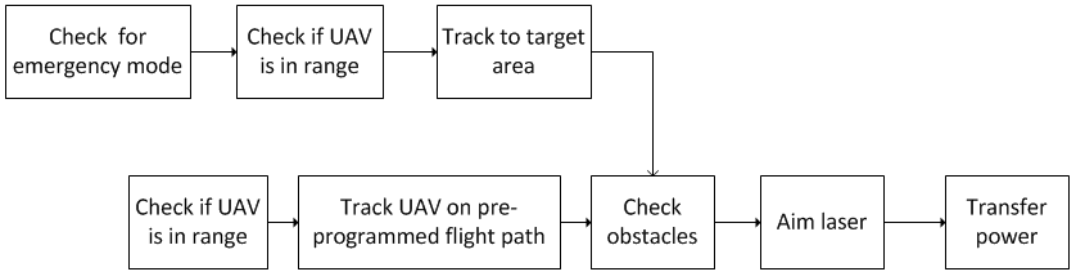

Figure 5.21: Operational flow diagram showing the laser base station support system.

5.5.4 Operations & Logistics diagram

The link of between the maintenance, ground station and laser base station support systems is presented in a flow diagram. The schematic representation of the operations and logistics concepts is shown in figure 5.22.

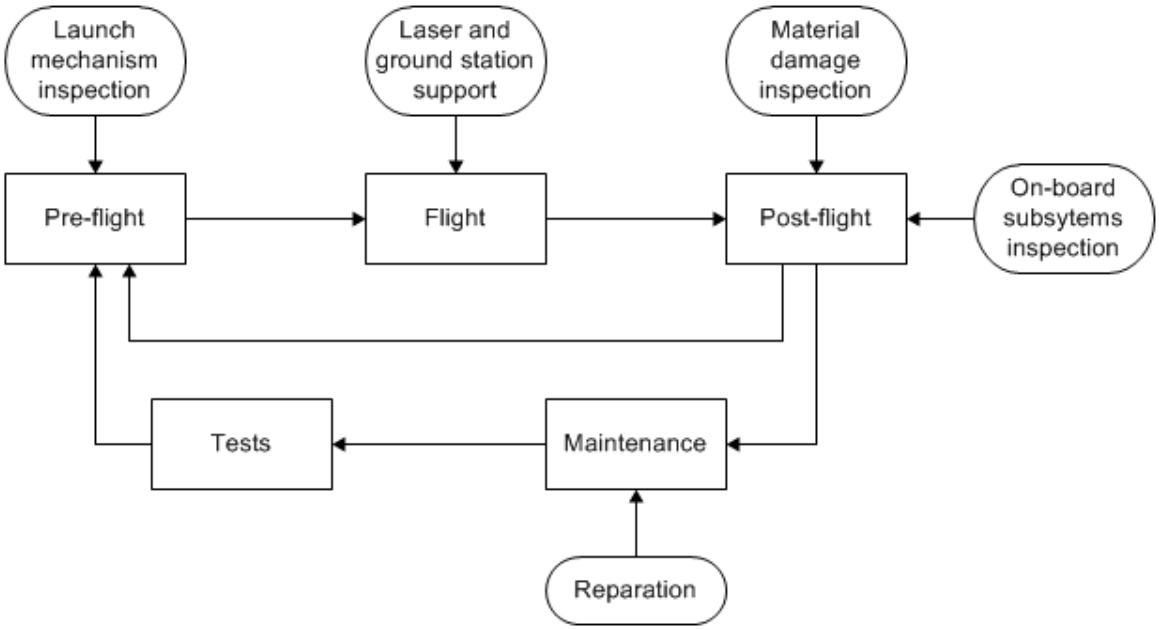

Figure 5.22: Operations and Logistics flow diagram.

CHAPTER 6

INTEGRATION OF SUBSYSTEMS

The previous chapters describe how the different subsystems are designed. This chapter explains how these subsystems are integrated into the whole system. First a brief overview of the entire system is given. The next section describes the different interactions between the subsystems with the help of an interface diagram. Finally this chapter is concluded with a feasibility analysis of the system.

6.1 System Overview

The system contains a set of subsystems working together to achieve the mission. This mission consists of monitoring an urban area. The monitoring is done by the aircraft which contains several subsystems. In order to keep functioning a power system regulates the power that is received from the ground. PV cells collect the power and the PMD system distributes it over the aircraft. Batteries on board store excess power for later use.

An aircraft control system is used to control the flight path of the UAV. In order to keep the aircraft along the required flight path an autopilot controls servo actuators, which in turn deflect a certain control surface.The required flight path commands are received through a communication system. This system has an omnidirectional antenna to pick up the radio waves and a receiver convert these to input signals that is understood by the autopilot. Data is sent back with a transmitter and the same omnidirectional antenna. An on board obstacle detection can also alter the flight path when an obstacle is in the way. It detects the obstacle and sends the data the the autopilot system which then determines the best course of action.

The propulsion system provides thrust to the UAV and achieves this with a combination of an electric motor and propeller. Most of the power that is sent to the aircraft is used by this system. The power that the aircraft requires, is sent from the laser base station. To make sure the laser hits the correct spot, a tracking system keeps track of the aircraft. For a rough estimation a GPS system on board is used for the initial tracking after which the laser is fired at a low power setting. When the PV cells on the aircraft detect the laser and it stays within acceptable margins, the power of the laser is increased and power is transferred. To aim the laser accurately a galvanometer, which determines the vertical angle, is mounted on top of a rotary stage, which determines the horizontal angle. The laser base station sends/receives data to/from the aircraft through a so called sector antenna. A receiver and transmitter is used to code/decode the radio waves. Finally this system is designed as a platform that can accommodate ten kilograms of payload. Power for the payload is supplied, as the other systems, through optical laser beaming.

6.2 Interaction Among Subsystems

The designed system is a complex systems with a lot of interactions. A risk is to design a subsystem that does not function in the system and introduce a possibility that the system does not function at all. In order to prevent this and make sure the subsystems are properly integrated, the interaction among the different subsystems have to be identified. To give a overview of the interaction a N^2 chart is used and this is displayed in figure 6.1. During the design process this is used to iterate the design.

Aerodynamics of the aircraft	Geometry and loads	Power Required, Flight Performance	Fuselage shape	Geometry of the wing, canard and vertical stabiliser		Flight performance	Flight performance	Flight performance	
Centre of gravity, MTOW	**Structure of the aircraft**	Assigned location	Assigned space, maximum temperature materials	Assigned space	Assigned space	Deployment Attachment Positions			
Power available, dimension propeller	Dimensions, weight	**Propulsion System**	Power consumption motor			Propeller Dimensions			
PV Cells Curvature Shape	PV Cells Integration, Weight	Power budget	**Electric Systems**	Power budget	Power budget		Power budget		
Dimensions control surfaces	Weight servos and flight computer		Power Required, Frequency and voltage used	**Aircraft Control Systems**	Data Bandwidth Required				
	Weight		Power Required, Frequency and voltage used		**Communication Systems**			Laser range, network specifications	
Take off and landing performance required	Dimensions Attachment Part Structure, load factors					**Deployment & Recovery System**			
	Weight, Volume in the fuselage		Power Required, Frequency and voltage used		Data Bandwidth Required		**Obstacle detection**		
			Area PV Cells		Data Bandwidth Required			**Tracking system & Laser power system**	
			Network specifications					Network specifications	**Network**

Figure 6.1: N^2 Chart of the laser base station

6.3 Risk Analysis

In order to identify and mitigate the risk involved in the project, a risk map is constructed wherein all functions from the functional flow diagram are ranked. This ranking is based on the probability of a functional failure and the impact that failure would have. Functions with a high probability of failure in combination with severe consequences are regarded as high risk functions. In the early design phase, a risk analysis was already performed and this analysis can be found in the mid term report [5]. However, at this stage the conceptual design is finished and a better understanding of the risk is obtained. Therefore the same risk map is updated to give a clear overview of the risk of this project at the current state. The risk map is shown in figure 6.2.

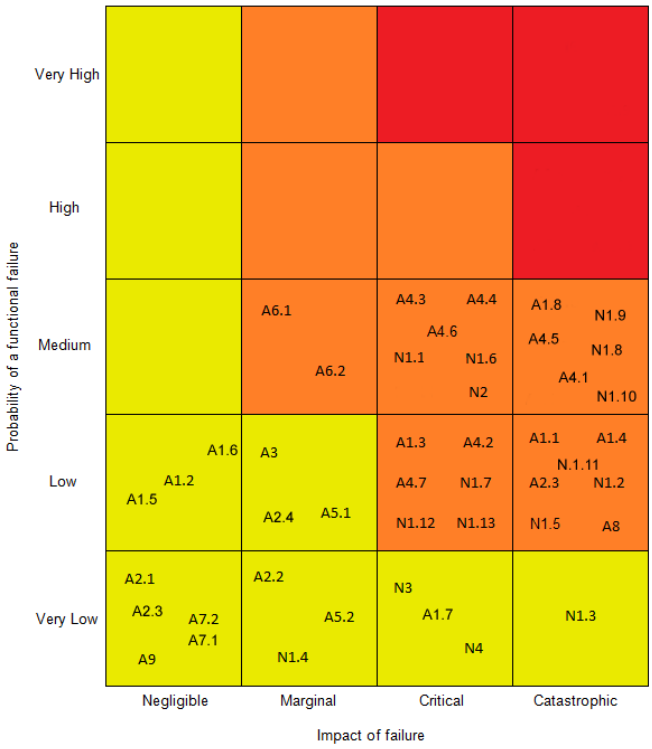

Figure 6.2: An updated risk map of the system.

The functions from the risk map which remained the same as in the mid term report are listed below without further explanation:

A1.1 Check Structural Integrity

A1.2 Charge Battery

A1.3 Check Energy

A1.4 Perform Visual Inspection

A2.1 Switch On

A2.2 Establish Communication

A3 Fly to Destination Area

A4.2 Check Battery Power

A4.3 Send Position, Attitude, Obstacles and Energy Need

A4.4 Receive Flight Path Data

A4.6 Collect Energy from PV cells

A4.7 Charge Batteries

A5.1 Switch On Payload

A6.1 Collect Data

A6.2 Send Data

A7.3 Recover from net and Switch Off

A8 Maintain Aircraft

A9 Store Aircraft

N1.1 Receive Aircraft Positions

N1.2 Judge Weather Conditions

N1.3 Check Requirement for Maintenance

N1.4 Obtain Target Area

N1.5 Identify Obstacles

N1.6 Obtain Need for Laser Power

N1.7 Assure Only One Aircraft Per Laser

N1.11 Transmit Laser Power

N1.12 Construct Flight Path

N1.13 Send Flight Path Data

N2 Receive Measurement Data

N3 Process Data

N4 Distribute Data

The functions from the risk map that are changed in the risk map or are recently added in the functional flow diagram are listed below with some explanation:

A1.5 Check Payload
Before launching the aircraft, the payload must be checked because without payload the aircraft cannot perform its mission, which is inconvenient for the customers. Before launch, the aircraft is thoroughly checked and thus the likelihood of missing the payload is low. In case the payload is skipped during the check, the aircraft can be recovered and the payload can still be installed and therefore the consequences are negligible.

A1.6 Check Control Surfaces
In order to keep the aircraft controllable, it must be ensured that the control surfaces function properly. Safety and redundancy measures are implemented in the control systems of the aircraft to mitigate risk. In case the control surfaces fail and the autopilot fails to solve the problem, it is always possible to control the aircraft manually. Since the aircraft is checked thoroughly before the mission, the likelihood of skipping this procedure is low and the applied fail safe measures result in a marginal impact.

A1.7 Check Motor and Propeller
The motor and propeller are essential for the aircraft as these parts provide the thrust for the aircraft to perform its mission. Therefore it is necessary to check before flight whether these parts are functioning properly. The propeller is designed such that it can cope with the recovery force when being recovered by a net and on top of that, the propeller can be folded making it impossible to get stuck in the net. The aircraft is checked every three months and during these checks, the motor is examined thoroughly. So the likelihood that either the propeller or the motor fails is very low. However the impact of failure is considered as critical, because if the aircraft is not recovered on time, it can fall out the sky when it loses its gliding ability completely.

A1.8 Check Cameras
The cameras are the eyes of the aircraft. Without cameras the aircraft is unable to detect and avoid obstacles. It is very important to keep the lenses of the cameras clean and undamaged, because the view of the cameras depend on the lenses. The likelihood of not checking the cameras properly is considered as medium because checking the inner parts of the camera and the lenses are very hard. The impact of failure is considered as catastrophic because obstacle detection cannot be done when the cameras are damaged.

A2.3 Deploy Winch
Before launching the aircraft, the winch, which is used to launch the aircraft needs to be deployed. Deploying the winch is a standard procedure and thus the likelihood that something goes wrong is very low. The consequence of something that goes wrong is negligible because safety protocols are used to keep operators away from danger spots near the winch.

A2.4 Launch Aircraft
For the launch it is essential that the alignment of the aircraft is correct during the ground run until the release to prevent the aircraft from spinning out of control. Also the timing of the release is essential because releasing it too early while the aircraft has not reached the required speed, insufficient lift is generated to keep the aircraft airborne. Releasing the aircraft too late is even worse because then the aircraft goes nose down and is eventually smashed on the ground being badly damaged. During the design phase it was shown that the winch is good quality and the likelihood of a failure in deployment is low. The consequence is considered as marginal because the worst that can happen is having a badly damaged aircraft and operators are not allowed to stay in the path of the launch so no injuries can occur.

A4.1 Determine Position, Attitude and Obstacles
This function was considered as a high risk because it was unsure whether it was possible to determine position, attitude and obstacles accurately enough. However, in this stage it is clear that this is possible since the autopilot is able to determine the position and attitude of the aircraft accurately enough for aircraft control and the obstacle detection cameras are able to detect any possible obstacles that the aircraft might encounter. Thus this function is re-ranked in the risk map.

A4.5 Control Aircraft
This function was considered a high risk because it was unsure how accurately the aircraft could be controlled. In this stage it is clear that the autopilot is able to control the aircraft with great accuracy and therefore this function is moved lower in the risk map.

A7.1 Deploy Net
The principle of deploying the net is same as deploying the winch and thus the ranking is the same as deploy winch.

A7.2 Fly Aircraft into the Net
The aircraft shall be guided into the net by the autopilot. The autopilot is able to control the aircraft with pinpoint accuracy and automatically makes wind correction. Thus the probability that the aircraft misses the net is considered very low. Also the consequences are considered

marginal because the net is located on a spot where, in case the aircraft misses the net, it will not fly into buildings and properties. It is also ensured that the aircraft has enough time and space to make another run.

N1.8 Track Aircraft Accurately In the midterm report this function was ranked at the top right corner of the risk map. However, in the later design phase it was proven that tracking the aircraft accurately enough was feasible using laser tracking and thus this function is moved down in the risk map as the probability of functional failure is lower. In the detail design phase the risk of this function might be even lower depending on results from experimental tests.

N1.9 Assure Clear Line of Sight Same as the previous function it is shown that assuring a clear line of sight can be done with much less risk and therefore this function is also moved down on the risk map.

N1.10 Assure Laser Extended Path is Clear of Obstacles The same reasoning as the previous function also holds for this function.

6.4 Feasibility Analysis

In the early stage of the project it was determined that technology wise it is feasible to have an aircraft fly continuously while being powered by optical beaming with lasers. In the design phase most required subsystems could be designed without any major problems. A big challenge is the energy transfer by optical beaming with laser. The laser must be powerful enough to provide the UAV enough power to perform its mission while it may not be harmful to citizen, air traffic and animals. A difficulty that was encountered during the design phase was laser deflection when the laser beam hits the PV cells at a too large angle. This difficulty prevents the aircraft to be beamed continuously and as result, back up batteries must be carried by the aircraft.

Another step that has to be taken is to get assent from authorities. Since this is a new concept, it does not fall under the existing rules and regulations regarding to aviation authorities and laser regulations. Despite the fact that it was shown during the design phase that this concept could be implemented safely, extensive testing is required before actual taking it into use. Before the start of the detail design, a set of requirements were set up. Having the subsystems and eventually the concept designed, the requirements will be checked whether these are met or not. In case if a requirement is not met, an explanation and possible solution is given. These requirements are put into a requirements compliance matrix, which can be found in Appendix A.

CHAPTER 7

SUSTAINABILITY

Sustainability is becoming more important in aerospace design processes due to the depletion of fossil energy sources. By reducing production and operational energy needs and by using power from sun, water or wind the impact on the environment can be minimised. This chapter proposes solutions to the sustainable problem and describes several parts of the system with the scope of green energy, such as bio composites and recyclability of the UAV. Multiple solutions of powering the laser are analysed. To conclude this chapter, a life cycle analysis is made in order to estimate the total CO_2 produced by the system.

7.1 Bio composites

While normal UAVs use metals like aluminium due to the low cost and low weight, this project group decided to took into composites and more specific, natural composites. Aluminium can be easily manufactured into a certain shape and has good structural properties. The project requirements specify no upper limit for costs, thus the main disadvantage of aluminium can be eliminated, namely the environmental impact of the manufacturing of the metal. This disadvantage is eliminated by implementing bio composites which are analysed in this section by considering the characteristics, the advantages and the disadvantages.

7.1.1 Characteristics of Bio Composites

Bio composites are made in the same way as general composites by using a reinforcement and a matrix, also called the resin. Bio composites use natural fibers such as wood fiber, jute or flax. The matrix is replaced by a sustainable resin. The Dutch company GreenGran produces durable composites and moreover, temperature resistant composites. When the material can handle higher temperatures, the insulation layer between the PV cells and the skin can be thinner, thus decreasing the mass of the aeroplane.

7.1.2 Advantages and Characteristics of Bio Composites

Bio composites can be grown and therefore they will not deplete earth's resources. The only thing that is needed is farmland and energy from the sun and the fibers are processed in the same way as non-natural fibers. The resin that is used by GreenGran is polypropylene (PP) which can be easily recycled and can thus be extracted from recycled sources. The composite has high stiffness and strength with average impact strength [21].

7.1.3 Disadvantages and limitations of Bio Composites

The main limitation of using bio composites is the low resistance to heat. Composites are bad heat conductors and therefore local heating can occur which results in melting of the resin and possible disintegration of the composite. This failure does have catastrophic results in the form of a crash, thus high temperatures must be avoided at all times. The maximum temperature of the material is 156 °C while the temperature of the PV cells will be higher. A layer of a few millimetres of insulation of sustainable glass wool [138] is applied to cope with this limitation.

7.1.4 Recyclability of Bio Composites

As mentioned before, the polypropylene can be recycled. The remaining layers can be shredded and used for the growth of new plants and therefore complete the circle.

7.2 Recyclability and Environmental Impact of Hazardous Materials

To reduce the impact on the environment, as much of the UAVs hazardous materials have to be recycled. Two parts of the UAV are difficult to recycle, the battery and the PV cell. These parts are analysed in this section.

7.2.1 Hazardous integrated materials in the system

In contradiction to the composites, the electric system houses hazardous materials in order for the system to operate. These materials include the toxic arsenic and lithium, which is difficult to recycle. These materials are analysed and the best solution with respect to human and environmental safety is proposed.

Lithium from the batteries

Lithium is a light and common element in the earths crust, although it does not occur in its elemental form due to its high reactivity. Lithium is mined from different types of minerals of which the most reserves are located in South America and Australia. Lithium mining is considered relatively safe, the last two decades no fatalities occurred in Australian lithium mines [139].

The increasing market for lithium in mobile device batteries and car batteries has tripled the price of the element from 2000 to 2012 [140]. Due to the increase in price, recycling of devices that contain lithium will be increasingly economical feasible. Although the recycling of lithium has yet be become cheaper than mining of new lithium, economists foresee this happening in the future [141]. For now, governments have to support companies that take effort in recycling lithium ion batteries. Such a company is Toxco located in the USA, which has already received multi million grands from the US government [142].

Recyclability of Gallium Arsenide PV cells

Gallium arsenide (GaAs) is a crystal constructed out of the rare element gallium and the highly toxic arsenic. Gallium reserves exceed one million tonnes [143], but are still scarce, compared to other metals. Due to the small amount of the element on earth, a sustainable method of recycling GaAs is needed. Such a method has yet to be found. Nowadays, gallium is mainly produced as a side product of aluminium mining, therefore it does not inflict direct damage to the environment [144]. With the rise in the use of semiconductors the gallium reserves can be easily depleted.

Arsenic is a metalloid with great properties with respect to semi conductance. Like gallium, it is produced as a side product, namely by the purification of copper. One of the risks of handling arsenic is the high toxicity. Precautions have to be taken into account in order to mitigate the risks involved, including when producing GaAs.

Although arsenic is very toxic, the GaAs crystal is stable and only when it is ground to very small pieces can it be harmful to the human body, but when GaAs is handled with care it maintains its structure.

7.3 Sustainable Options to Power Grid

By powering the UAV with laser power beaming, the UAV will have zero emissions. Theoretically this is not true when the laser is powered by fossil fuels. To provide a system that is as green as possible, sustainable power options are analysed in this section. Of course the main reason that sustainable options are considered is the inevitable depletion of fossil fuels. To ensure the operation of our system in the future a sustainable energy source has to be selected.

7.3.1 Common Industrial Energy Provision

Most power is generated by using burning fossil fuels, due to the low cost of coal and fossil fuel power stations. The two main fuels are coal and the slightly cleaner natural gas. The amount of CO_2 emissions from black coal and natural gas are 94.6 $g \cdot MJ^{-1}$ and 56.1 $g \cdot MJ^{-1}$ respectively. Besides the amount of emitted CO_2, other harmful compounds such as SO_2, NO_x and CO are released into the air, which can impose health risks [145].

7.3.2 Alternatives in Providing Energy

Several green alternatives exists in power provision. The main methods are analysed, which are solar energy, hydropower and wind energy. Even these sustainable alternatives emit small amounts of carbon dioxide because of production and maintenance. Each alternative is concluded with these values.

Analysis of Solar Energy in the Netherlands

Solar energy can be used to power the UAV. By generating more energy in the day and delivering that back to the grid, the method can deliver almost emission free power. The disadvantage of using solar panels in the Netherlands is the low power per unit area. On average 2.81 $kWh \cdot m^{-2} \cdot day^{-1}$ [146], which is too low to be efficient. The CO_2 emission of solar energy is 10.6 $g \cdot MJ^{-1}$ [147].

Imported Hydropower

Another green substitute of power from coal is using the energy of falling water. In fact, Norway's electric energy production is almost fully hydroelectric, therefore the excess energy can be imported to power the UAV without large emissions. Hydropower has the lowest emission of carbon dioxide per unit energy, namely 1.5 $g \cdot MJ^{-1}$ [147].

Wind Energy in the Netherlands

Wind energy in the Netherlands has great potential due to the high wind speeds in the coastal areas. A wind turbine in the Netherlands operates at optimum wind speeds 25% of the time [148], therefore a 3 MW turbine delivers on average 0.75 MW. The CO_2 emission of a wind turbine is 2.1 $g \cdot MJ^{-1}$ [147].

7.4 Life cycle Analysis of the System

In order to make an estimation about the system's produced carbon dioxide and end-of-life (EOL) recyclability rate, the section is divided into materials, transport, operations and end-of-life analysis. Hazardous materials are not taken into account as they are covered in the previous sections.

7.4.1 Materials

As explained in the previous chapter, the UAV is mostly made out of bio composites which contribute nothing to very little to the emission of carbon dioxide, other greenhouse gasses or poisonous gas. The materials of the subsections are analysed with respect to their emissions. The recycling of 1 kg of plastics (including PP) emits 3.5 kg of carbon dioxide [149]. Carbon fibres emit 5.8 $(kgCO_2) \cdot kg^{-1}$ [150] while the natural fibres have a low emission of 1.7 $(kgCO_2) \cdot kg^{-1}$ due to their natural growth. The emissions of metals varies, with steel emitting 1.3 $(kgCO_2) \cdot kg^{-1}$, copper and nickel with an embodied energy of 2.6 $(kgCO_2) \cdot kg^{-1}$ and aluminium emitting 8.2 $(kgCO_2) \cdot kg^{-1}$. The PV cells have an embodied energy of 242 $(kgCO_2) \cdot m^{-2} = 215$ $(kgCO_2) \cdot kg^{-1}$, the glass wool insulation emissions are 1.35 $(kgCO_2) \cdot kg^{-1}$ and the lithium ion batteries have a high specific emission of 12.5 $(kgCO_2) \cdot kg^{-1}$ [151]. An overview of the embodied energy is presented in table 7.1 where can be seen that the total emission of the raw materials of one UAV is 330 kg CO_2.

Table 7.1: Emission of carbon dioxide for one UAV per material. *(Based on the estimate that the remaining materials are electronic chips.)

Material	**Material mass** [kg]	**Spec. Emission** [$(kgCO_2) \cdot kg^{-}1$]	**Emission** [$(kgCO_2)$]
Plastics	8.17	3.5	28.6
Carbon fibers	3.55	5.8	20.6
Li-ion	3.51	12.5	43.9
Nat. fibers	2.91	1.7	4.95
PV cells	1.05	215	225
Copper	0.7	2.6	1.82
Steel	0.56	1.3	0.728
Aluminium	0.273	8.2	3.87
Glass wool	0.231	1.35	0.311
Nickel	0.158	2.6	0.410
Others	0.063	5*	0.315
Total	**21.2**		**330**

7.4.2 Transport

Transportation by truck burns diesel fuel and therefore adds to the emission of CO_2. The total transportation of the UAV has thus to be estimated and multiplied with the values from table 7.2 [152].

Table 7.2: Emission of gas for combinations of distance and truck mass.

	Short distance (< 150 km)		**Long distance (> 150 km)**	
Truck weight [Mg]	$(gCO_2) \cdot kg^{-1}km^{-1}$	$(gNO_x) \cdot kg^{-1}km^{-1}$	$(gCO_2) \cdot kg^{-1}km^{-1}$	$(gNO_x) \cdot kg^{-1}km^{-1}$
3.5 - 10	0.481	$3.39 \cdot 10^{-3}$	-	-
10 - 20	0.297	$2.16 \cdot 10^{-3}$	-	-
> 20	0.132	$0.930 \cdot 10^{-3}$	0.124	$0.860 \cdot 10^{-3}$

Most of the materials come from the GreenGran factory which is located in the Netherlands, therefore transportation emissions are minimised. The electric system is also bought in the Netherlands, limiting the transport to 150 km. The motor and propeller come from the USA. By buying the batteries, the PV cell and the other components in China, costs can be minimised. The distances over sea from the USA and China to Rotterdam are 6,000 km and 20,000 respectively. For transport over sea the emission equals $63.4(gCO_2) \cdot tonne^{-1} \cdot km^{-1}$. In table 7.3 the emissions due to transport are summarised and the released carbon dioxide due to transportation is 11.9 kg.

Table 7.3: Emission of carbon dioxide for transport of one UAV per material.

From	**Dist.** [km]	**Mass** [kg]	$(kgCO_2) \cdot kg^{-1} \cdot km^{-1}$	**Emission** [$kgCO_2$]
Netherlands by truck	150	12.1	$3.39 \cdot 10^{-3}$	0.509
China by ship	$20 \cdot 10^3$	8.61	$63.4 \cdot 10^{-6}$	10.9
USA by ship	$8.0 \cdot 10^3$	0.456	$63.4 \cdot 10^{-6}$	0.507
Total		21.2		11.9

7.4.3 Operations

In the operations part the energy need is the important part, other factors are thus neglected. The UAV will be powered with wind energy when available. The energy consumption of the laser is estimated to

be $7.52 \cdot 10^4$ kWh which equals $2.71 \cdot 10^5$ MJ. The emitted CO_2 due to energy consumption for one UAV and the lasers is then 569 kg.

7.4.4 End-of-life analysis

In the previous sections the recyclability is already roughly considered. Now the system is divided in its core materials, the mass percent recyclability can be calculated. Almost every part can be recycled except for some parts of the motor, the batteries and the PV cell. The recyclability rate for each part is presented in table 7.4. As can be seen the structure can fully be recycled. Parts which are mainly made out of materials can be re-used. Parts with electronic parts are considered less recyclable and are have thus lower ratios.

Table 7.4: Estimates on recyclabilities of the systems of one UAV. Note: batteries and GaAs cells can be recycled but have to be shipped and the process is costly, thus the recyclability ratio is set to zero.

Part	**Mass** [kg]	**Recyclability ratio** [-]	**Waste** [kg]
Structure	12.9	1.0	0
Batteries	3.9	0.0	3.9
PV cell	1.08	0.0	1.08
Electric system	0.70	1.0	0
Communications	0.70	1.0	0
Obstacle detection	0.724	0.7	0.217
Flight control	0.588	1.0	0
Other parts	0.405	0.0	0.405
Total	21.2		5.60

From the table can be seen that almost 75% of the UAV can be recycled under the assumptions that the electronics, batteries and PV cells are not recyclable.

7.5 Conclusions

This chapter described the sustainability of the system in various ways as carbon dioxide emission and recyclability. Carbon dioxide is mostly produced due to operations. The recyclability of the UAV is around 75% due to the use of bio composites. Further analysis has to be done on manufacturing of the UAV and emission and waste that are related to those activities.

CHAPTER 8

COST ANALYSIS

This chapter presents an overview of the costs related to this project. Design, manufacturing and operational costs are taken into account. When the total cost is known, a market analysis is done in order to compare the system with competitive systems. The chapter is concluded by an analysis of return of investment and indicates how profit can be generated while using of exploiting this system.

8.1 Cost Analysis of the System

The design and manufacturing costs are investigated in this section as well as the initial and operational costs of all the subsystems. These costs are necessary to provide a solid base for comparison against other systems which will be done in the market analysis.

8.1.1 Design and Manufacturing Costs

The design and manufacturing costs are estimated on an salary of EUR 50 per hour per student-engineer. The system has to be fulle operational in 2014, thus the total design costs are estimated on 40 weeks of work of nine people working five days a week. The calculation of design cost can be seen from equation 8.1.

$$\begin{aligned} \text{Cost}_{design} &= \text{Number of students} \cdot \text{Weeks} \cdot \text{Days in week} \cdot \text{Hours} \cdot \text{Salary} \\ \text{Cost}_{design} &= 9 \cdot 40 \cdot 5 \cdot 8 \cdot 50 = 720,000 \text{ EUR} \end{aligned} \tag{8.1}$$

The manufacturing cost is estimated to be EUR 1,700 per UAV. For the whole system this adds up to EUR 5,100.

8.1.2 Cost of One UAV

The costs of a single laser powered UAV are described and summarised in this section. First a descriptive list of the subsystems is given and thereafter the results are presented in table 8.1.

Manufacturing Costs
The costs of manufacturing are estimated to be EUR 1,700. This includes the workers and the materials such as adhesives and bolts.

Structures
The structure is the combination of the two composites, the natural composite and the carbon fiber one. The costs of carbon fiber are high, but due to the small structure few carbon fiber is needed. Included in the operational cost is the hiring of an engineer who checks the UAV when in maintenance.

Motor
The motor will be shipped from the USA and will be replaced every six months.

Propeller
The propeller will be made from nylon and glass fiber and will add little to the total cost.

Electric System
The electric system consists of the battery and the infrastructure. Due to the low amount of batteries needed, the costs will be relatively low.

Flight Control
This includes the control surfaces and the autopilot, The autopilot will be a Kestrel program.

Communication
Communications are done by antennas and will be maintained by a communications engineer.

Deployment
Costs related to deployment are mainly due to the use of a winch and the costs per take off.

Landing
Landing costs are the cost of the net which will catch the UAV.

Obstacle Detection
Obstacle detection costs are mainly that of the cameras.

Laser
The laser cost is the operational cost for power from the electric grid.

PV Cells
The PV cell system is the subsystem that collects the energy. The costs consist out of the purchase of high quality PV cells.

Table 8.1: Total cost estimate of one UAV.

Subsystem	**Initial Cost** [EUR]	**Operational Cost** [EUR/year]
Manufacturing costs	1,700	
Structures	500	16,667
Electric Motor	82	738
Propeller	30	
Batteries	160	960
Electric system	1,290	
Flight control	10,160	16,667
Communication	12,000	5,760
Deployment	11,667	3,324
Landing	1,400	
Obstacle Detection	47,780	
Laser		6,000
PV cells	15,000	
Total	**101,769**	**50,115**

8.1.3 Cost of One Laser Base Station

In the system over The Hague are two kinds of laser base stations. Two with a single laser and two with two lasers. These costs are listed in this section and summarised in table 8.2 and table 8.3.

Tracking and Aiming
The tracking and aiming system coordinates the laser such that it hits the UAV. The system consists out of several engines and rotors that have to be very accurate.

Laser
The power of the diode laser is 4.5 kW and the cost is estimated by EUR 50,000 per kW.

Laser Base Station
A laser base station is a building of EUR 250,000 where the laser, the cooling system and some electrical infrastructure is located. Like normal buildings, the laser base station has maintenance costs .

Table 8.2: Total cost estimate of one laser base station with one laser.

Subsystem	**Initial Cost** [EUR]	**Operational Cost** [EUR/year]
Tracking and Aiming	13,000	
Laser	225,000	
Laser Base Station	250,000	5,000
Total	**488,000**	**5,000**

Table 8.3: Total cost estimate of one laser base station with two lasers.

Subsystem	**Initial Cost** [EUR]	**Operational Cost** [EUR/year]
Tracking and Aiming	13,000	
Laser	450,000	
Laser Base Station	250,000	5,000
Total	**628,250**	**5,000**

8.1.4 Cost of the Ground Station

The costs of a ground station are estimated to be the same as a laser base station. This is initial EUR 250,000 and thereafter power and maintenance on the building of EUR 5,000 per year.

8.1.5 Total Costs of the System

The total initial and operational costs of the system for the Hague are summarised in table 8.4. The system includes two operating UAV, one UAV as reserve, four laser base stations with six lasers and one ground station. The operations are monitored by one pilot, one communications engineer and one structural engineer.

Table 8.4: Total costs of the system including three UAVs, four base stations and six 4.5 kW lasers.

Subsystem	**Initial Cost** [EUR]	**Operational Cost** [EUR/year]
Design costs	720,000	
Manufacturing costs	5,100	
Structures	1,500	50,000
Electric motor	246	6624
Propeller	90	
Batteries	480	960
Electric system	3,870	
Flight control	30,480	50,000
Communication	36,000	17,280
Deployment	35,000	9,972
Landing	4,200	
Obstacle Detection	143,340	
Tracking and Aiming	52,000	
Laser	1,350,000	18,000
PV cells	45,000	
Laser base station	1,000,000	20,000
Ground station	250,000	5,000
Total	**± 3,600,000**	**± 178,000**

8.2 Market Analysis

In order to investigate the economic feasibility of the system, other solutions with respect to monitoring have to be investigated. To to make the economic benefits of the system clear, advantages and disadvantages are traded off. Several other uses of the system are proposed in this subsection to increase the system's value.

8.2.1 Comparison of the System with respect to Equivalent Systems

The main competitors of the laser assisted UAV system are closed circuit television (CCTV) and using governmental patrol cars. These are included in the analysis of advantages and disadvantages of the system.

Advantages of the System

The main advantage of the system is the flexibility. While CCTV is fixed to certain roads, the UAV can move freely in the 10×10 km^2 and monitor each road and especially emergency sites and the potential traffic jams related to that.

The speed of 100 km $\cdot$ h^{-1} ensures fast arrival on emergencies sites with an maximum of just over 8 minutes from corner to corner of the target area. The UAV is much faster compared to a monitoring car that has to follow the road and can be hindered by the traffic jam. The UAV can provide overview imagery that only multiple, high mounted cameras can provide.

An other advantage of the system is the exposure of a city in the media. When the system is purchased and operating, the city will promote their positive attitude against technology. For cities that want to advertise them self as technological cities - For instance in the Netherlands: Delft, Eindhoven and Enschede - embracing of the system will gain them interest from other technological companies and people.

From a sustainable point of view, the system is considered more green than using patrol cars. The power required of the system is in the order of 10 to 20 kW, while cars use much more power. Governmental cars, like police cars, still use fossil fuels which are depleting. The UAV will be powered by green energy and consists out of bio composites, making them - apart from walking, biking or CCTV - the greenest solution for a mobile monitoring system. The same advantage therefore applies as for the technical exposure.

Disadvantages of the System

The disadvantage of the system is mainly the high costs related to the development, manufacturing and operation of the system. Where the initial cost of CCTV is high, the operational cost is low. Only the low energy cost and the monitoring. The UAV has both high initial and operational cost. The trade off that has to be made is that of speed and flexibility against costs.

Another problem with the system is that it is not proven for these requirements. Development, testing and certification all have to be done and this can take up several years. When a monitoring system is quickly needed, CCTV or car patrol will be chosen over the laser assisted UAV.

8.2.2 Other Uses of the System

Besides monitoring an urban area, other uses of the system can be investigated. This section will propose multiple different uses of the UAV in both monitoring and non-monitoring missions.

Forest monitoring and Disaster Prevention

Due to the fact that forests are not easily accessible by vehicles, monitoring from the sky can be advantageous. Wildlife tracking can be done by the UAV while it is being powered from the edges of the forest. Also wildfires can be easily detected by the use of thermal cameras. The risk of forest fire

can greatly be reduced. When the only mission of the UAV is monitoring the forest, the payload can be minimised and the distance between the laser and the UAV can be increased, making the area larger. Other uses of disaster prevention are monitoring dikes and dune areas where flooding can give severe problems.

Defense

When the payload of the UAV is used for defense purposes, it can be used to defend borders or camps. It can both be monitor of eliminate enemy targets. Because landing the UAV is unnecessary, their will be continuous surveillance above critical targets and appropriate action can be done at each moment in time.

Border control

When laser base stations are added to a border, the UAV can monitor the area continuously, making sure illegal crossing is prevented. With normal and thermal cameras, computers and human controllers can spot crossing people. This will minimise labour costs and reduces the changes of people getting through.

8.3 Return on Investment

For the return on investment (ROI) the costs per year for the system is calculated. To determine if the system is competitive with other systems a reference UAV is investigated and the costs are compared and reasons why the laser assisted UAV is more expensive are presented.

8.3.1 Cost of the system per year

An analysis of the costs per year is made with an estimated interest of 3% in order to determine the yearly cost. The present value (PV) is determined to make sure two series of payments are equal. From table 8.5 can be seen that five yearly payments of around EUR 950,000 can buy the system.

Table 8.5: Cost analysis for initial cost plus yearly payments in comparison with fixed yearly costs.

		Initial and yearly costs		**Fixed yearly fee**	
Year	**Date**	**Payment** [EUR]	**PV** [EUR]	**Payment** [EUR]	**PV** [EUR]
0	1-1-2014	3,855,160	3,855,160	957,424	957,424
1	1-1-2015	177,854	172,674	957,424	929,537
2	1-1-2016	177,854	167,645	957,424	902,464
3	1-1-2017	177,854	162,762	957,424	876,178
4	1-1-2018	177,854	158,021	957,424	850,658
Total			**4,516,261**		**4,516,261**

8.3.2 Cost Comparison to Other Systems

A main competitor with the laser assisted UAV is the Penguin B from UAV Factory [153]. This UAV is capable of carrying 10kg and flying at least 100 $\mathrm{km} \cdot \mathrm{h}^{-1}$, therefore it can be compared well against the laser UAV. The key characteristics of both UAV are presented in table 8.6.

Table 8.6: Comparison between a laser assisted UAV and a Penguin B. *(Note: infinite flight does not cover landing for maintenance procedures and bad weather conditions.)

		Laser Assisted UAV	**Penguin B**
Parameter	**Unit**	**Value**	**Value**
Maximum Take Off Weight	[kg]	31	21
Empty Weight	[kg]	21	10
Wing Span	[m]	3.1	2.2
Length	[m]	2.5	2.7
Wing Area	[m^2]	1.4	0.79
Powerplant	kW	1.7	1.8
Max Payload	kg	10	10
Endurance	h	∞*	20+
Cruise speed	[$m \cdot s^{-1}$]	28	22
Stall speed	[$m \cdot s^{-1}$]	17	13
$C_{L_{max}}$ (clean wing)	[-]	1.3	1.3
Initial cost one UAV	[EUR]	102,402	60,000
Cost per ground control unit	[EUR]	500,000	13,000
Estimated initial cost per system monitoring the Hague	[EUR]	$\pm$ 3,700,000	$\pm$ 266,000

The import difference between the UAVs is the endurance. While the Penguin B uses fuel which is the limiting factor in endurance, the laser assisted UAV will fly by laser power and thus does not need for refueling. In the report is simulated that concerns with respect to safety are unnecessary because the reflected laser power is lower than the maximum permissible exposure at all times.

The use of bio composites and other sustainable design choices result in a UAV that is more recyclable than others. The laser power is generated with wind and water energy, reducing the carbon dioxide emission. The choice for a composite factory in the Netherlands decreases the needed transportation. From the comparison in table 8.6 can be seen that the cruise speed of the Penguin B is lower, while a higher power is needed. This is mainly due to the higher maneuverability of the aeroplane, which is needless of our problem of monitoring the motorways.

The sustainability of the laser assisted system comes with a price. The initial cost of the system is higher due to the four needed base stations and the six lasers each with a cost of EUR 225,000. At the end of the project's lifetime, which is more than five years, the lasers can be sold, reducing the overall cost of the project because a positive cash flow is added at the end. The mean-time-to-failure for the laser array is over 10,000 hours [13]. When six lasers power two UAVs at 90% for five years, they are around 25% of their lifetime. When the value of the lasers is assumed to decrease linearly, each laser is still worth EUR 168,750. Decreasing the projects present value with EUR 873,391 and therefore reducing the fixed yearly fee with EUR 185,000.

To summarise the comparison with the Penguin B the main differences between the systems are presented. Although the Penguin B is less expensive, the laser assisted UAV has some unique selling points. The use of safe laser technology will ensure efficient power transfer compared to using fossil fuels. Moreover, the use laser power will draw positive attention to a city which wants to be profiled as a city that has a positive attitude against new technology. The sustainable aspects of the projects are meaningful due to the importance of environmental impact and the depletion of fossil fuels. These are the key selling points that other UAVs lack, creating a new market segment and ensuring the sales of the system for countless missions.

CHAPTER 9

FURTHER DESIGN STEPS

The implementation of the laser technologies within the UAV industries, improved the UAV to have a long endurance to stay airborne which gives a large range of applications to use the aircraft. This chapter gives an overview of the methodology used for further developments of the project. This methodology is explained by showing a workflow of the designated steps and these steps are further explained. Furthermore an estimation of the production time is presented by the means of a Gantt chart. Through the feedback of the designing team, improvements are implemented within the methodology.

9.1 Workflow Diagram

The design thesis project of a laser powered unmanned aerial vehicle (UAV) finishes with a conceptional design of the UAV and the base stations. Development of this design is very difficult and requires a lot of resources, therefore suitable funding is required to be found first. Finding an investor which could seem as a relatively easy job however, it is time consuming to find an investor to supply the project with the suitable fundings. Marketing and looking for investors is done simultaneously, this is performed to increase the efficiency of the time management. Once the funding and the buyers are assured, a location for the assembly and the production of the subsystems is selected. Furthermore a deserted location is chosen which is essential for the testing of the systems to be done safely and to prevent any safety hazards. After providing the suitable resources and working spaces for the project, a detailed analysis of the design is performed to each subsystem. The design of the aircraft is optimised to increase the payload of the UAV. The aerodynamic drag could be reduced by including fairings within the detailed design phase. Analysis of the canard and its interferences with the wing is performed in a wind tunnel test. The optimisation of the launch system is done by improving the aerodynamic shape of the railboard used to launch the UAV. Laser experts are provided to determine the variation of the laser power density with respect to the laser angles. The UAV structure is Optimised for weight and strength, also it is considered to increase the structure resistance to lighting strikes. New products and system subparts are being developed on a daily basis, so the use of these new developed products has to be considered as in lithium batteries with lower specific capacity which could save up to half the weight currently used. By developing and optimising the UAV design, a new detailed design is presented to be produced. The production process begins by inquiring the different parts for the subsystems from the market then assembled in the factory by professionals to produce the first prototype. The first prototype model goes through a large sequence of tests to validate the functionality of each subsystem. The tracking system is tested to measure the angular deviations of the laser with the accuracy required. The launching and landing net system are tested to ensure the safety of the UAV. Furthermore the UAV performance is tested. This test sequence should ensure the customer of the product functionality and safety. The result of these tests are used in optimising the prototype resulting in a final design of the UAV and the station systems ready to be produced. The production of the final product is then performed and distributed to the customers. The production and distribution of the final product could be considered as a final step, however there is always some feedback or specifications from the customers to provide them with nearly the same product but with different mission capabilities. These specifications are given to the designing division of the subsystems at the factory to buy the appropriate subsystem parts and goes through the same cycle of production again. A summarise of the production plan is shown in the figure 9.1. The first commercial prototype should be ready before the end of 2014 to sell as it can be seen in the figure 9.2.

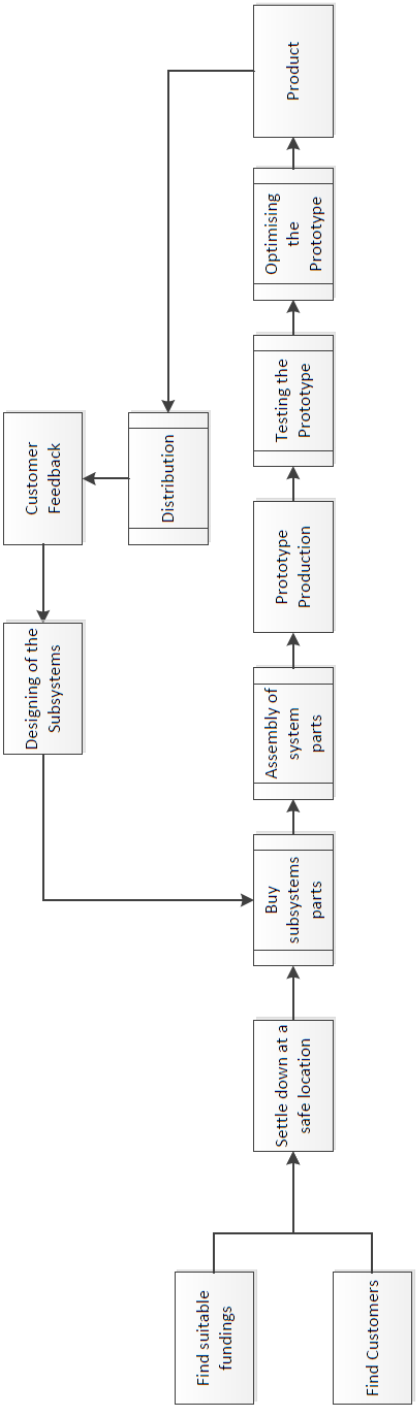

Figure 9.1: Workflow Diagram

9.2 Gantt Chart

The post-DSE activities are shown in the gantt chart in figure 9.2. A detailed design of the wing and fuselage will be done after the DSE for approximately three months. The number, design and location

of ribs, spars, sections and other structural elements will be determined. A flight simulator will also be programmed to simulate the UAV in combination with the laser system. The flight simulator will help with visualising the manoeuvrability and laser tracking of the UAV while performing a mission above the Hague. The winch being designed by Skylaunch will also be provided during the period of the detailed design [122]. After the project is funded and customers are found the UAV and laser systems can be assembled, tested and improved for approximately one year.

Once the first product is released at the end of 2014, the customers will have feedback with respect to the results of the performed mission. The subsystems can be improved and replaced according to this feedback. Improving the subsystems will also require further research on new technologies which are being developed over the life time. The systems will be tested and distributed afterwards. This will be repeated until the end of the mission.

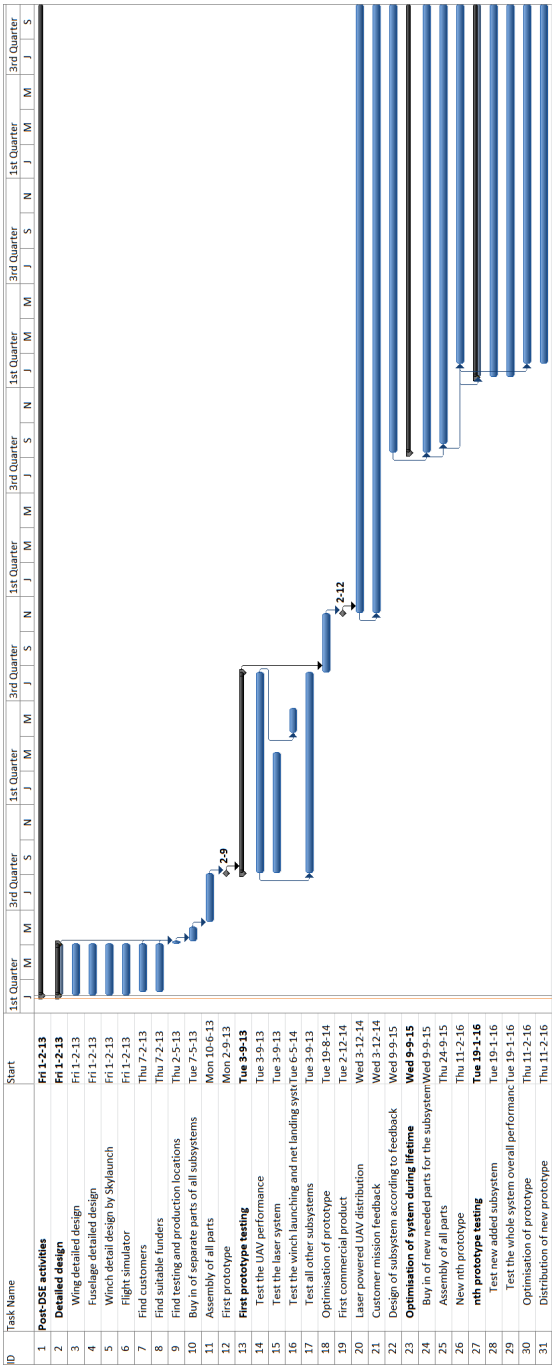

ID	Task Name	Start
1	**Post-DSE activities**	**Fri 1-2-13**
2	**Detailed design**	**Fri 1-2-13**
3	Wing detailed design	Fri 1-2-13
4	Fuselage detailed design	Fri 1-2-13
5	Winch detail design by Skylaunch	Fri 1-2-13
6	Flight simulator	Fri 1-2-13
7	Find customers	Thu 7-2-13
8	Find suitable funders	Thu 7-2-13
9	Find testing and production locations	Thu 2-5-13
10	Buy in of separate parts of all subsystems	Tue 7-5-13
11	Assembly of all parts	Mon 10-6-13
12	First prototype	Mon 2-9-13
13	**First prototype testing**	**Tue 3-9-13**
14	Test the UAV performance	Tue 3-9-13
15	Test the laser system	Tue 3-9-13
16	Test the winch launching and net landing syst	Tue 6-5-14
17	Test all other subsystems	Tue 3-9-13
18	Optimisation of prototype	Tue 19-8-14
19	First commercial product	Tue 2-12-14
20	Laser powered UAV distribution	Wed 3-12-14
21	Customer mission feedback	Wed 3-12-14
22	Design of subsystem according to feedback	Wed 9-9-15
23	**Optimisation of system during lifetime**	**Wed 9-9-15**
24	Buy in of new needed parts for the subsystem	Wed 9-9-15
25	Assembly of all parts	Thu 24-9-15
26	New nth prototype	Thu 11-2-16
27	**nth prototype testing**	**Tue 19-1-16**
28	Test new added subsystem	Tue 19-1-16
29	Test the whole system overall performanc	Tue 19-1-16
30	Optimisation of prototype	Thu 11-2-16
31	Distribution of new prototype	Thu 11-2-16

Figure 9.2: Gantt chart of the activities after the DSE

CHAPTER 10

CONCLUSIONS AND RECOMMENDATIONS

Conclusions

In order to monitor the motorway network of The Hague, a system is designed consisting of four laser base stations with a total of six lasers, three UAVs, two landing sites and one ground control station. The UAVs are able to carry 10 kg payload and fly at a velocity of 100 km h^{-1}. The laser base stations cover an area of 10 x 10 km. Within this area, a flight path is constructed above the motorways at an altitude of 230 m. With two airborne UAVs, the monitoring interval is 12.5 minutes.

Gallium Arsenide (GaAs) diode lasers with an output of 4.5 kW are used to transfer power to the aircraft. Photovoltaic (PV) cells on the aircraft convert the laser energy to electric power at an efficiency of 56%. These lasers operate at a wavelength of 830 nm, which is invisible to the human eye. A simulation model shows that the lasers can be aimed at the PV cells within a margin of 6 cm. This is established using measurements on the PV cells which are directly communicated to the laser controller. The laser beam itself is controlled with a rotary stage and a galvanometer.

PV cells reflect a part of the laser beam, depending on the incidence angle. By applying curvature to the PV cells, the maximum exposure of reflected laser power on the ground is 1.0 W m^{-2}. This is within the safety limit of 6.1 W m^{-2}. Obstacles that might fly through the laser beam are detected by a radar system and thermal cameras on the ground. When this occurs, the laser is switched off immediately.

For the design of the UAVs, a canard configuration is chosen. This configuration allows placement of the PV cells between the main wing and the canard. This configuration is also beneficial because of the lower induced drag compared to a conventional configuration. The design is optimised during multiple iterations. The aircraft is controlled with an autopilot and servo-actuators. The structure of the wings consists of a carbon fibre composite and is designed for a load factor of 4. For the fuselage, bio-composites are used which are 100% recyclable.

To save weight, the UAVs do not have a landing gear. The aircraft is deployed by a winch. During the ground run, the UAV is supported by a rail board. Instead of a conventional landing, the aircraft is caught from the sky with a net. Cable transducers control the deceleration of the UAV.

Thrust is provided by a foldable push-propeller. This prevents interference with cameras in the nose. A foldable propeller will not get stuck in the net. Using the program PropCalc, a propeller is selected which operates at 4700 RPM providing a thrust of 37 N. This propeller is driven by an electric motor. The electric system provides power to all subsystems and has a Lithium-Ion battery which allows for 30 minutes of flight. Due to the limited number of cycles, this battery has to be replaced every five months.

The UAVs are able to detect obstacles using cameras. With a thermal camera and an optical flow algorithm, birds can be detected and avoided. Continuous radio communication provides a data rate of 2 Mb·s^{-1}. This is required for the tracking system, flight control and payload data.

The complete system has an initial cost of approximately 3.7 million EUR and a yearly operational cost of 178.000 EUR. Compared to other UAVs in the market, this system is more expensive. However, these UAVs can operate continuously for months and are sustainable.

The system can be operational at the end of 2014. Further steps include a detailed design and extensive testing of the prototype.

Recommendations

This report discusses the preliminary design phase. For the detailed design phase recommendations can be taken into account.

A simulation has shown that the aiming of the laser can be done in a safe manner, however, an experimental test is still required to fully prove this. The test should determine if the laser is constantly aimed at the PV cells and measure the intensity of the reflections on the ground. If the requirements are not met, then a redesign of this part of the system is necessary.

Further analysis is recommended on the design of the UAVs. Wind tunnel tests can be performed to optimise the overall performance of the aircraft by determining the interaction of the canard on the wing.

Different materials can be analysed in order to optimise the structure for weight and strength. Load tests can then be performed to determine the ultimate strength of the aircraft structure. Furthermore it is recommended to design the structure such that it is able to cope with lightning strikes.

Instead of using Lithium-Ion batteries it is recommended to opt for Lithium-Sulphur batteries in the future, when the technology is improved. The main problem with these batteries at the moment is that they have a very low number of cycles compared to Lithium-Ion batteries. The power density, however, is considerably higher.

When considering the maximum exposure of laser light, the laser power can be increased by a factor of 6. This increase in power could translate in an increase in payload on the aircraft. This would imply a redesign for instance, as an increased aircraft weight increases the required lift which in turn means a higher wing surface.

CHAPTER 11

BIBLIOGRAPHY

[1] "Certification Specifications for Normal, Utility, Aerobatic, and Commuter Category Aeroplanes CS-23 Amendment 3 20 July 2012," *European Aviation Safety Agency (EASA)*.

[2] "Helios Prototype: The forerunner of 21st century solar-powered ätmospheric satellites;" *NASA*, [http://www.nasa.gov/centers/dryden/news/FactSheets/FS-068-DFRC.html, Accessed on 20 January 2012.].

[3] "Beamed Laser Power For UAVs," *NASA*, [http://www.nasa.gov/centers/dryden/news/FactSheets/FS-087-DFRC.html, Accessed on 20 January 2012.].

[4] "LaserMotive Company," [www.lasermotive.com, Accessed on 20 January 2012.].

[5] Goossens, L., van Holstein, R., Liu, F., Matema, S., Negem, T., Peeters, P., Reitsma, J., Slinger, B., and Uzumcu, S., "Mid Term Report: Laser Assisted UAV," *TU Delft, Faculty of Aerospace Engineering*.

[6] "Model 8360K Optical Scanner Datasheet," *Cambridge Technology*, [http://www.camtech.com/index.php?option=com_content&view=article&id=104&Itemid=78, Accessed on 21 January 2013.].

[7] "NanoRotator 360 Stage Datasheet," *Thorlabs*, [http://thorlabs.com/newgrouppage9.cfm?objectgroup_id=1064, Accessed on 21 January 2013.].

[8] Erteza, A., "Boresighting a Gaussian beam on a specular target point: a method using conical scan," *Applied Optics*, Vol. 15, No. 3, March 1976.

[9] "Kestrel Autopilot System," *Procerus Technologies*, [http://www.procerusuav.com/Downloads/DataSheets/Kestrel_2.4.pdf, Accessed on 16 January 2013].

[10] Widlok, M., "Advanced methods of galvoscanner position control with integrated power supply module," *University of Science and Technology in Cracow*.

[11] Baluta, G. and Coteata, M., "Precision microstepping system for bipolar stepper motor control," *Electrical Machines and Power Electronics, 2007. ACEMP '07. International Aegean Conference on*, sept. 2007, pp. 291 –296.

[12] Huy, H. L., Brunelle, P., and Sybille, G., "Design and implementation of a versatile stepper motor model for simulinks SimPowerSystems," *Industrial Electronics, 2008. ISIE 2008. IEEE International Symposium on*, 30 2008-july 2 2008, pp. 437 –442.

[13] "1.6 mm Ony High Power Array," *Coherent*, [http://www.coherent.com/products/?1576/1-6-mm-Onyx-MCCP-High-Power-Array, Accessed on 13 January 2012].

[14] Griffiths, D., *Introduction to electrodynamics*, Prentice Hall, 3rd ed., 1999.

[15] Tomasi, C., "Weak absorption by atmospheric water vapour in the visible and near-infra-red spectral region," *Il Nuovo Cimento*, Vol. 2, No. 5, 1979, [http://link.springer.com/article/10.1007%2FBF02557751, Accessed 12 January 2013].

[16] Kim, I. I., B., M., and E., K., "Comparison of laser beam propagation at 785 nm and 1550 nm in fog and haze for optical wireless communications," *Optical Access Incorporated*, [http://www.lightpointe.com/images/LightPointe_historical_Free_Space_Optics_info_Comparison_of_laser_beam_propagation_MRV_7.pdf, Accessed on 17 January 2013].

[17] Andreev, V., "High Current Density GaAs and GaSb Photovoltaic Cells for Laser Power Beaming," 2003, [http://www.ioffe.ru/pvlab/pdf/3P-B5-33.pdf, Accessed 13 January 2013].

[18] Landis, G. A., "Extended Temperature Solar Cell Technology Development," 2004, [http://ntrs.nasa.gov/archive/nasa/casi.ntrs.nasa.gov/20050198962_2005199189.pdf, Accessed 12 January 2013].

[19] Sawhney, G., *Heat and Mass Transfer*, I K International Publishing House Pvt. Ltd., 2nd ed., 2010.

[20] Oomen, G., "CIGS Cells for Space," *Dutch Space*, [http://www.solar-technology.nl/assets/presentaties/Dutch-Space-Gijs-Oomen.pdf, Accessed on 12 January 2012].

[21] Snijder, M., "GG N026J Data sheet," *GreenGran*, 2012, [martin.snijder@greengran.com, Received on 18 January 2013].

[22] Young, H. D., *HyperPhysics*, Addison Wesley, 7th ed., 1992.

[23] "Space Solar Cells — Emcore," *Emcore*, [http://www.emcore.com/space-photovoltaics/space-solar-cells/, Accessed on 23 January 2013].

[24] Black, A. and Copley, S., "Laser Technology for Materials Processing," *Penn State University*, [http://www.asminternational.org/static/Static%20Files/IP/Magazine/AMP/V168/I01/amp16801p31.pdf, Accessed 23 January 2013].

[25] Bonenschansker, I., "Solar Boat en Zonnecellen," *Delft University of Technology*, [http://tudelft.nl/actueel/dossiers/archief/solar-boat/zonnecellen/solar-boat-en-zonnecellen/, in Dutch Accessed 23 January 2013].

[26] "Europe's Energy Portal Fuel Prices, Rates for Power and Natural Gas," *Europe's energy Portal*, [http://www.energy.eu, Accessed on 23 January 2013].

[27] van Tooren, M. J. L., La Rocca, G., Vos, R., and Zandbergen, B., "AE1201 A/C Preliminary Sizing (class I weight estimation method) 2010," *Faculty of Aerospace Engineering, Delft University of Technology*.

[28] van Tooren, M. J. L., La Rocca, G., Vos, R., and Zandbergen, B., "AE1201 A/C Preliminary Sizing (T/W-W/S diagram) Part 1 of 2 2010," *Faculty of Aerospace Engineering, Delft University of Technology*.

[29] La Rocca, G., "AE2101 Wing Design Part 1 2010," *Faculty of Aerospace Engineering, Delft University of Technology*.

[30] La Rocca, G., "AE3201 Design of unconventional solutions for stability and control: V-Tail and Canard 2012," *Faculty of Aerospace Engineering, Delft University of Technology*.

[31] Mulder, J. e. a., "Flight Dynamics AE3202," *TU Delft, Faculty of Aerospace Engineering*.

[32] La Rocca, G., "AE2101 Wing Design Part 2 2010," *Faculty of Aerospace Engineering, Delft University of Technology*.

[33] La Rocca, G., "AE3201 Weight estimation and iterations in a/c design; aircraft balance 2012," *Faculty of Aerospace Engineering, Delft University of Technology*.

[34] La Rocca, G., "AE2101 Wing Design Part 3 2010," *Faculty of Aerospace Engineering, Delft University of Technology*.

[35] Sadraey, M., "Aileron Design," *Aircraft Design: A systems engineering approach*, 2012, [http://faculty.dwc.edu/sadraey/AileronDesign.pdf, Accessed on 15 January 2013].

[36] "Certification Specifications for Very Light Aeroplanes CS-VLA Amendment 1 5 March 2009," *European Aviation Safety Agency (EASA)*.

[37] La Rocca, G., "AE3021 Aircraft Design V-n diagram 2012," *Faculty of Aerospace Engineering, Delft University of Technology*.

[38] "HexPly M21 Datasheet," *Hexcel*, 2010, [http://www.hexcel.com/Resources/DataSheets/Prepreg-Data-Sheets/M21_global.pdf, Accessed on 18 January 2013.].

[39] Niu, M. C. Y., *Composite Airframe Structures: Practical Design Information and Data*, Conmilit Press Ltd., 1st ed., 1992.

[40] Gardiner, G., "Out-of-Autoclave Prepregs: Hype or Revolution?" *Composites World*, 2011, [http://www.compositesworld.com/articles/out-of-autoclave-prepregs-hype-or-revolution, Accessed 18 January 2013.].

[41] Megson, T. H. G., *Aircraft Structures for Engineering Students*, Elsevier, 4th ed., 2007.

[42] van Tooren, M. J. L., La Rocca, G., Vos, R., and Zandbergen, B., "AE1201 The Design of the Fuselage Part 2 of 2 2010," *Faculty of Aerospace Engineering, Delft University of Technology*.

[43] "NF30, 50, 70 Data sheet," *GreenGran*, [http://www.agrofibrecomposites.com/GreenGranNF305070factsheetandcomparisonchart.pdf, Accessed on 25 January 2013.].

[44] Melkert, J. A., "AE3021 Aircraft Design Improved drag prediction 2008," *Faculty of Aerospace Engineering, Delft University of Technology*.

[45] La Rocca, G., "AE3201 Requirement Analysis and Design principles for A/C stability control (Part 1) 2012," *Faculty of Aerospace Engineering, Delft University of Technology*.

[46] La Rocca, G., "AE3201 Requirement Analysis and Design principles for A/C stability control (Part 2) 2012," *Faculty of Aerospace Engineering, Delft University of Technology*.

[47] Eugene, L., "Effect of canard deflection on close-coupled canard-wing-body aerodynamics," 1992, [http://www.researchgate.net/publication/23863217_Effect_of_canard_deflection_on_close-coupled_canard-wing-body_aerodynamics, Accessed on 15 January 2013].

[48] La Rocca, G., "AE3201 Aircraft Design 2008-2009: vertical tailplane data," *Faculty of Aerospace Engineering, Delft University of Technology*.

[49] Sadraey, M., "Rudder Design," *Aircraft Design: A systems engineering approach*, 2012, [http://faculty.dwc.edu/sadraey/RudderDesign.pdf, Accessed on 15 January 2013].

[50] van Tooren, M. J. L., La Rocca, G., Vos, R., and Zandbergen, B., "AE1201 A/C Preliminary Sizing (T/W-W/S diagram) Part 2 of 2 2010," *Faculty of Aerospace Engineering, Delft University of Technology*.

[51] Anderson, J., *Introduction to Flight*, McGraw-Hill Series in Aeronautical and Aerospace Engineering, McGraw-Hill, 2008.

[52] "The Bolly book," *Bolly Products*, [http://www.bolly.com.au/1998BollyBookv3.pdf, Accessed on 12 January 2013.].

[53] Schenk, H., "Propeller calculator," [http://www.drivecalc.de/PropCalc/index.html, Accessed on 13 January 2013.].

[54] Barnard, J., "Model Aircraft Propellers," *Barnard Microsystems Limited*, [https://www.faa.gov/news/fact_sheets/news_story.cfm?newsId=6275, Accessed on 13 January 2012.].

[55] "Jane's UAV database," *Jane's Aircraft*.

[56] Gundlach, J., *Designing Unmanned Aircraft Systems: A Comprehensive Approach*, AIAA Education Series, Amer Inst of Aeronautics &, 2011.

[57] "Folding Propeller w/ Alloy hub - 11x6," *HobbyKing*, [http://www.hobbyking.com/hobbyking/store/uh_viewItem.asp?idProduct=5331, Accessed on 17 January 2013].

[58] "PR-EW2208 inch Carbon Fiber Propeller for rc airplane 45-60CC engine," *Alibaba.com*, [http://www.alibaba.com/product-gs/518767173/PR_EW2208_inch_Carbon_Fiber_Propeller.html, Accessed on 17 January 2013].

[59] "Carbon fiber sheets," *Composite Resources*, [http://www.composite-resources.com/product/carbon-fiber-sheets, Accessed on 17 January 2013].

[60] "Glass filled nylon," *The plastic shop*, [http://www.theplasticshop.co.uk/plastic_technical_data_sheets/glass_filled_nylon_technical_data_sheet.pdf, Accessed on 17 January 2013].

[61] "Electronica, Quadro/Multicopters en toebehoren," *Lynx modelbouw*.

[62] "Graupner Elektro prop 22x10," *Albatros Modelbouw*, [http://www.albatrosmodelbouw.be/product.php?id_product=2093, Accessed on 17 January 2013].

[63] "DC Motor / Propeller Matching," *Lab 5 Lecture Notes*, 2005.

[64] "Power Series Brushless Motors," *Horizon Hobby Brand*, [http://www.e-fliterc.com/PowerSystems/Motors/BrushlessCharts.aspx, Accessed on 14 January 2013].

[65] Greenhalgh, S., "PropCalc," *eSouring.net*, [http://www.esoaring.net/forum/viewtopic.php?f=3&t=852, Accessed on 15 January 2013].

[66] Zandbergen, B. T. C., *Aerospace Vehicle Electrical power systems*, 2010.

[67] R., W. J. and L., W. J., *Space Mission Analysis and Design*, Microsm Press and Kluwer Academic Publishers, 3rd ed., 1999.

[68] Enslin, H. R. and Wolf, S. M., "Integrated Photovoltaic Maximum Power Point Tracking Converter," *IEEE Transactions on Industrial Electronics*, [http://ieeexplore.ieee.org/stamp/stamp.jsp?tp=&arnumber=649937, Accessed on 18 January 2013.].

[69] "High energy, lightweight batteries," *Barnard Microsystems Limited*, [http://www.barnardmicrosystems.com/L4E_batteries.htm, Accessed on 17 January 2013.].

[70] "Lithium-Ion Battery Cell Specification," [http://www.batteryspace.com/prod-specs/icr18650nh-2200.pdf, Accessed on 17 January 2013.].

[71] "Comparison of battery types," [http://www.allaboutbatteries.com/electric_cars.html, Accessed on 11 January 2013.].

[72] "A design to generate UAV electrical power in flight," [http://www.eetimes.com/design/military-aerospace-design/4374725/A-design-to-generate-UAV-electrical-power-in-flight, Accessed on 10 January 2013.].

[73] "Certification Specifications for Normal, Utility, Aerobatic, and Commuter Category Aeroplanes CS-23," *European Aviation Safety Agency*, [http://www.easa.europa.eu/agency-measures/docs/certification-specifications/CS-23/CS-23%20Amendment%202%20(corrigendum).pdf, Accessed on 17 January 2013.].

[74] "Lithium-Ion Battery for Spacecraft applications," *Air Force Space Command*, [https://info.aiaa.org/tac/PEG/APSTC/SpecificationsStandardsReports/SMCStandardSMC-S-017(2008)-Li-IonBatterySV.pdf, Accessed on 17 January 2013.].

[75] *Conrad*, [http://www.conrad-uk.com/ce/en/product/110706?WT.mc_id=googlebase&insert=8V&adcampaign=googlebase&CAWELAID=858567535, Accessed on 17 January 2013.].

[76] "High energy, lightweight batteries," *Conrad*, [http://www.conrad-uk.com/ce/en/FastSearch.html?search=wiring+and+connectors&initial=true&categorycode=, Accessed on 17 January 2013.].

[77] Roskam, J., *Airplane Design: Preliminary Calculation of Aerodynamic, Thrust and Power Characteristics*, Airplane Design, Darcorporation, 2000.

[78] Phillips, W., *Mechanics of Flight*, Aerospace/Engineering, John Wiley & Sons, 2004.

[79] Hoh, R. Nicoll, T., "Criteria to mitigate rudder overcontrol in transport aircraft," *HOH Aeronautics*.

[80] "Pegasus Actuators," *Pegasus Actuators GmbH*, [http://www.pegasus-actuators.com/en/sites/products/, Accessed on 16 January 2013].

[81] "PA-Control," *Pegasus Actuators GmbH*, [http://www.pegasus-actuators.com/fileadmin/datasheet/135-4/PA-R-135-4datasheet.pdf, Accessed on 16 January 2013].

[82] "PA-Control," *Pegasus Actuators GmbH*, [http://www.pegasus-actuators.com/fileadmin/datasheet/250-9/datasheetPA-R-250-9series.pdf, Accessed on 16 January 2013].

[83] Chao, H. Cao, Y. and Chen, Y., "Autopilots for Small Unmanned Aerial Vehicles: A Survey," 2010, [http://www.u-nav.com/images/Autopilots_for_Small_Unmanned_Aerial_Vehicles_A_Survey.pdf, Accessed on 14 January 2013.].

[84] Barnard, J., "Small UAV Command, Control and Operation Issues," *Barnard Microsystems Limited*.

[85] Kull, P., "Request," [p.kull@pegasus-actuators.com, Email received on 15 January 2013].

[86] "Vogels in Nederland," *Vogelbescherming Nederland*, 2013, [http://www.vogelbescherming.nl/service__vragen/vragen__antwoorden/q/fq_id/54, Accessed on 8 January 2012.].

[87] "Environmental information sheet," *Civil aviation authority*, 2008, [http://www.caa.co.uk/docs/7/EIS2008.pdf, Accessed on 8 January 2012.].

[88] "Peregrine falcon," *All about birds*, [http://www.allaboutbirds.org/guide/Peregrine_Falcon/id, Accessed on 8 January 2012.].

[89] N, S.-R. J., Yelton, D., Witt, C., and Galetti, R., "Passive Obstacle Detection System for Wire Detection," [http://pages.swcp.com/~spsvs/resume/PODS_DSS2009_2009-01-15.pdf, Accessed on 7 January 2012.].

[90] "Real time optical flow," 2007, [http://www.academypublisher.com/jmm/vol02/no05/jmm02053845.pdf, Accessed on 24 January 2012.].

[91] Larkin, P., Torre-Bueno, J., Griffin, R., and Walcott, C., "Reactions of Migrating Birds to Lights and Aircraft," 1975, [http://www.ncbi.nlm.nih.gov/pmc/articles/PMC432678/pdf/pnas00049-0020.pdf, Accessed on 8 January 2012.].

[92] "Bird scared," 2013, [http://www.livescience.com/21497-aircraft-bird-collisions.html, Accessed on 24 January 2012.].

[93] "Pigeon control," 2013, [http://www.pigeoncontrolresourcecentre.org/html/reviews/remove-pigeons-birds-of-prey.html, Accessed on 24 January 2012.].

[94] "Planck law," 2013, [http://scienceworld.wolfram.com/physics/PlanckLaw.html, Accessed on 9 January 2012.].

[95] "Body temperatures," 2012, [http://www.goldennumber.net/body-temperatures, Accessed on 18 January 2012.].

[96] "Heat transfer from starlings sturnus volgaris during flight," 1999, [http://jeb.biologists.org/content/202/12/1589.full.pdf, Accessed on 10 January 2012.].

[97] Zangh, X., "Atmosphere Infrared Absorption Model," 2011, [http://ia701508.us.archive.org/27/items/AtmosphereInfraredAbsorptionModelAtmosphericWindow/Cisme-20110307-093636-6502-9P1--5.pdf, Accessed on 10 January 2012.].

[98] Glickstein, I., "Atmosphere Infrared Absorption Model," 2011, [http://wattsupwiththat.com/2011/02/28/visualizing-the-greenhouse-effect-atmospheric-windows/, Accessed on 11 January 2012.].

[99] "Radiance from the sea surface," *Ocean Optics*, [http://www.oceanopticsbook.info/view/remote_sensing/level_2/counting_photons, Accessed on 8 January 2012.].

[100] "Earth Radiance vs Blackbody Spectra," *NASA*, [http://climate.gsfc.nasa.gov/static/cahalan/Radiation/EarthRadVblackbody.html, Accessed on 8 January 2012.].

[101] "Sensitivity," *FLIR*, [http://www.flir.com/uploadedfiles/Eurasia/MMC/Appl_Stories/AS_0015_EN.pdf, Accessed on 10 January 2012.].

[102] "Optics conversion factor," *Caeleste*, [http://www.caeleste.be/lexicon/nep.html#_ftn2, Accessed on 10 January 2012.].

[103] "Color depth," *Snapsort*, [http://snapsort.com/learn/sensor/dxo-mark/color-depth, Accessed on 14 January 2012.].

[104] "Pixels for detection," *AXIS*, [http://www.axis.com/academy/identification/resolution.htm, Accessed on 14 January 2012.].

[105] "Megapixel calculator," *MPEG-4 comprissing codes for different resolutions*, [http://www.hautespot.net/support/IP/Camera/Calculator.htm, Accessed on 14 January 2013].

[106] "Flir T440," *Flir*, [http://www.shopflir.com/p12073/flir_t440_thermal_imaging_camera.php, Accessed on 22 January 2012.].

[107] "Hero3," *GoPro*, [http://gopro.com/cameras/hd-hero3-black-edition, Accessed on 22 January 2012.].

[108] "Battery weight," [http://www.dhgate.com/12v-6800mah-for-cctv-camera-super-rechargeable/p-ff8080813976b6530139909e128529f6.html#s1-1-null, Accessed on 22 January 2012.].

[109] "Optical flow," [http://www.jonathanmugan.com/GraphicsProject/OpticalFlow/, Accessed on 14 January 2012.].

[110] Rosa, T., "Absorption at MMW," 2007, [http://www.microwavejournal.com/articles/5214-multi-gigabit-mmw-point-to-point-radios-propagation-considerations-and-case-studies, Accessed on 16 January 2012.].

[111] "Furuno FAR2117," 2012, [http://www.psicompany.com/furuno-far2117-8-radar/, Accessed on 16 January 2012.].

[112] "FLIR PT-series," 2012, [http://www.flir.com/uploadedFiles/0906-409PT-SeriesInsert.pdf, Accessed on 16 January 2012.].

[113] of Technology, C. P. U., "Transmitter data," *Clyde.Space*, [http://www.clyde-space.com/cubesat_shop/communication_systems/301_cubesat-s-band-transmitter, Accessed on 17 January 2013].

[114] "Antennas Data," *Cobham Antenna Systems, Microwave Antennas.LTD*, [http://www.european-antennas.co.uk/antennas-3.php, Accessed on 14 January 2013].

[115] Desveaux, M. P., "Receiver Contact," *Dyplex Communication Ltd.*, [Contacted for the price of the receiver, contacted during week 03].

[116] "Cable data," *Totoku Electric Co,Ltd*, [http://www.shf.de/fileadmin/download/Connectors_and_Cables/totoku_tcf_series_v005.pdf, Accessed on 17 January 2013].

[117] "Absorption at different frequencies," [http://www.radartutorial.eu/07.waves/wa13.en.html, Accessed on 22 January 2012.].

[118] "Receiver VDR1 Data," *Advanced Microwave Products*, [http://www.advmw.com/surveillance_receiver_vdr1.html, Accessed on 14 January 2013].

[119] "Space Mission Analysis and Design," *Donna Klungle, Microcosm, Inc.*, [http://www.smad.com/store/bookstore/stl/smad3err.pdf, Accessed on 14 January 2013].

[120] Creek, S., "Antennas Contact," *COBHAM communications*, [Contacted for the weight and price of the antennas, contacted during week 03].

[121] "QuickTime and MPEG-4," *Apple Computer, Inc., registered in the U.S. and other countries.*, [http://images.apple.com/quicktime/pdf/H264_Technology_Brief.pdf, Accessed on 16 January 2013].

[122] "Skylaunch," *Sky launch*, 2013, [http://www.skylaunchuk.com/, Accessed on 19 January 2012.].

[123] Gibson, J., "The mechanics of the winch launch," [http://www.bfgc.co.uk/Technical/BGAmanual.pdf, Accessed on 17 January 2012.].

[124] Santel, C. G., "Numeric Simulation of a Glider Winch Launch," 2008, [http://darwin.bth.rwth-aachen.de/opus3/volltexte/2010/3265/, Accessed on 15 January 2013.].

[125] Noyes, D., "Achieving a safe winch launch," *DG Flugzeugbau*, [http://www.dg-flugzeugbau.de/windenstart-e.html, Accessed on 15 January 2012.].

[126] Asiimwe, R., Castellanos, J. L., Singh, K., and Teo, Z., "Design of a Recreational Glider," 2012.

[127] "Winch launching manual issue 1," *The gliding federation of Australia*, 1998, [http://2009.gfa.org.au/Docs/ops/Winchmanual.pdf, Accessed on 16 January 2013.].

[128] Gibson, J., "Understanding the Winch Launch," 1987, [http://www.bfgc.co.uk/Technical/Winch.aspx, Accessed on 17 January 2012.].

[129] "Technical Requirements for Winches used to Launch Gliders and Motorgliders," *Technical Commission of the German Aero Club*, 1982, [http://www.ranlog.com/winch/DAeC_Technical_Requirements.pdf, Accessed on 14 January 2012.].

[130] Daniels, B., "Winch project, A proposal," 2003, [http://www.planeur-stflo.net/pages/vavenvol/winch_proposal.pdf, Accessed on 14 January 2012.].

[131] "Winch cable sizing," 2013, [http://www.fibremax.nl/products/dyneema-cables/, Accessed on 16 January 2012.].

[132] "Cable Transducer," *BEI Sensors*, [http://www.beiied.com/PDFs2/Linear_Cable-Transducer_LT25.pdf, Accessed on 17 January 2013].

[133] "Cable strength," *Mt. Buffalo, Australia*, [http://www.digipac.ca/chemical/mtom/contents/chapter1/ltw_001.htm, Accessed on 17 January 2013].

[134] "Net Material," *Mt. Buffalo, Australia*, [http://www.rcgroups.com/forums/member.php?u=61874&page=3, Accessed on 17 January 2013].

[135] "Pole Supporter," *Jiangsu Bosheng Science and Technology Co., Ltd*, [http://www.alibaba.com/product-gs/537535699/30ft_35ft_distribution_steel_pole_post.html, Accessed on 17 January 2013].

[136] "Plastic Net," *Anping Changsheng Wire Mesh Co., Ltd.*, [http://www.alibaba.com/product-gs/504801139/plastic_fishing_net.html?s=p, Accessed on 17 January 2013].

[137] "Fatigue and Damage Tolerance Evaluation of Structures, The Composite Materials Response," *National Aerospace Laboratory NLR*, [http://reports.nlr.nl:8080/xmlui/bitstream/handle/10921/224/TP-2009-221.pdf?sequence=1, Accessed on 17 January 2013.].

[138] "Third Generation Glass Wool," *Ecophon*, [http://www.ecophon.com/en/Topmenu-right-Toolbar-container/About-Ecophon/Environmental-statement/Third-generation-glass-wool/, Accessed on 18 January 2013].

[139] "Fatalities in Australian Mining," *West Australian Government*, [http://exiswww.dmp.wa.gov.au/, Accessed on 14 January 2013].

[140] Riseborough, J., "Ipad Boom Strains Lithium Supplies After Prices Triple," *Bloomberg*, [http://www.bloomberg.com/news/2012-06-19/ipad-boom-strains-lithium-supplies-after-prices-triple.html, Accessed on 14 January 2013].

[141] "Lithium Battery Recycling," *Altprofits*, [http://www.altprofits.com/ref/ct/nbo/mao/lithium_battery_recycling.html, Accessed on 14 January 2013].

[142] "Toxco Gets 9.5 Million DOE Grant for Battery Recycling," *Autoblog*, [http://green.autoblog.com/2009/08/18/toxco-gets-9-5-million-doe-grant-for-battery-recycling/, Accessed on 14 January 2013].

[143] Kramer, D. A., "Mineral Commodity Summary 2006: Gallium," *United States Geological Survey*, 2008, [http://minerals.usgs.gov/minerals/pubs/commodity/gallium/, Accessed 15 January 2013].

[144] Greber, J. F., *Ullmann's Encyclopedia of Industrial Chemistry*, Wiley-VCH, 7th ed., 2012.

[145] *Air pollution from electricity-generating large combustion plants*, Copenhagen: European Environment Agency (EEA), 1st ed., 2008.

[146] "Surface meteorology and Solar Energy," *NASA*, [http://eosweb.larc.nasa.gov/cgi-bin/sse/sse.cgi, Accessed on 5 December 2012].

[147] Lenzen, M., "Life-cycle energy balance and greenhouse gas emissions of nuclear energy: A review," *pandora-archive Energy Conversion & Management*, 2008, [http://www.isa.org.usyd.edu.au/publications/documents/ISA_Nuclear_Report.pdf, Accessed 16 January 2013].

[148] "Opbrengst Windenergy op Land," *Dutch Ministry of Infrastructure and Environment*, [http://www.windenergie.nl/onderwerpen/techniek/opbrengst, Accessed on 18 January 2013].

[149] "Inventory of Embedded Energy," *Inventory of Carbon and Energy*, [http://perigordvacance.typepad.com/files/inventoryofcarbonandenergy.pdf, Accessed on 20 January 2013].

[150] De Vegt, O., "Comparative environmental life cycle assessment of composite materials," *ECN*, 1997, [ftp://ftp.ecn.nl/pub/www/library/report/1997/i97050.pdf, Accessed 21 January 2013].

[151] "Environmental impacts of batteries for low carbon technologies compared," *European Commission*, [http://ec.europa.eu/environment/integration/research/newsalert/pdf/303na1.pdf, Accessed on 21 January 2013].

[152] "Well-to-Wheel emissions of carbon dioxide," *CE*, [http://www.ce.nl/?go=home.downloadPub&id=790&file=08_448_11.pdf, Accessed on 20 January 2013].

[153] "Penguin B UAV Factory Unmanned Platforms and Subsystems," *UAV Factory*, [http://www.uavfactory.com/product/46, Accessed on 22 January 2013].

APPENDIX A

COMPLIANCE MATRIX

Aircraft requirements					
General requirements					
Code	Requirement	Fulfilled?	Section	Responsible Person(s)	Comment
AG. 2	The aerial vehicle shall be unmanned.	✓	5.1, 5.3	FL, TN	
AG. 3	The aerial vehicle shall be a fixed wing aircraft in canard configuration.	✓	4.1, 4.3	RH, JR	
AG. 4	The aircraft shall be able to carry a payload of at least 10 kg.	✓	4.2	LG	
AG. 5	The aircraft shall be able to monitor continuously.	✓	5.5	RH	
AG. 6	The aircraft shall be powered by optical power beaming with lasers.	✓	3.2, 3.3	PP, BS	
AG. 7	The aircraft shall have an operational life of 5 years.	✓	4.1-4.3	LG	
AG. 8	The aircraft shall have cruise velocity of 100 km h^{-1}.	✓	4.1-4.4	RH, JR	
AG. 9	The aircraft shall cruise at an altitude of 230 m.	✓	4.1-4.4	RH, JR	
AG. 10	The aircraft shall be able to perform turning flight at a velocity of 100 km/h.	✓	4.1-4.4	RH, JR	
AG. 11	The aircraft shall be able to perform turning flight at a bank angle of 30°	✓	4.1-4.4	RH, JR	
AG. 12	The aircraft shall be able to perform climbing flight with a flight path angle of 5°	✓	4.1-4.4	RH, JR	
AG. 13	The aircraft shall be able to avoid ground based obstacles.	✓	5.2	SU	
AG. 14	The aircraft shall be able to avoid animals.	✓	5.2	SU	
AG. 15	The aircraft shall be able to avoid air traffic.	✓	5.2	SU	
Wing requirements					
AW. 2	The wing shall optionally provide attachment for the vertical stabilisers/winglets.	✓	4.1	LG	
AW. 3	The wing shall provide attachment for the ailerons.	✓	4.1	LG	
AW. 4	The ailerons shall be positioned outside the disturbed flow of the foreplane.	✓	4.3	FL	
AW. 5	The wing shall not block the path between the laser and the photovoltaic cells.	✓	4.1, 3.3	LG, PP	
Fuselage requirements					
AF. 1	The fuselage shall provide space for the payload.	✓	4.2	LG	
AF. 2	The fuselage shall provide space for the subsystems.	✓	4.2	LG	
AF. 3	The fuselage shall have a shape such that there are no laser hazards due to reflected laser light.	✓	3.3, 4.2	LG, PP	
Foreplane requirements					
AH. 2	The foreplane shall ensure longitudinal equilibrium of moments around the centre of gravity in steady flight.	✓	4.3	RH, JR	
AH. 3	The foreplane shall provide longitudinal stability around the state of equilibrium under all flight conditions.	✓	4.3	RH, JR	
AH. 4	The foreplane shall provide attachment for the elevators.	✓	4.3	LG	
AH. 5	The foreplane shall not block the path between the laser and the photovoltaic cells.	✓		RH, JR	
Vertical stabiliser requirements					
AV. 1	The vertical stabiliser shall provide lateral stability under all flight conditions.	✓	4.4	RH, JR	
AV. 2	The vertical stabiliser shall provide attachment for the rudder.	✓	4.4	LG	
Structure requirements					
AS. 1	The structure shall be able to cope with the loads during all flight conditions over its operational life.	✓	4.1-4.4	LG	
AS. 2	The structure shall be able to cope with the launch loads.	✓	4.1-4.4	LG	
AS. 3	The structure shall be able to cope with the landing loads.	✓	4.1-4.4	LG	
AS. 4	The structure shall not fail in the event of a lightning strike.	✓	4.1-4.4	LG	Further consideration required during the detail design.

Figure A.1: Compliance matrix part one.

Code	Requirement	Fulfilled?	Section	Responsible Person(s)	Comment
AS. 5	The structure shall provide attachment for the wing.	✓	4.1	LG	
AS. 6	The structure shall provide attachment for the foreplane.	✓	4.3	LG	
AS. 7	The structure shall provide attachment for the vertical stabiliser(s).	✓	4.4	LG	
AS. 8	The structure shall provide attachment for the electric motor.	✓	4.2	LG	
AS. 9	The structure shall provide attachment for the photovoltaic cells.	✓	4.2	LG	
Energy collection system requirements					
AL. 1	The aircraft shall collect laser energy from the laser base stations using gallium arsenide photovoltaic cells.	✓	3.3	PP	
AL. 2	The photovoltaic cells shall be able to collect enough power to simultaneously charge the batteries, power the electric motor at maximum power and power the systems at all angles and distances to the laser base station.	✓	3.3	PP	
AL. 3	The photovoltaic cells shall be positioned on the fuselage.	✓	3.3, 4.2	PP	
AL. 4	The photovoltaic cells shall have a shape such that there are no laser hazards due to reflected laser light.	✓		PP	
AL. 5	The photovoltaic cells shall not fail due to overheating.	✓	3.3, 4.2	PP	
Energy storage system requirements					
AB. 1	The aircraft shall store energy using Sion Power lithium-sulphur batteries.	✗	4.6	SM	Lithium-ion batteries are used instead due a higher number of operational cycles
AB. 2	The batteries shall provide enough power to fly for 18 minutes without laser power when the aircraft is in normal operations.	✓	4.6	SM	Sized for 30 minutes due a change in laser beaming.
AB. 3	The batteries shall be able to fully recharge in 3 hours when the aircraft is in normal operations.	✓	4.6	SM	
Electric system requirements					
AE. 1	The electric system shall receive power from the energy collection system.	✓	4.6	SM	
AE. 2	The electric system shall store energy in the energy storage system.	✓	4.6	SM	
AE. 3	The electric system shall check the energy stored.	✓	4.6	SM	
AE. 4	The electric system shall distribute power among the systems.	✓	4.6	SM	
AE. 5	The electric system shall provide power to the electric motor.	✓	4.6	SM	
Propulsion requirements					
AP. 1	The aircraft shall be propelled by an electric motor with propeller.	✓	4.5	FL	
AP. 2	The electric motor shall provide enough power for the aircraft to perform the required manoeuvres when the aircraft is in normal operations.	✓	4.5	FL	
AP. 3	The electric motor shall be positioned at the rear of the aircraft facing backwards.	✓	4.5	FL	
AP. 4	The electric motor shall not produce a sound intensity level higher than 107 dB (A) at 1 m distance.	✗	4.5	FL	A sound intensity level could not be obtained, but the tip speed of the propeller is way below Mach 0.7, which satisfies the limit from Roskam.
Attitude and position system requirements					
AA. 1	The attitude and position system shall use inertial navigation system and global positioning system for attitude, position and velocity determination of the aircraft.	✓	5.1	FL	
AA. 2	The aircraft shall follow its received flight path commands.	✓	5.1	FL	

Figure A.2: Compliance matrix part two.

Code	Requirement	Fulfilled?	Section	Responsible Person(s)	Comment
Communication system requirements					
AR. 1	The communication system shall provide communications among the on board systems using electric wiring.	✓	5.3	TN	
AR. 2	The aircraft shall receive positioning data from the global positioning system.	✓	5.3	TN	
AR. 3	The aircraft shall communicate with the laser base stations and the ground station using radio frequencies.	✓	5.3	TN	
AR. 4	The aircraft shall send attitude, position, velocity, energy status and system status data to the ground station.	✓	5.3	TN	
AR. 5	The aircraft shall send thermal and visual view to the ground station.	✗	5.3	TN	Communication through laser base station is much faster.
AR. 6	The aircraft shall continuously send mission data to the ground station.	✗	5.3	TN	Communication through laser base station is much faster.
AR. 7	The aircraft shall receive its flight path commands from the ground station.	✗	5.3	TN	Communication through laser base station is much faster.
AR. 8	The aircraft shall receive its system commands from the ground station.	✗	5.3	TN	Communication through laser base station is much faster.
AR. 9	The aircraft shall send attitude, position and velocity data to the laser base stations.	✓	5.3	TN	
AR. 10	The aircraft shall receive energy transfer status from the laser base stations.	✓	5.3	TN	
Control system requirements					
AC. 1	The control system shall use flight path commands to control the aircraft.	✓	5.1	FL	
AC. 2	The control shall autonomously evade obstacles detected by the obstacle detection system.	✓	5.1, 5.2	FL, SU	
AC. 3	The aircraft shall use elevators for pitch control under all flight conditions.	✓	4.3, 5.1	FL	
AC. 4	The aircraft shall use ailerons for roll control under all flight conditions.	✓	4.1, 5.1	FL	
AC. 5	The aircraft shall use (a) rudder(s) for yaw control under all flight conditions.	✓	4.4, 5.1	FL	
Obstacle detection systems requirements					
AO. 1	The aircraft shall detect obstacles with a thermal optical camera.	✓	5.2	SU	
AO. 2	The thermal optical camera shall be positioned such that it can be used for obstacle detection in the direction of flight.	✓	4.2, 5.2	SU, LG	
AO. 3	The thermal optical camera shall be positioned such that the pilot has a clear overview in the direction of flight.	✓	4.2, 5.2	SU, LG	
Laser base station requirements					
General requirements					
LG. 1	Four laser base stations shall be available to provide power to the aircraft.	✓	3.2	PP	
LG. 2	The laser base stations shall cover an area of 10 by 10 km^2.	✓	5.5	RH	
LG. 3	The laser base station shall continuously provide power to the aircraft.	✗	3.2	PP	Batteries required, beaming continuously not possible due to reflection

Figure A.3: Compliance matrix part three.

Code	Requirement	Fulfilled?	Section	Responsible Person(s)	Comment
LG. 5	The laser range from the laser base stations to the aircraft shall be at most 4 km.	✓	4.1-4.4	JR	
LG. 6	The angle between the ground and the laser path shall be at minimum 3.3°.	✓	4.1-4.4	BS	
LG. 8	Laser hazards to animals shall be avoided.	✓	5.2	SU	
LG. 9	Laser hazards to air traffic shall be avoided.	✓	5.2	SU	
LG. 10	Laser hazards to the aircraft shall be avoided.	✓	5.2	SU	
Communication requirements					
LC. 1	The communication system shall provide communications among the systems of the laser base station using electric wiring.	✓	5.3	TN	
LC. 2	The laser base station shall communicate with the aircraft using radio frequencies.	✓	5.3	TN	
LC. 3	The laser base station shall receive attitude, position and velocity data from the aircraft.	✓	5.3	TN	
LC. 4	The laser base station shall send energy transfer status to the aircraft.	✓	5.3	TN	
LC. 5	The laser base station shall communicate with the ground station using telephone cable.	✓	5.3	TN	
LC. 6	The laser base station shall send system status data to the ground station.	✓	5.3	TN	
LC. 7	The laser base station shall receive commands from the ground station.	✓	5.3	TN	
Tracking system requirements					
LT. 1	The tracking system shall use attitude, position and velocity data from the aircraft for initial tracking.	✓	3.1	BS	
LT. 2	The tracking system shall use a tracking laser to pinpoint on the photovoltaic cells on the aircraft.	✓	3.1	BS	
Aiming system requirements					
LA. 1	The aiming system shall use data from the tracking system to aim the laser.	✓	3.1	BS	
LA. 2	The angular velocity of the aiming system shall be $7° \ s^{-1}$.	✓	3.1	BS	
LA. 3	The angular resolution of the aiming system shall be 25 μ rad both horizontally and vertically.	✓	3.1	BS	
LA. 4	The update frequency of the aiming system direction shall be at least 278 Hz.	✓	3.1	BS	
LA. 5	The laser shall at all time be aimed at the photovoltaic cell area on the aircraft when it is active.	✓	3.1	BS	
Obstacle detection system requirements					
LO. 1	The obstacle detection system shall detect obstacles with an optical camera.	✓	5.2	SU	
LO. 2	The obstacle detection system shall detect obstacles with a thermal camera.	✓	5.2	SU	
LO. 3	The obstacle detection system shall detect obstacles at long range with radar.	✓	5.2	SU	
LO. 4	The obstacle detection system shall be able to detect ground based obstacles within and close to the laser path.	✓	5.2	SU	
LO. 5	The obstacle detection system shall be able to detect animals within and close to the laser path.	✓	5.2	SU	
LO. 6	The obstacle detection system shall be able to detect air traffic within and close to the laser path.	✓	5.2	SU	

Figure A.4: Compliance matrix part four.

Code	Requirement	Fulfilled?	Section	Responsible Person(s)	Comment
Laser requirements					
LL. 1	The laser shall be able to transfer enough power to simultaneously charge the batteries, power the electric motor at maximum power and power the systems of the aircraft at all angles and distances to the laser base station.	✓	3.2	PP	
LL. 2	The laser light shall have a wavelength in the range of 820 - 850 nm.	✓	3.2	PP	
LL. 3	The laser beam shall be divergent.	✓	3.2	PP	
Operational requirements					
General operational requirements					
OG. 1	Two aircraft shall operate simultaneously in the same network.	✓	5.5	RH	
OG. 2	The aircraft shall periodically land for maintenance.	✓	5.4	SM	
OG. 3	The batteries shall periodically be replaced.	✓	4.6	SM	
OG. 4	The aircraft shall be recovered in case of need for maintenance.	✓	5.4	SM	
OG. 5	The aircraft shall be recovered in case of critical on board system failures.	✓	5.4	SM	
OG. 6	The aircraft shall be recovered in case of critical laser base station failures.	✓	5.4	SM	
OG. 7	The aircraft shall be recovered in case of a power outage of the electric grid.	✓	5.4	SM	
Launch requirements					
OL. 1	The aircraft shall be launched from a rail using a winch.	✓	5.4	SU	
OL. 1	The aircraft shall be launched from Rotterdam airport.	✗	5.4	SU	Different locations are considered
Recovery requirements					
OR. 1	The aircraft shall be recovered using a net.	✓	5.4	SM, TN	
OR. 2	The aircraft shall be recovered at Rotterdam airport.	✗	5.4	SM, TN	Four different locations are available for landing
Monitoring requirements					
OM. 1	The aircraft in the network shall monitor an area of 10 by 10 km^2 around the motorway network of the Hague.	✓	5.5	RH	
OM. 2	The aircraft in the network shall operate in scanning mode and emergency mode.	✓	5.5	RH	
OM. 3	In scanning mode, the aircraft in the network shall fly the same flight path, while monitoring the priority area consisting of the A4, A12, A13 and N44 motorways with an interval of at most 15 minutes.	✓	5.5	RH	
OM. 4	In emergency mode, one of the aircraft in the network shall leave its flight path and fly to and loiter above the emergency target area.	✓	5.5	RH	
Miscellaneous requirements					
Sustainability requirements					
MS. 1	The aircraft shall be recyclable at end of life.	✗	4.1-4.4, 7.1	SM, PP	Batteries cannot be recycled.
MS. 2	Renewable energy options to power the electric grid shall be identified.	✓	7.2	PP	
Other requirements					
MO. 1	A design concept shall be presented in 10 weeks.	✓	All	All	

Figure A.5: Compliance matrix part five.

APPENDIX B

FUNCTIONAL FLOW DIAGRAM

B.1 Functional Flow Diagram

In the final design phase the Functional Flow Diagram is created. It shows all functions that are required from the system. For this project, two Functional Flow Diagrams are created. One for the aircraft and one for the network of base stations. These two diagrams are also interlinked at some points.

B.1.1 Aircraft

There are multiple aircraft flying in the network. Each aircraft is represented as a subsystem. Figure B.1 shows the Functional Flow Diagram for the aircraft subsystem. The diagram consists of a top level and two sub-levels. The pre-operational inspection is to make sure the aircraft is capable of performing the mission. Then the aircraft can be deployed. The sub level of the launch function describes the winch launch procedure. From that moment on the aircraft has to be operated. Operating the aircraft basically means keeping the aircraft in the air. To keep the aircraft in the air, it should not fly into obstacles. It should also fly a specific flight path assigned by the network. On the sub-level, this means continuously monitoring of position, attitude and obstacles. Then it sends this data to the network, along with the current energy status. The network receives this data and uses it to construct a flight path. This flight path is sent to and received by the aircraft. The autopilot on board the aircraft uses information from speed and attitude measurements to deflect control surfaces and regulate motor power. The flight path constructed by the network also depends on the energy status of the aircraft. When the aircraft requires energy, it is directed to fly in the range of lasers. The laser energy is transferred to the aircraft and stored by batteries. After deployment, the aircraft also has to fly to the destination area. When the destination area is reached, the payload is initialized. This allows the equipment to monitoring the urban area. The collected data is send to the network and processed there. When the mission is over or maintenance is required, the aircraft is cached with a net an switched off.

B.1.2 Network

The operations are done from the network. The Functional Flow Diagram of the network is shown in figure B.2. The network consists of one base station for operations and four laser base stations. Before the flight path of a certain aircraft can be constructed, a few steps have to be taken. First, the positions of the aircraft are required. They are sent by the aircraft and received by the network. Then, the network judges the weather conditions. Depending on the received status from the aircraft, the requirement for maintenance is judged. When necessary, the aircraft can be recovered and stored or maintained. When it is not necessary to recover the aircraft, the target area is obtained by the network. This target area is specified by the operator of the system. Any obstacles on the way are identified and will be avoided in the flight path. When laser power is required, there are some additional requirements for the flight path. It is not possible to power two aircraft with one laser, so one aircraft can than be redirected to another laser. For safety reasons, there should not be any obstacles in between the laser and the aircraft. Also the extended laser path should be clear of obstacles as other aircraft and satellites. Tracking of the aircraft is done by first scanning around the estimated position of the aircraft with the laser beam at low power. When the PV cell on the aircraft detects the laser beam, a signal is sent to the laser base station. Then, the laser can start following the aircraft using feedback from the PV cell. If everything is safe, the laser power is set to transfer rate. The final flight path is constructed by the network and then sent to the aircraft.

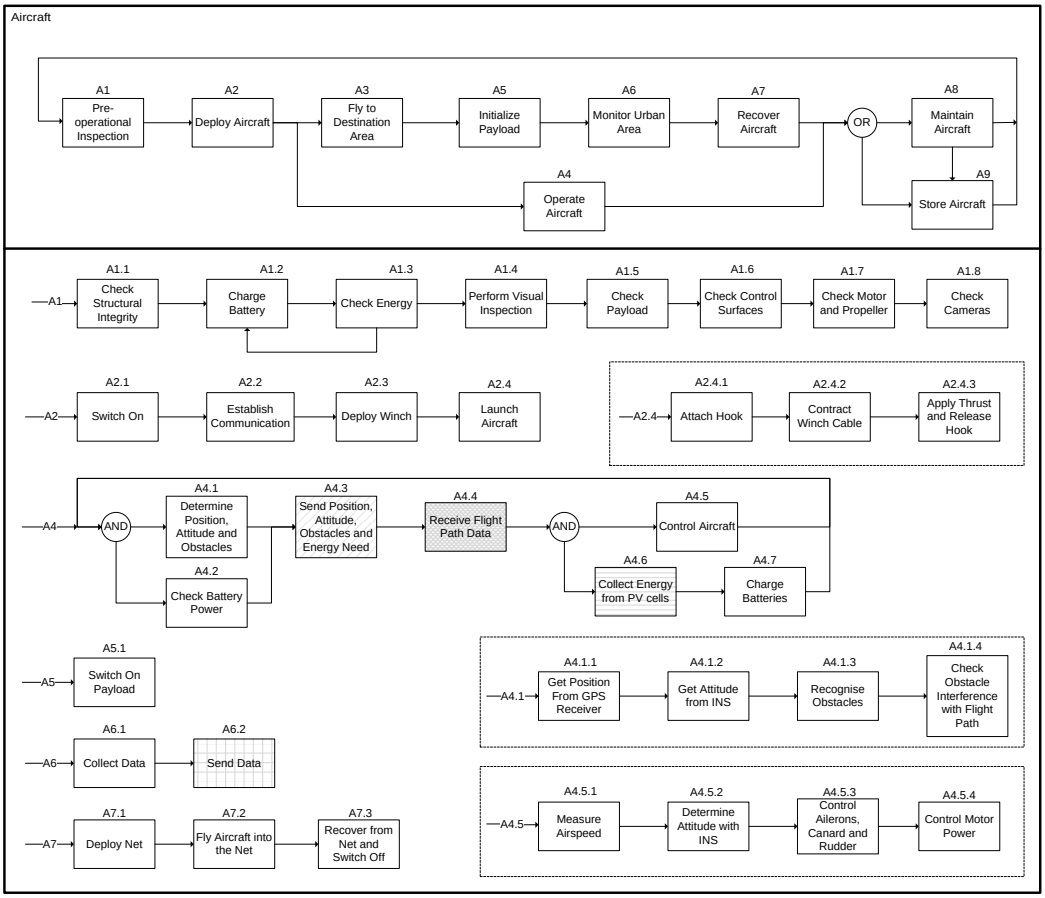

Figure B.1: Functional Flow diagram of the aircraft.

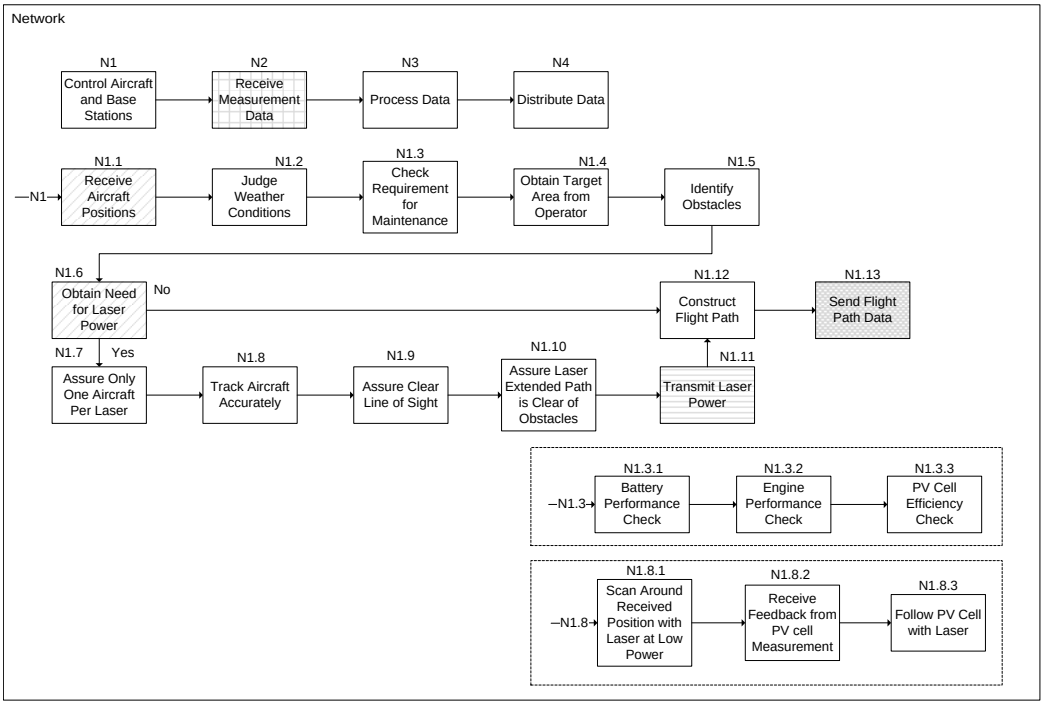

Figure B.2: Functional Flow diagram of the network.

B.2 Functional Breakdown Structure

The Functional Breakdown Structure is a tool used in the functional analysis of the system, and presents an other view of the system than the Functional Flow Diagram. The Functional Breakdown Structure is a hierarchical structure in the form of an and tree. It helps with identifying functions that cannot be placed in a flow form, e.g. 'provide lift'.

The Functional Breakdown Structure for the system is shown in figure B.3. It consists of the top level functions Maintain Network, Perform Flight, Provide Power, Monitor and Launch and Recover. These top level functions are then further broken down into lower level functions. Maintain Network comprises of maintaining the aircraft and maintaining the base stations. The aircraft are assigned a flight path and must avoid collisions while the base stations track the aircraft in order to fire the laser beam accurately and are synchronised with the other base stations. Perform Flight is an essential function of the mission and is the combination of lift, propulsion, stability and control, and communications. Determining position and attitude, and transmitting commands is put under the function establish communications. Provide Power is divided into providing power to the base stations and providing power to the aircraft. Storing power is a function of the aircraft, whereas distributing the power over (sub)systems is for both the aircraft and base stations. The top level function Monitor contains the lower level functions obtain measurement data, process data, transmit data and receive data. The last two also have the functions of providing uplink and downlink respectively. The last function contains the launch and recovery under normal as well as abnormal conditions, where the latter contains performing emergency procedures.

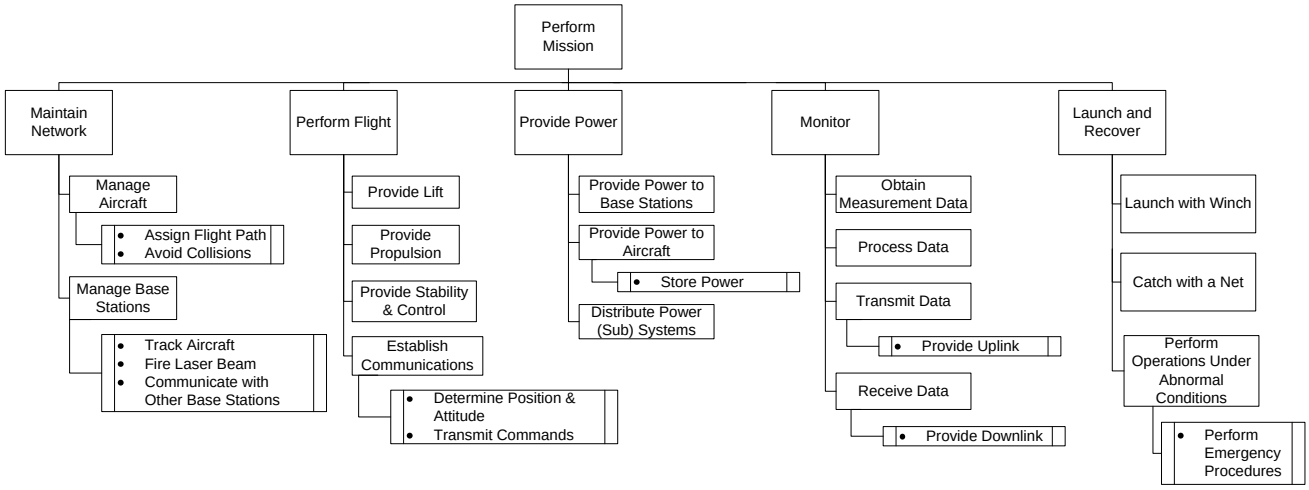

Figure B.3: Functional Breakdown Structure.

APPENDIX C

RESULTS

In this appendix the final values of the conceptual design are presented.

C.1 List of Symbols

Table C.1: Dimension parameters of the conceptual design.

Parameters	Unit	Value
Λ_{LEc}	[°]	0.0
Λ_{LEv}	[°]	31.8
Λ_{LEw}	[°]	13.8
Λ_{TEw}	[°]	0.0
λ_c	[-]	1
λ_v	[-]	0.3
λ_w	[-]	0.4
AR_c	[-]	10
AR_v	[-]	5.0
AR_w	[-]	7.0
$b_c/2$	[m]	0.77
$b_v/2$	[m]	0.41
b_w	[m]	3.10
c_{r_c}	[m]	0.15
c_{t_c}	[m]	0.15
c_{r_v}	[m]	0.26
c_{t_v}	[m]	0.08
c_{r_w}	[m]	0.64
c_{t_w}	[m]	0.25
l_f	[m]	2.5
MAC	[m]	0.47
r_f	[m]	0.25
S_c	[m^2]	0.24
S_v	[m^2]	0.14
S_w	[m^2]	1.40

Table C.2: Performance parameters of the conceptual design.

Parameters	Unit	Value
α_{stall}	[°]	13.3
μ	[°]	45
C_{D_0}	[-]	0.038
$C_{L_{des}}$	[-]	0.50
$C_{L_{max}}$	[-]	1.30
G	[%]	10.5
h	[m]	230
L/D	[-]	10.2
P_{req}	[kW]	1.2
V_c	[$m \cdot s^{-1}$]	27.8
V_s	[$m \cdot s^{-1}$]	16.7

Table C.3: Mass of the systems and the location of the c.g.

Group	**Component**	**Mass [kg]**	**Location c.g in % of l_f [-]**	**Location c.g in [m] from the nose**
Fuselage	Electric System	4.5	85	2.1
	Propulsion system	0.5	100	2.6
	Pv cell	1.3	50	1.3
	Structure	6.4	58	1.5
	Communications	0.6	30	0.8
	Obstical detection	0.7	10	0.3
	Cannard	1.1	10	0.3
	Flight control	0.5	83	2.1
	Total fuselage	15.8	61	1.5
Wing	Structure	4.5	91	2.3
	Control Surfaces	0.1	98	2.5
	Vertical Stabilizer	0.8	95	2.4
	Total wing	5.4	92	2.3
Payload		10.3	60	1.5
MTOW		31.5	66	1.6